AD

USAAMRDL TECHNICAL REPORT 72-14

DERIVATION OF A FATIGUE LIFE MODEL FOR GEARS

By

J. H. Rumbarger
L. Leonard

May 1972

EUSTIS DIRECTORATE
U. S. ARMY AIR MOBILITY RESEARCH AND DEVELOPMENT LABORATORY
FORT EUSTIS, VIRGINIA

130

CONTRACT DAAJ02-70-C-0068
FRANKLIN INSTITUTE RESEARCH LABORATORIES
PHILADELPHIA, PENNSYLVANIA

D D C
RECEIVED
JUN 29 1972
B

DISCLAIMERS

The findings in this report are not to be construed as an official Department of the Army position unless so designated by other authorized documents.

When Government drawings, specifications, or other data are used for any purpose other than in connection with a definitely related Government procurement operation, the U. S. Government thereby incurs no responsibility nor any obligation whatsoever; and the fact that the Government may have formulated, furnished, or in any way supplied the said drawings, specifications, or other data is not to be regarded by implication or otherwise as in any manner licensing the holder or any other person or corporation, or conveying any rights or permission, to manufacture, use, or sell any patented invention that may in any way be related thereto.

Trade names cited in this report do not constitute an official endorsement or approval of the use of such commercial hardware or software.

DISPOSITION INSTRUCTIONS

Destroy this report when no longer needed. Do not return it to the originator.

14. KEY WORDS	LINK A		LINK B		LINK C	
	ROLE	WT	ROLE	WT	ROLE	WT
Spur Gear Life						
Gear Life						
Gear Reliability						
Fatigue Life						
Calculation Method						

II

DOCUMENT CONTROL DATA - R & D

(Security classification of title, body of abstract and indexing annotation must be entered when the overall report is classified)

1. ORIGINATING ACTIVITY *(Corporate author)*	2a. REPORT SECURITY CLASSIFICATION
Franklin Institute Research Laboratories Philadelphia, Pennsylvania	UNCLASSIFIED
	2b. GROUP

3. REPORT TITLE

DERIVATION OF A FATIGUE LIFE MODEL FOR GEARS

4. DESCRIPTIVE NOTES *(Type of report and inclusive dates)*

Final Report (25 June 1970 through 25 November 1971)

5. AUTHOR(S) *(First name, middle initial, last name)*

John H. Rumbarger   and Larry Leonard

6. REPORT DATE	7a. TOTAL NO. OF PAGES	7b. NO. OF REFS
May 1972	138	16
8a. CONTRACT OR GRANT NO DAAJ02-70-C-0068 b. PROJECT NO	9a. ORIGINATOR'S REPORT NUMBER(S) USAAMRDL Technical Report 72-14	
c. Task 1G162203D14414	9b. OTHER REPORT NO(S) *(Any other numbers that may be assigned this report)*	
d.	FIRL F-C2864	

10. DISTRIBUTION STATEMENT

Approved for public release; distribution unlimited.

11. SUPPLEMENTARY NOTES	12. SPONSORING MILITARY ACTIVITY
	Eustis Directorate, U.S. Army Air Mobility Research and Development Laboratory, Fort Eustis, Virginia

13. ABSTRACT

A load-life model is developed for calculating the fatigue life and reliability of a spur gear mesh. The dynamic capacity of a gear mesh is defined as the tangential load which can be transmitted for one million pinion revolutions with a 90% probability of survival. The model is an extension of the currently accepted Lundberg-Palmgren Rolling Element Bearing Life Model. Limited rolling contact testing of cylindrical samples with and without traction in the contact was accomplished. At a low coefficient of traction (below 0.1), no statistically significant effect on fatigue life was noted. Scanning electron microscopy studies were performed of all test samples. One rolling test sample was SEM examined periodically during testing to observe initiation and progression of failure. Numerical examples are presented for the calculation of the dynamic capacity of a standard contact ratio and a high contact ratio spur gear mesh.

I

DD FORM NOV 65 **1473**

The research described herein was conducted by the Franklin Institute Research Laboratories under the terms of Contract DAAJ02-70-C-0068. The work was performed under the technical management of Mr. L. Bartone and Mr. E. R. Givens, Propulsion Division, Eustis Directorate, U. S. Army Air Mobility Research and Development Laboratory.

The objective of this research effort was to develop a load-life model for calculating the fatigue life and reliability of a spur gear mesh. The model derived pertains only to the surface pitting mode of gear failure and is an extension of the currently accepted Lundberg-Palmgren Rolling Element Bearing Life Model.

Appropriate technical personnel of this Directorate have reviewed this report and concur with the conclusions contained herein.

III

DERIVATION OF A FATIGUE
LIFE MODEL FOR GEARS

Final Report

by

J. H. Rumbarger
L. Leonard

IV

SUMMARY

A load-life model is developed for calculating the fatigue life and
reliability of a spur gear mesh. The dynamic capacity of a gear mesh
is defined as the tangential load which can be transmitted for one
million pinion revolutions with a 90% probability of survival. The
model is an extension of the currently accepted Lundberg-Palmgren Rolling
Element Bearing Life Model. Limited rolling contact testing of cylindri-
cal samples with and without traction in the contact was accomplished.
At a low coefficient of traction (below 0.1) no statistically significant
effect on fatigue life was noted. Scanning electron microscopy studies
were performed of all test samples. One rolling test sample was SEM
examined periodically during testing to observe initiation and progression
of failure. Numerical examples are presented for the calculation of the
dynamic capacity of a standard contact ratio and a high contact ratio
spur gear mesh.

$\overline{V}$

FOREWORD

This is the final report of the Franklin Institute Research Laboratories' project entitled "Derivation of a Fatigue Life Model for Gears." This project was conducted during the 18-month period from 25 June 1970 through 25 November 1971 for the Eustis Directorate, U. S. Army Air Mobility Research and Development Laboratory under Contract DAAJ02-70-C-0068, DA Task 1G162203D14414.

U. S. Army Air Mobility Research and Development Laboratory technical direction was provided by Mr. L. Bartone and Mr. R. Givens.

The principal investigators at FIRL were Mr. J. H. Rumbarger (Project Engineer) for the stress analysis and derivation of the life model, and Dr. J. Meakin and Dr. L. Leonard of the Materials Science Department of FIRL for the metallurgical examination and classification. Other investigators who contributed to the success of the project at FIRL were Mr. E. G. Filetti, Mr. J. Dunfee, Mr. J. Zudans, and Mr. M. L. Adams.

FIRL would also like to acknowledge assistance of Mr. R. Valori of the Naval Air Propulsuion Test Center, Philadelphia Naval Base, for supplying qualified MIL-L-7808 oil for the tests and helpful suggestions throughout. Also, Mr. A. J. Lemanski, Vertol Boeing Company, provided tne sample problem material for the standard and high contact ratio gear sets. His encouragement and suggestions were also appreciated.

TABLE OF CONTENTS

TABLE OF CONTENTS (Cont.)

LIST OF ILLUSTRATIONS

LIST OF ILLUSTRATIONS (Cont.)

LIST OF ILLUSTRATIONS (Cont.)

LIST OF TABLES

INTRODUCTION

A need exists for improved life and reliability estimating methods for critical mechanical components. Helicopter transmissions are a complex system of rolling element bearings and gears. The current emphasis upon increased reliability and decreased maintenance requires methods to evaluate the relative risk or reliability of each individual component. Thus, high-risk or low-reliability components can be identified and the proper design effort expended to improve their performance. Present gearing technology and AGMA Standards[1] enable a designer to design a safe gear with a long anticipated life. Gear technology does presently enable the designer to calculate the anticipated hours of life of a gear mesh at specified loads, speeds, and duty cycles for a given probability of survival. The ability to estimate gear operating life would enable a designer to consider reliability and would be an important step toward increasing the maintanability of U. S. Army aviation mechanical transmission equipment.

Current rolling element bearing technology[2,3] provides the design engineer with the ability to calculate the anticipated hours of life of rolling element bearings under specified loads, speeds and duty cycles for a given probability of survival. The overall reliability of the system of bearings in a transmission can also be expressed for a given probability of survival.

Rolling element bearings and gears have much in common, and technological advances in one field should logically be applied to the other. In 1947, the first significant step toward a solution of the problem for life rating rolling element bearings was accomplished with the publication of a new comprehensive mathematical treatment, "Dynamic Capacity of Rolling Bearings," by Lundberg and Palmgren. A supplement to the original paper, "Dynamic Capacity of Rolling Bearings," was published in 1952.[3] The Anti-Friction Bearing Manufacturer's Association (AFBMA) adopted this mathematical life model and incorporated it into an American industry standard in 1949.[4] The United States of America Standards Institute also adopted the theory and issued Standard B3.11-1959, entitled "American Standard Method of Evaluating Load Ratings for Ball and Roller Bearings."[5] Adoption of these standards has resulted in a more uniform method of load rating the bearings and has reduced the amount of conflicting claims made by different manufacturers for essentially the same configuration of bearings. The present program is an attempt to apply the same Lundberg-Palmgren load-life model to a spur gear mesh.

There are four common modes of gear failure: tooth breakage, surface pitting, scoring, and wear. The fatigue life model derived in this report pertains only to the surface pitting mode of gear failure. Thus, it must be assumed that a gear mesh is properly designed to avoid tooth

breakage and scoring and to have an acceptable wear life before one can realistically talk in terms of a load-life computation involving a specified probability of survival. This is also the case with rolling element bearings where failure modes such as fracture of races or rolling elements and sliding or skidding of the elements with respect to the races as well as serious wear problems h. /e been properly designed out of the system prior to evaluation of lit. estimates and reliability numbers.

The resulting fatigue life model for a spur gear mesh is intended to be used in a similar manner to, and in conjunction with rolling element bearing fatigue life estimates. In this manner, the reliability estimates for a complete transmission involving bearings and gear meshes can be calculated.

The following analytical and experimental analyses were conducted during this investigation.

STRESS ANALYSIS

The effects of tractions in a rolling contact upon subsurface shear stresses were determined from the current literature. The variation of maximum values of several stresses which are candidates for being considered the decisive stress amplitude were investigated. The magnitude and depth below the operating surface of the maximum value of each candidate decisive stress amplitude were determined in terms of the applied coefficient of traction (ratio of traction to applied normal load).

FORMULATION OF LIFE MODEL

The currently accepted rolling element bearing load-life model was then used as a starting point for the derivation of a fatigue life model for a spur gear mesh. The dynamic capacity (tangential load that a spur gear mesh can carry for 1 million stress repetitions or tooth loadings) was then presented in terms of the decisive stress amplitudes which are a function of surface traction.

EXPERIMENTAL EVALUATION OF TRACTION EFFECTS UPON ROLLING FATIGUE LIFE

A rolling fatigue life experimental program both with and without surface traction in the contact was accomplished. This experimental program determined the effect of traction (expressed analytically above) upon rolling fatigue life.

FAILURE INVESTIGATION AND CLASSIFICATION

A complete metallurgical examination of all test specimen failures was conducted using the latest available scanning electron microscope techniques.

DYNAMIC CAPACITY OF A SPUR GEAR MESH

The results of the experimental and analytical studies were then combined to express a dynamic capacity of a spur gear mesh complete with suggested material constants. The dynamic capacity number in this form can be used directly with the transmitted tangential gear load and the revolutions per minute of the pinion to calculate pitting fatigue life of the mesh for 90% (B-10) probability of survival.

NUMERICAL EXAMPLE

The derived dynamic capacity equation for a spur gear mesh was then used to numerically calculate the relative fatigue life of a standard contact ratio gear mesh and a comparable high contact ratio spur gear mesh.

STRESS ANALYSIS

LUNDBERG-PALMGREN LIFE MODEL

The Lundberg-Palmgren theory introduces the material shear stress at a critical depth below the contact surface and the volume of material subjected to stress. Correlation between theory and test results was obtained by using a statistical method. The life formula for rolling bearings may be expressed as:

$$\log \frac{1}{S} \sim \frac{\tau_o^c \, N^e \, V}{z_o^h} \tag{1}$$

where
- S = probability of survival, percent
- τ_o = decisive stress amplitude, psi
- z_o = depth below surface to τ_o, in.
- N = millions of stress repetitions
- V = stressed volume in.^{3}
- e = Weibull exponent
- $c \& h$ = material constants to be determined

Appropriate expressions for the decisive stress amplitude (τ_o), its depth below the surface (z_o), stress repetitions (N), and the stress volume (V) must be substituted into Eq. 1 and the unknown exponents (c, e, h) correlated with test data in order to obtain a load-life relationship.

Two subsurface shear stresses have been identified and calculated for the case of a contact of elastic bodies. The unidirectional maximum subsurface shear stress occurs directly beneath the point of rolling and is proportional to the applied load. This shear stress varies in magnitude but does not reverse in orientation. This shear stress is expressed as one-half the difference of the maximum and minimum principal stresses at the point. The reversing orthogonal subsurface shear stress occurs below the surface, but it is zero under the line of load application. The single amplitude magnitude of this stress is less than that of the unidirectional shear stress. However, its total amplitude in reversal is greater than that of the unidirectional shear stress. These two subsurface shear stresses will be defined in detail and presented as a function of surface traction in the following portions of the stress analysis. The octahedral shear stress is also used on occasion for stress computation and will be considered below.

STRESSES IN LINE CONTACT

Figure 1 shows two solid elastic bodies in line contact. It also shows the coordinates of an element of volume in the subsurface. This contact

of a cylinder with another cylinder or a flat surface is described as "line contact" because the initial contact under no load is along a mathematical line. Application of load (P) results in an elastic compression or flattening of the bodies in contact and the formation of measurable width. The contact area shown in Figure 2 is 2b wide by ℓ_{eff} in length.

$$\sigma_{zx} = \frac{2P}{\pi \ell_{eff} b} \sqrt{1 - \frac{x^2}{b^2}}$$
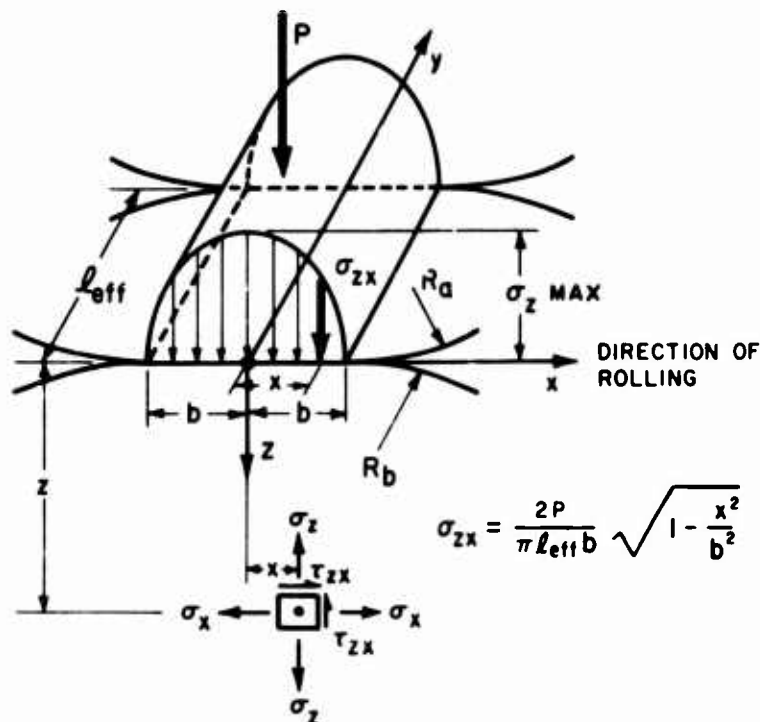
Figure 1. Solid Elastic Bodies in Contact (Line Contact)
With Surface and Subsurface Field.

Figure 2, taken from Reference 6, shows the subsurface stress field along the line of symmetry (Y=0) and directly under the applied load. The subsurface shear stress (τ_{23}) is the unidirectional subsurface shear stress. The magnitude and depth for the maximum values of this stress are given by Eqs. 2 and 3 for the classical case of line contact with no traction.

$$\tau_{23} = 0.304 \, \sigma_{z_{max}} = 0.304 \, \frac{2P}{\ell_{eff} \, \pi b} \tag{2}$$

$$z_o = 0.78 \, b \tag{3}$$

5

VALUES OF STRESS COMPONENTS (σ_z MAX)

$$\tau_{23} = \left|\frac{\sigma_2 - \sigma_3}{2}\right|$$
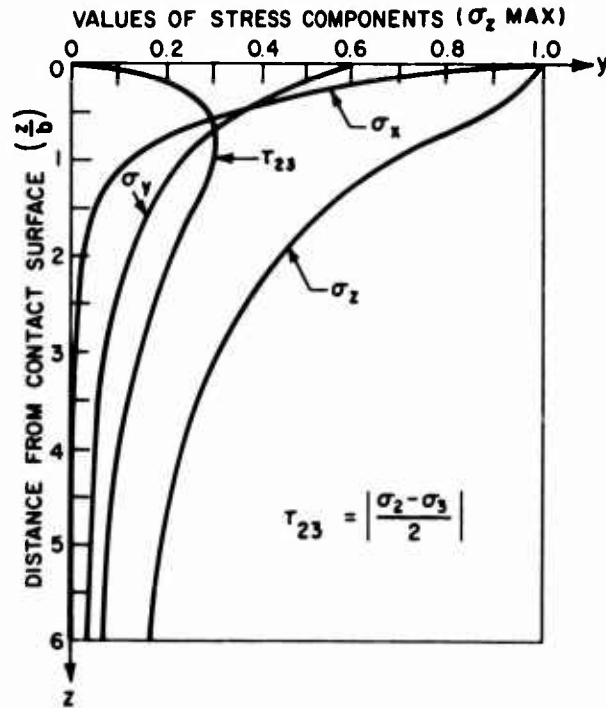
Figure 2.   Subsurface Stress Field Along Line of Symmetry (y=o)
(Line Contact).

Figure 3 shows the subsurface stress field at a depth of 78% of the
contact semiwidth below the contact surface. This is in the X-Z plane
of Figure 1, and the subsurface shear stress of interest is the "orthogo-
nal reversing subsurface shear stress", τ_{zx}. The magnitude of the
maximum single amplitude value of τ_{zx} and depth below the surface are
given in Eqs. 4 and 5.

$$\tau_{zx_{max}} = 0.256 \, \sigma_{z_{max}} = 0.256 \cdot \frac{2P}{\ell_{eff}} \frac{}{\pi b} \tag{4}$$

$$z_o = 0.5 \, b \tag{5}$$

The maximum value of τ_{zx} occurs at y = $\pm$ 0.85b from the line of symmetry
as shown in Figure 3.

6
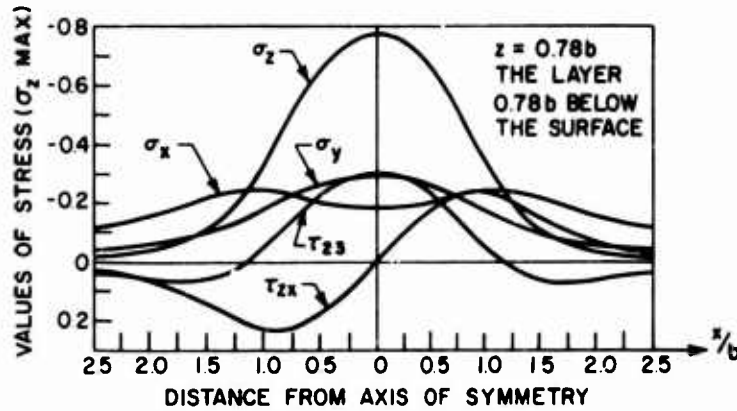
Figure 3.   Subsurface Stress Field Showing Maximum Value of Orthogonal
(τ_{zx}) Shear Stress (Line Contact).

The single amplitude of τ_{zx} (Eq. 4) is less than the amplitude of the
unidirectional subsurface shear stress, τ_{23} of Eq. 2, However, the
double amplitude for total range of the orthogonal reversing subsurface
shear stress τ_{zx} (Eq. 4) is greater than the total amplitude of the uni-
directional subsurface shear stress, τ_{23} of Eq. 2.   The orthogonal
reversing subsurface shear stress is usually considered to be the stress
which is decisive for fatigue calcul tions and should be used in Eq. 1.
The unidirectional subsurface shear stress, τ_{23}, is usually considered to
be representative of the static load capability of the material.   Since
both subsurface shear stresses are expressed as a proportional constant
times the maximum surface compressive stress (Hertz stress), it is not
possible to determine from the currently accepted Lundberg-Palmgren work
of References 2 and 3 which is the decisive stress amplitude.   Therefore,
both stresses will be considered as they are affected by surface tractions.
A third stress sometimes used for failure analysis is the octahedral
shear stress.   This is a resolution of a system of three-dimensional
stresses into two systems acting on the eight octahedral planes.   One
system consists of octahedral shearing stresses and the other system is
equal octahedral normal stresses.[7] Octahedral shearing stresses
on the eight octahedral planes are usually associated with yielding or
inelastic action and are used in connection with the energy of distortion
theory of failure. The octahedral shear stress is not usually considered
in determination of fatigue life as expressed by Eq. 1.

STRESSES IN LINE CONTACT WITH TRACTION

An extension of the fatigue life model of Eq. 1 for the case of a spur
gear requires the determination of the decisive stress amplitude and its
depth below the surface.   The case of stresses and deformations due to
tangential and normal loads on an elastic solid with applications to
contact stresses was the subject of the doctoral thesis by C. K. Liu.[8]
This work was subsequently published in the ASME Transactions[9]

7

and summarized in textbook form in Reference 7. Figure 4 represents normal and tangential loads for two rollers in contact according to the Liu analysis.

The Liu analysis considered both normal and tangential loads to be distributed in Hertzian fashion over the area of contact. The magnitude of the intensity of the tangential load is assumed to be linearly proportional to that of the normal load when sliding motion of the body is impending. The stresses in the elastic body due to the application of these loads on its boundary were presented in closed form[8,9] for both plane-stress and plane-strain cases. A numerical value of $\mu = 1/3$ was assumed for the linear proportionality (coefficient of traction) between the tangential and normal loads in order that the distribution of stresses could be illustrated. The significance of the stress distribution across the contact area and in the body was also discussed. It was shown that when the combination of loads considered in Reference 9 was applied at the contact area of the bodies, the maximum shearing stress τ_{12} would be at the surface instead of beneath the surface. For example, for plane strain, with a coefficient of traction of $\mu = 1/3$, the maximum shearing stress occurred at the surface and was 43% larger than the maximum shearing stress which would act below the surface when normal force acts alone. The effects of range of normal stress and of shearing stress on the plane of maximum shear and on the plane of maximum octahedral shear on failure by progressive fracture (fatigue) were discussed. Liu did not consider the variation of the orthogonal reversing subsurface shear stress τ_{zx}. Liu's investigation further showed that when the coefficient of traction became greater than $\mu = 1/9$, the maximum shearing stress, τ_{12}, occurred at a point in the surface. But when μ was less than 1/9, the stress was underneath the surface. The present study uses the formulation and results of the Liu study and considers the variations and location of maximum values of the orthogonal reversing subsurface shear stress, τ_{xz}, as well as the effects of traction on the unidirectional maximum subsurface shear stresses.

The equations for the subsurface stresses due to combined application of distributed normal and tangential loads are given in Eqs. 6 through 14 of Table I. These equations are taken directly from Reference 8. Combination of the state of stress at a point in the subsurface into principal stresses, maximum shear stresses, and octahedral shear stresses is given in Eqs. 15 through 22 of Table II, again based on standard elasticity[7] and presented in Reference 8 in detail.

The work by Liu[8] was carried out in detail in his thesis with a coefficient of traction of 1/3. The stress equations (Eqs. 6 through 9) have been generalized in the traction coefficient, μ. These equations and the corresponding principal stress and maximum shear equations (Eqs. 15 through 22) were programmed for rapid solution by digital computer. The range of investigation of the variables of interest are shown in Table III. Essentially, four coefficients of traction were used with the exception that a finer grid was used in the case of the

8
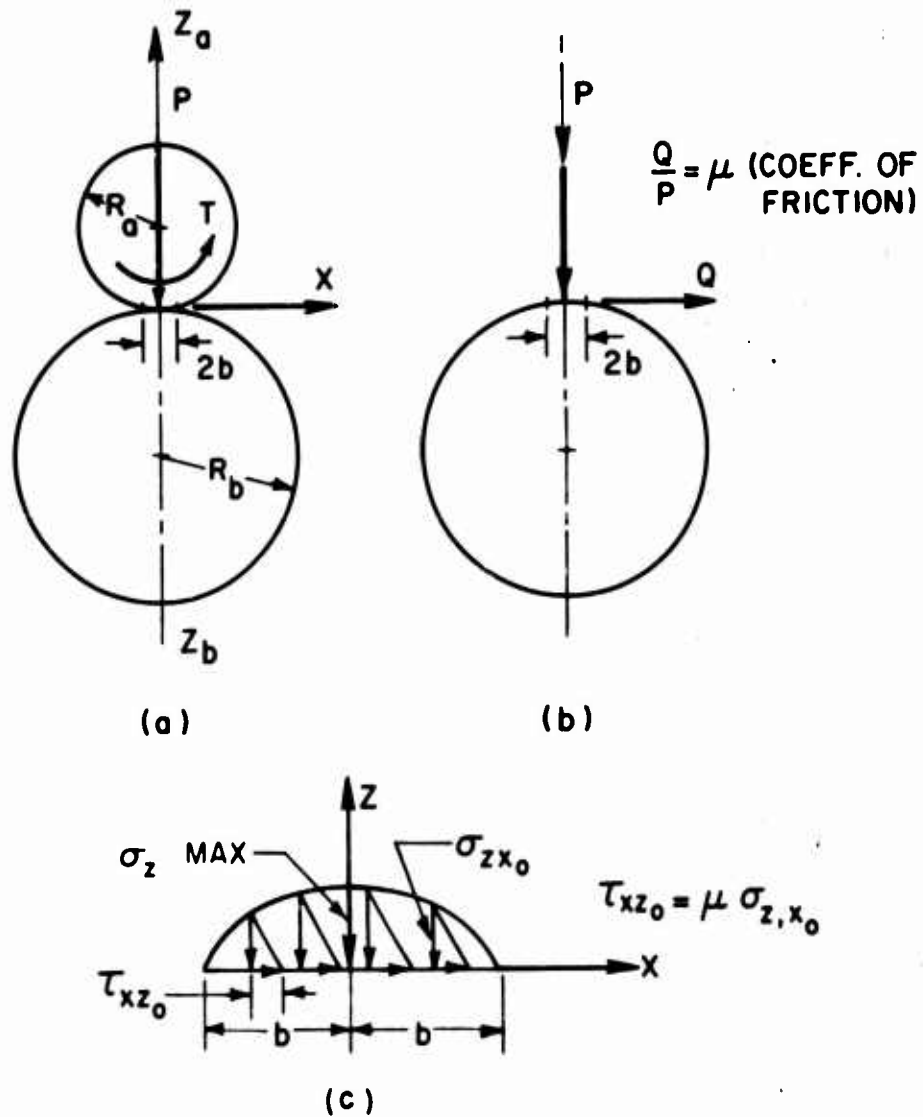
Figure 4.   Normal and Tangential Loads for Two Rollers in Contact.

TABLE I. SUBSURFACE STRESSES DUE TO COMBINED APPLICATION OF DISTRIBUTED NORMAL AND TANGENTIAL LOADS

$$\sigma_x = -\frac{2P}{\pi^2 b}\left\{(b^2 + 2x^2 + 2z^2)\frac{z}{b}\bar{\psi} - \frac{2\pi z}{b} - 3xz\phi + \mu\left[(2x^2 - 2b^2 - 3z^2)\phi + \frac{2\pi x}{b} + 2(b^2-x^2-z^2)\frac{x}{b}\bar{\psi}\right]\right\} \tag{6}$$

$$\sigma_y = -\frac{4P\nu}{\pi^2 b}\left\{[(b^2 + x^2 + z^2)\frac{z}{b}\bar{\psi} - \frac{\pi z}{b} - 2xz\phi] + \mu\left[(x^2 - b^2 - z^2)\phi + \frac{\pi x}{b}(b^2-x^2-z^2)\frac{x}{b}\bar{\psi}\right]\right\} \tag{7}$$

$$\sigma_z = -\frac{2P}{\pi^2 b}z[b\bar{\psi} - x\phi + \mu z\phi] \tag{8}$$

$$\tau_{xz} = -\frac{2P}{\pi^2 b}\left\{z^2\phi + \mu[(b^2 + 2x^2 + 2z^2)\frac{z}{b}\bar{\psi} - \frac{2\pi z}{b} - 3xz\phi]\right\} \tag{9}$$

$$\phi = \frac{\pi}{K_1} \cdot \frac{1 - \sqrt{\frac{K_2}{K_1}}}{\sqrt{\frac{K_2}{K_1}}\sqrt{2\sqrt{\frac{K_2}{K_1}} + \left[\frac{K_1 + K_2 - 4b^2}{K_1}\right]}}$$

$$\bar{\psi} = \frac{\pi}{K_1} \cdot \frac{1 + \sqrt{\frac{K_2}{K_1}}}{\sqrt{\frac{K_2}{K_1}}\sqrt{2\sqrt{\frac{K_2}{K_1}} + \left[\frac{K_1 + K_2 - 4b^2}{K_1}\right]}} \tag{10}$$

where $b = \sqrt{\frac{2P\Delta}{\pi}}$

$$\Delta = \frac{2}{\left(\frac{1}{R_a} + \frac{1}{R_b}\right)}\left[\frac{1 - \nu_1^2}{E_1} + \frac{1 - \nu_2^2}{E_2}\right] \tag{11}$$

$$\left.\begin{array}{l} K_1 = (b + x)^2 + z^2 \\[2mm] K_2 = (b - x)^2 + z^2 \end{array}\right\} \tag{12}$$

10

TABLE II.	PRINCIPAL, MAXIMUM SHEAR, AND MAXIMUM OCTAHEDRAL SHEAR STRESSES

$$\sigma_1 = \sigma_y \tag{13}$$

$$\sigma_2 = \frac{\sigma_x + \sigma_z}{2} + \sqrt{\frac{(\sigma_x - \sigma_z)^2}{4} + (\tau_{xz})^2} \tag{14}$$

$$\sigma_3 = \frac{\sigma_x + \sigma_z}{2} - \sqrt{\frac{(\sigma_x - \sigma_z)^2}{4} + (\tau_{xz})^2} \tag{15}$$

$$\theta = \tan^{-1}\left[\frac{2\tau_{xz}}{\sigma_x - \sigma_z}\right]$$

$$\tau_{12_{max}} = \left|\frac{\sigma_1 - \sigma_2}{2}\right|$$

$$\tau_{13_{max}} = \left|\frac{\sigma_1 - \sigma_3}{2}\right| \tag{16}$$

$$\tau_{23_{max}} = \left|\frac{\sigma_2 - \sigma_3}{2}\right|$$

$$\tau_{OCT_{max}} = \frac{1}{3}\sqrt{(\sigma_1 - \sigma_2)^2 + (\sigma_2 - \sigma_3)^2 + (\sigma_3 - \sigma_1)^2} \tag{17}$$

TABLE III.	RANGE OF INVESTIGATION OF EFFECT OF TRACTION UPON STRESSES	
Description	Symbol	Values Investigated
Coeff. Of Traction	μ	0, 0.075, 0.15, 0.333
Depth	z/b	0 to 1.2 in 0.1 Steps 0.02 Steps in range of interest
Distance	x/b	0 to ± 1.0

octahedral shear stress. The results of the computer compilation of stress fields at the various points in the subsurface were computer-plotted in order to rapidly and visually determine the variation of the candidate decisive stress amplitudes. These plots were helpful in locating the areas of maximum and minimum. Then the detailed computer sheets were used to obtain accurate readout. A summary of the effects ot surface traction on subsurface shear stresses is given in Table IV. In this table, it should be noted that the double amplitude of the orthogonal reversing subsurface shear stress τ_{zx} is given.

VARIATION OF ORTHOGONAL REVERSING SUBSURFACE SHEAR STRESS

A plot of the orthogonal reversing subsurface shear stress, τ_{xy}, as a function of the coefficient of traction is given in Figure 5. Table V gives the single amplitude and sum or range of τ_{xz} as a function of surface traction. It is apparent from the figure and the table that the total range remains constant. The depth at which the maximum amplitude or range is encountered remains constant at 0.5 b. With a zero coefficient of traction, the plus and minus amplitudes are equal. As the coefficient of traction increases, the plus amplitude decreases, but it is compensated for by an increase in the negative amplitude.

The use of the orthogonal reversing subsurface shear stress, τ_{xz}, in a life model would result in no life changes as a function of changes in surface traction across the gear tooth. The decisive stress amplitude in this case does not change in magnitude or depth with changes in surface traction.

VARIATION OF UNIDIRECTIONAL SUBSURFACE SHEAR STRESS

Table IV indicates that in the plane of rolling (xz plane), the τ_{23} unidirectional subsurface shear stress increases in magnitude and decreases in its depth from the surface of contact with an increase in the coefficient of traction.

TABLE IV. SUMMARY OF EFFECTS OF SURFACE TRACTION ON SUBSURFACE SHEAR STRESSES

Stress Ratio	Coeff. of Traction	Stress Magnitude	Location of Max Value	
			z/b	x/b
$\tau_{12}/\sigma_{z\ max}$	0.0	0.2589	0.60	0.0
	0.075	0.2635	0.50	0.1
	0.150	0.2770	0.0	0.1
	0.333	0.3775	0.0	0.3
$\tau_{13}/\sigma_{z\ max}$	0.0	0.0666	1.2	0.0
	0.075	0.0677	1.2	0.4
	0.150	0.0706	0.8	0.9
	0.333	0.2332	0.0	1.0
$\tau_{23}/\sigma_{z\ max}$	0.0	0.3002	0.8	0.0
	0.075	0.3025	0.8	0.2
	0.150	0.3096	0.6	0.6
	0.333	0.3549	0.4	0.9
$2\tau_{zx}/\sigma_{z\ max}$	0.0	0.4983	0.5	0.9
	0.075	0.4983	0.5	0.9
	0.150	0.4983	0.5	0.9
	0.333	0.4983	0.5	0.9
$\tau_{OCT}/\sigma_{z\ max}$	0.0	0.2614	0.8	0.0
	0.075	0.2636	0.6	0.3
	0.150	0.2711	0.6	0.4
	0.200	0.2779	0.6	0.5
	0.250	0.2871	0.5	0.7
	0.300	0.3142	0.0	0.3
	0.333	0.337	0.0	0.3
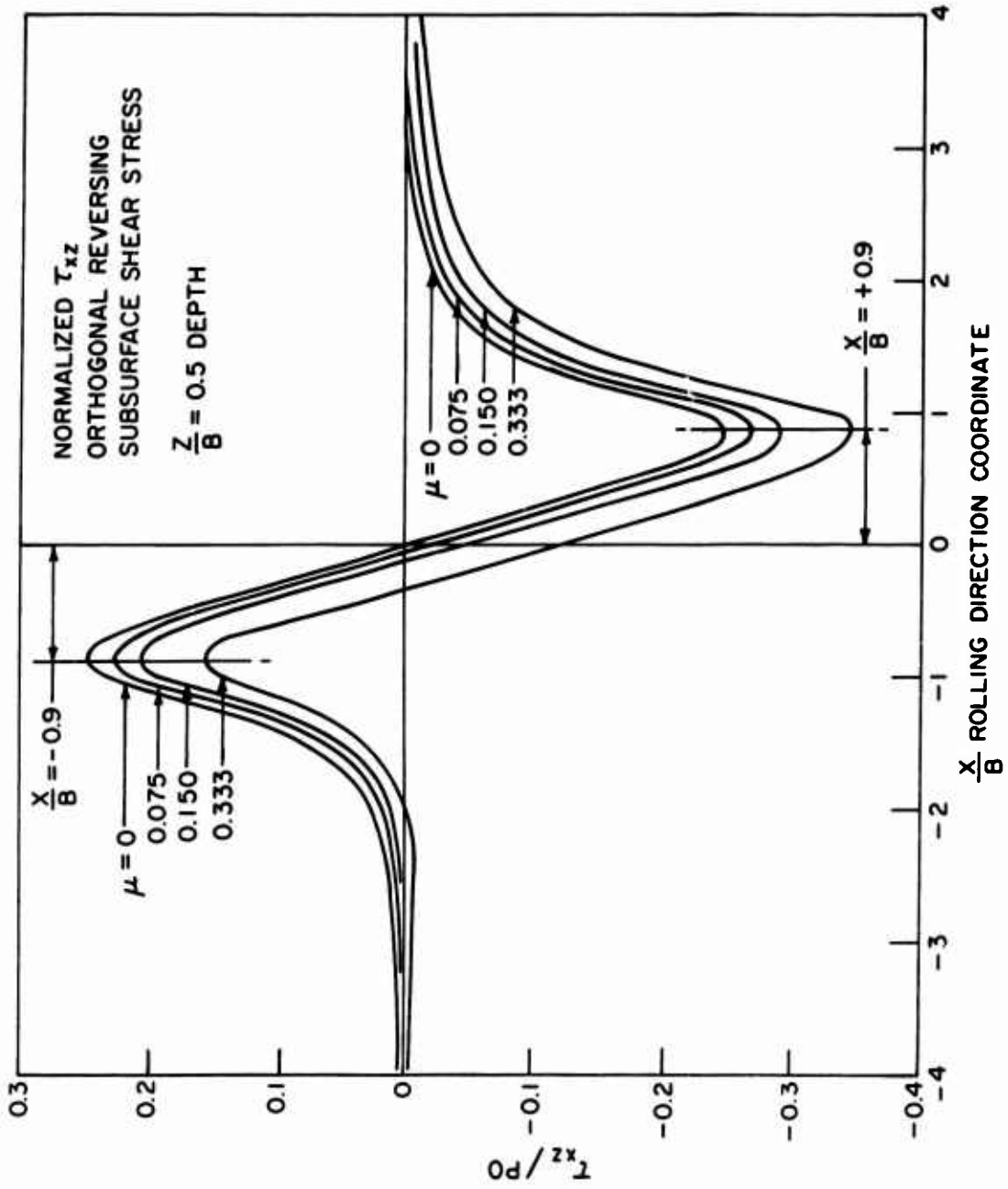
Figure 5. τ_{xz} Range as a Function of Coefficient of Traction.

14

	τ_{xz}	τ_{xz}	Sum or	Depth
μ	$\frac{x}{b} = -0.9$	$\frac{x}{b} = +0.9$	τ_{xz} Range	z/b
0	+ 0.24913	- 0.24913	0.49826	0.5
0.075	+ 0.22670	- 0.27155	0.49825	0.5
0.150	+ 0.20428	- 0.29398	0.49826	0.5
0.333	+ 0.14946	- 0.34880	0.49826	0.5

TABLE V. EFFECT OF TRACTION ON ORTHOGONAL REVERSING SUBSURFACE SHEAR STRESS, τ_{xz}

It should also be noted from Table IV that the subsurface shear stress, τ_{12}, does indeed reach a maximum in the surface of the contact with a coefficient of traction of approximately 1/9, as indicated by Liu.[8,9] The remaining subsurface shear stress, τ_{13}, reaches a maximum in the surface with a coefficient of traction between 0.15 and 0.33. However, magnitude of the stresses in the subsurface of both τ_{12} and τ_{13} is considerably less than the magnitude of the τ_{23} maximum shear stress. The magnitude of τ_{12} in the surface with a coefficient of traction of 0.333 exceeds the magnitude of τ_{23} in the subsurface at a similar coefficient of traction. The formulation of a fatigue life model based on the Lundberg-Palmgren formulation of Eq. 1 assumes variation of a decisive stress amplitude at a depth below the surface. Shear stresses in the contact surface will undoubtedly have an effect on surface metallurgy and surface life. However, for the purposes of the present subsurface oriented fatigue life model, the variation in the maximum unidirectional shear stress in the plane of rolling, τ_{23}, is of interest.

The effect of the coefficient of traction upon the decisive stress amplitude and its depth is given in Table VI for the maximum unidirectional subsurface shear stress, τ_{23}. The expressions in Table VI are a non-dimensional ratio of the maximum magnitude of τ_{23} with traction to the maximum value without traction. Also, a similar ratio of the depth below the surface is given. Both the magnitude and depth are expressed as second order polynomials in the coefficient of traction, μ. Figure 6 gives the curve showing the variation of the shear stress magnitude with the coefficient of traction. Figure 7 shows the relationship between the depth below the surface of the shear stress as a function of the coefficient of traction.

TABLE VI. EFFECT OF COEFF. OF TRACTION UPON DECISIVE STRESS AMPLITUDE AND ITS DEPTH

$$\frac{\tau_{23\ Max}}{\sigma_z\ Max} = \frac{\tau o}{\sigma_z\ Max} = 0.30036 - 0.01205\ \mu + 0.5421\ \mu^2 \quad (18)$$

$$\frac{Zo}{b} = 0.7819 - 0.05822\ \mu - 3.9873\ \mu^2 \quad (19)$$

VARIATION OF THE OCTAHEDRAL SHEAR STRESS

The variation of the octahedral shear stress, τ_{oct}, shown on Table IV, is represented in Figure 8. The variation of depth below the surface of the octahedral shear stress, as a function of coefficient of traction, is shown on Figure 9. It is seen here that a smooth curve fit is not possible with a second-order polynomial in terms of the coefficient of traction because of the rapid rise to the surface with the coefficient of traction above 0.25. The octahedral shear stress (Eq. 17 of Table II) is essentially a root-mean-square average of the three sub-surface uni-directional shear stresses. Therefore, the variation of the octahedral stress, both in magnitude and depth within the range of interest, is not significantly different from that of the maximum unidirectional sub-surface shear stress, τ_{23}.

SPUR GEAR FRICTION

The coefficient of friction or traction in a spur gear mesh varies with the pitch line velocity, tooth contact load, and lubricant. A ceiling value of $\mu \leq 0.06$ is reported by Dudley[17] for 20° and 25° pressure angle standard spur gears with lightweight and medium weight petroleum oils at 120°F oil inlet temperature.
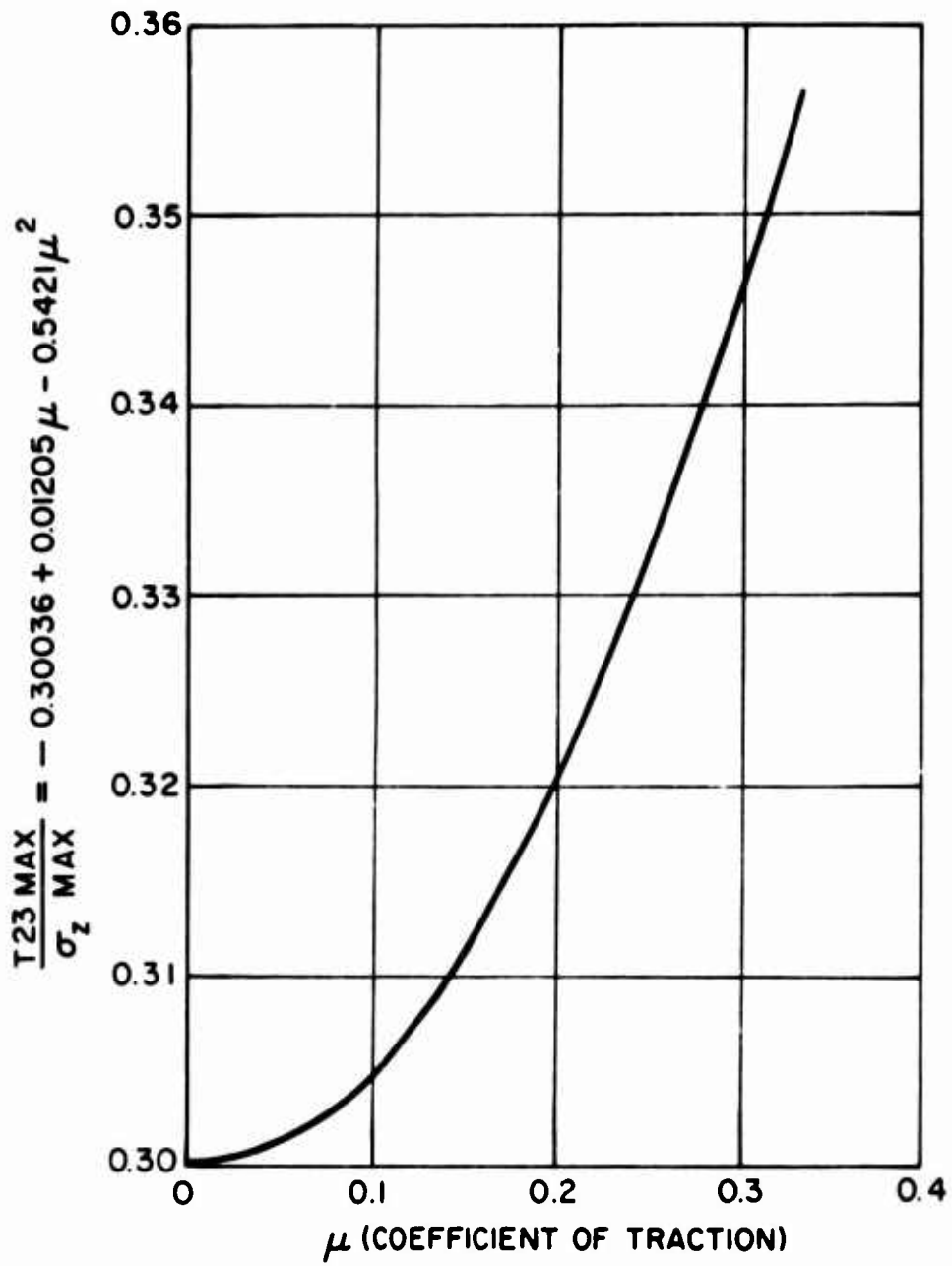
Figure 6. Variation of Maximum Shear Stress, τ_{23}, With Surface Traction.

17
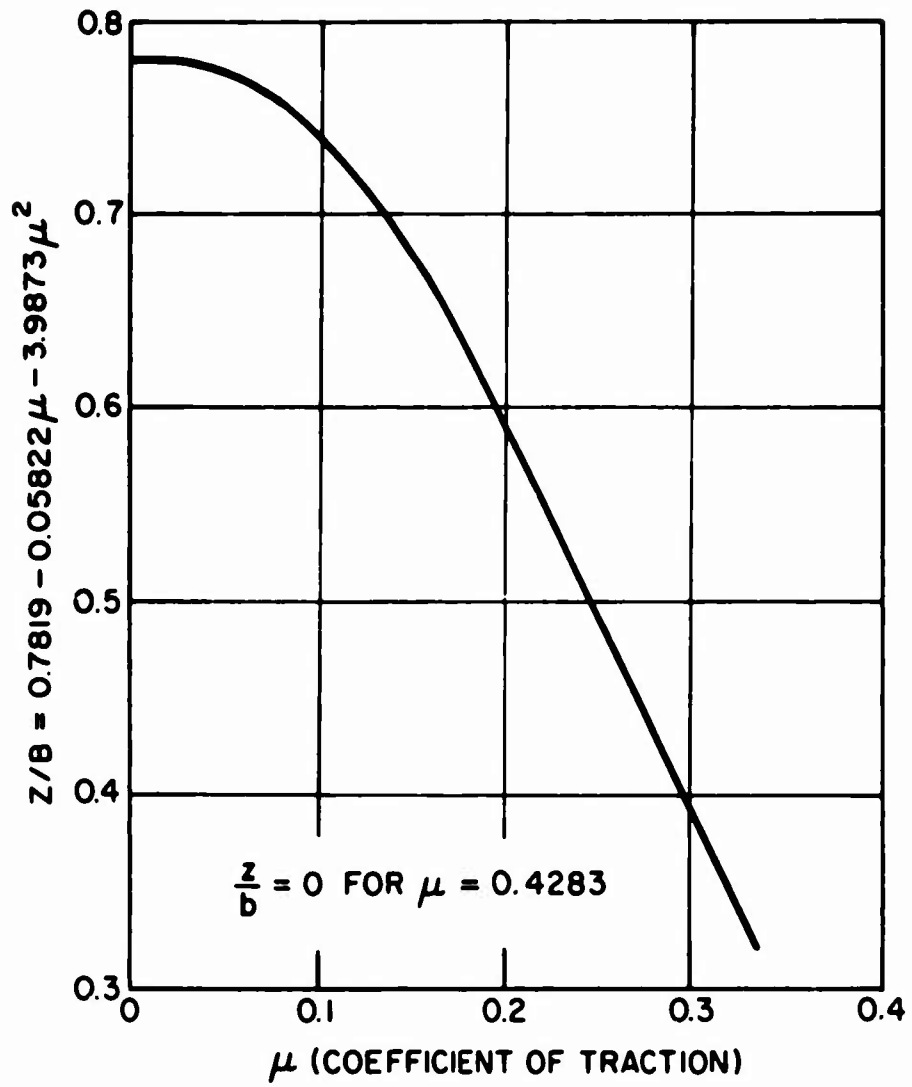
Figure 7. Variation of Depth to Maximum Shear Stress With Surface Traction.
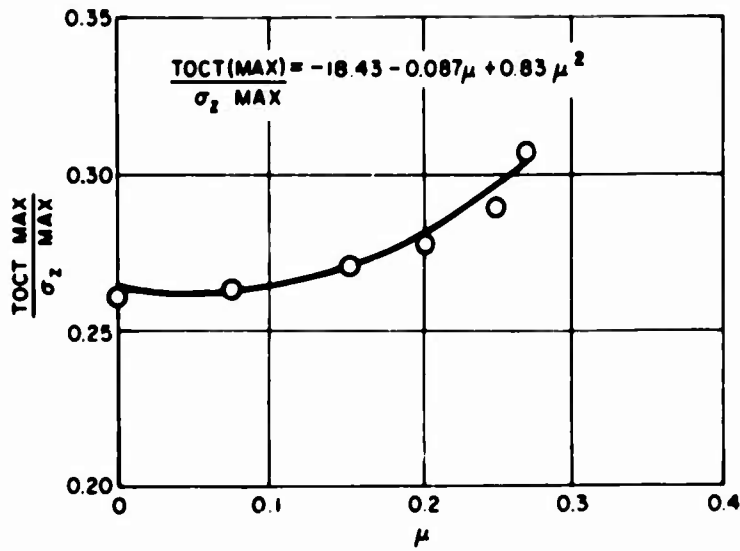
Figure 8. Variation of Octahedral Shear Stress With Surface
Traction.
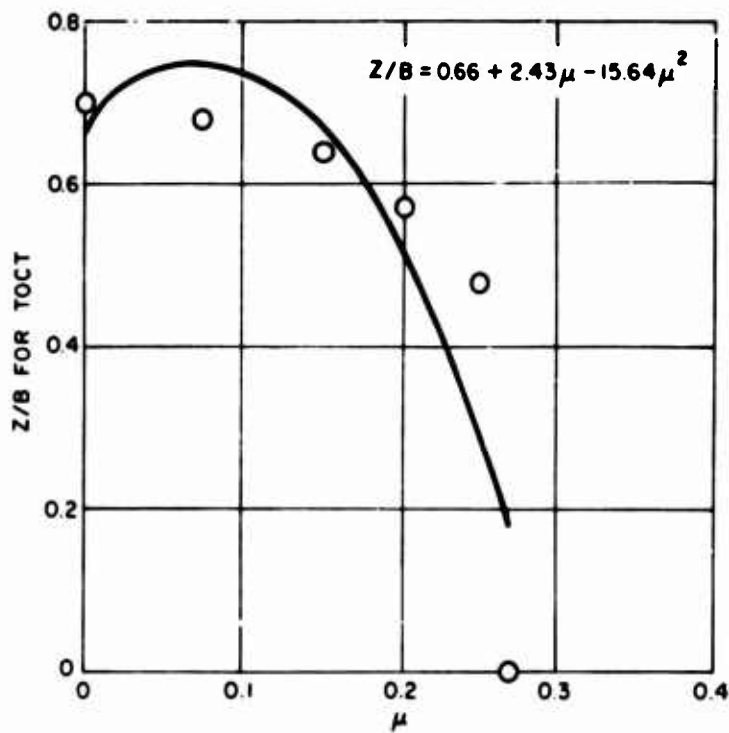
Figure 9. Variation of Depth to Octahedral Shear Stress
With Surface Traction.

19

FORMULATION OF A FATIGUE LIFE MODEL FOR INVOLUTE SPUR GEARS

LOAD ZONES IN GEAR MESH

Over the complete arc of contact, a gear tooth goes through a number of "load zones" where the load varies because of the number of teeth in contact. The "contact ratio" of a given mesh is a direct indication of the number of teeth in contact. For example, if a mesh has a contact ratio of 1.6, then 60% of the time two teeth in the mesh share the load and 40% of the time a single tooth carries the transmitted load. Each time the number of teeth in contact changes, another "load zone" is entered.

$$\text{Mp} = \text{Contact Ratio} = n + x$$
$$\text{where } n = \text{integer value} \qquad [20]$$
$$o < x < 1$$

$$\text{then the number of load zones} = 2n + 1 \qquad [21]$$

Define β_L as the angle of travel for each low-load zone (i.e., with larger number of teeth in contact) and β_H as the angle of travel for each high-load zone (i.e., with smaller number of teeth in contact). Then β_L and β_H are expressed as

$$\left. \begin{aligned} \beta_L &= x \, \gamma / \text{Mp} \\[2ex] \beta_H &= (1-x) \, \gamma / \text{Mp} \end{aligned} \right\} \qquad [22]$$

where Mp is the profile contact ratio or the average number of teeth that are in contact and γ is the total angle of tooth contact. Z is the length of the line of action. N_1 is the number of pinion teeth.

$$\left. \begin{aligned} \text{Mp} &= \frac{Z \, N_1}{2\pi r_1 \cos\phi} \\[3ex] Z &= \rho_P + \rho_G - C \sin\phi \end{aligned} \right\} \qquad [23]$$

$$\left. \begin{aligned} \rho_P &= \sqrt{r_{o1}^2 - (r_1\cos\phi)^2} \quad \text{(At Pinion Tip)} \\[3ex] \rho_G &= \sqrt{r_{o2}^2 - (r_2\cos\phi)^2} \quad \text{(At Gear Tip)} \end{aligned} \right\} \qquad [24]$$

20

The total angle of contact, γ, can then be expressed as

$$\gamma = (n+1)\ \beta_L + (n)\ \beta_H \qquad [25]$$

Load zones for standard and high contact ratio spur gear meshes are illustrated in Figures 10 and 11.

The total angle of the arc contact on the tooth can also be expressed as the sum of the angle of approach and the angle of recess.

$$\gamma = \phi_1 + \phi_1' \qquad [26]$$

where

ϕ_1 = Angle of approach

ϕ_1' = Angle of recess

The extent of the load zones as functions of the contact ratio and the angle of contact are tabulated in Table VII and illustrated in Figures 10 and 11 for several ranges of contact ratio. From Reference 10, these angles are

$$\phi_1 = [(r_2 + a_2)\ \sin \phi_2 - r_2 \sin \phi]/r_{b1} \qquad [27]$$

$$\phi_1' = [(r_1 + a_2)\ \sin \phi_1 - r_1 \sin \phi]/r_{b1} \qquad [28]$$

1 refers to pinion
2 refers to gear

where   a = addendum

r = pitch radius

r_b = base circle radius

and the auxiliary angles are:

$$\left.\begin{array}{l} \phi_1 = \cos^{-1}\ \dfrac{r_{b1}}{r_1 + a_1} < \pi/2 \\[2em] \phi_2 = \cos^{-1}\ \dfrac{r_{b2}}{r_2 + a_2} < \pi/2 \end{array}\right\} \qquad [29]$$

21
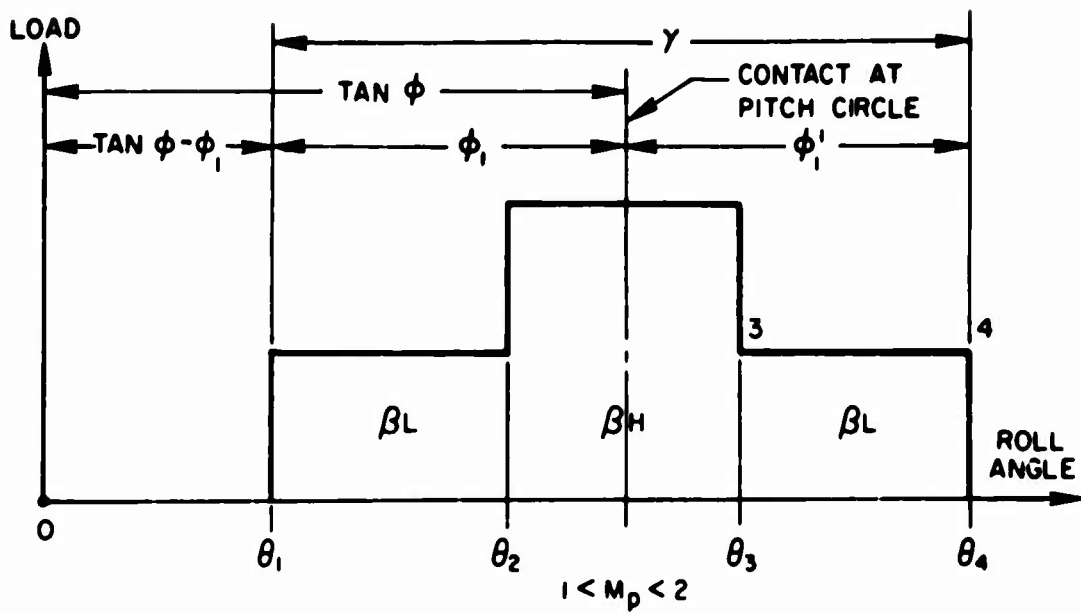
Figure 10. Gear Tooth Load Distribution, Normal Contact Ratio.
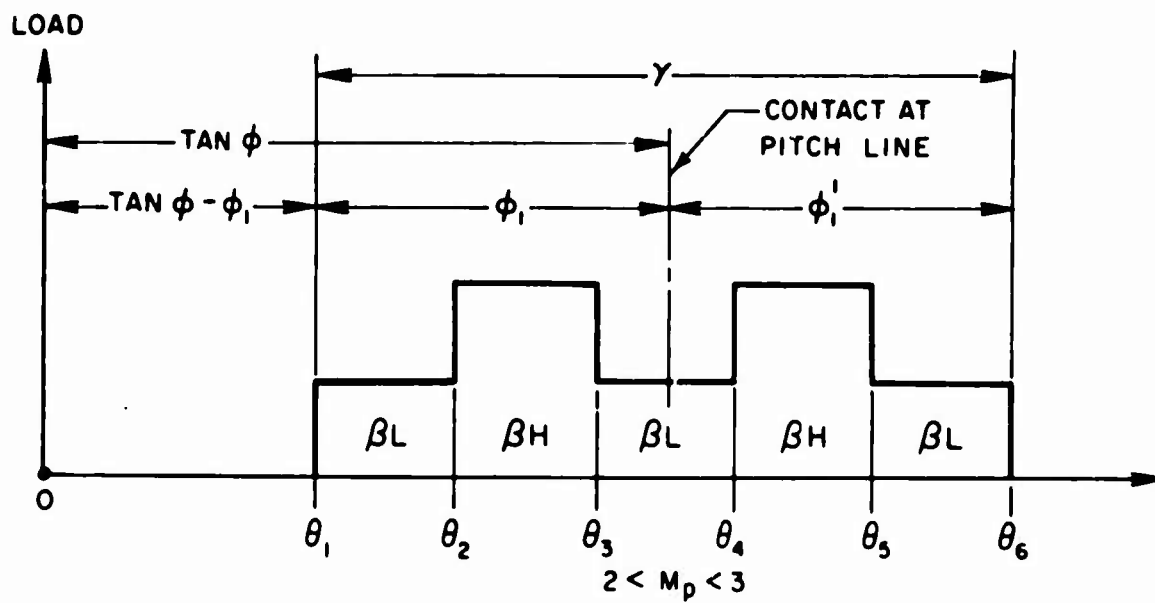
Figure 11. Gear Tooth Load Distribution, High Contact Ratio.

TABLE VII. EXTENT OF GEAR TOOTH LOAD ZONES

Point	Roll Angle	$1 < m_P < 2$	i^*	$2 < m_P < 3$	i^*
1	$\theta_1 = \tan\phi - \phi_1$	$\theta_1 = \tan\phi - \phi_1$	2	$\theta_1 = \tan\phi - \phi_1$	3
2	$\theta_2 = \theta_1 + \beta_L$	$\theta_2 = \tan\phi - \phi_1 + \dfrac{x\gamma}{m_P}$	1	$\theta_2 = \tan\phi - \phi_1 + \dfrac{x\gamma}{m_P}$	2
3	$\theta_3 = \theta_1 + 3\beta_L + \beta_H$	$\theta_3 = \tan\phi - \phi_1 + \dfrac{\gamma}{m_P}$	2	$\theta_3 = \tan\phi - \phi_1 + \dfrac{\gamma}{m_P}$	3
4	$\theta_4 = \theta_1 + 2\beta_L + \beta_H$	$\theta_3 = \tan\phi - \phi_1 + \dfrac{(1+x)\gamma}{m_P}$		$\theta_3 = \tan\phi - \phi_1 + \dfrac{(1+x)\gamma}{m_P}$	
		$(1+x) = m_P$			
		$\gamma = \phi_1 + \phi_i$			
		$\theta_3 = \tan\phi + \phi_i$			
5	$\theta_5 = \theta_1 + 2\beta_L + 2\beta_H$			$\theta_5 = \tan\phi - \phi_1 + \dfrac{2\gamma}{m_P}$	2
6	$\theta_6 = \theta_1 + 3\beta_L + 2\beta_H$			$\theta_6 = \tan\phi - \phi_1 + \dfrac{(2+x)\gamma}{m_P}$	3
				$(2+x) = m_P$	
				$\gamma = \phi_1 + \phi_i$	
				$\theta_6 = \tan\phi + \phi_i$	

$*i$ = number of teeth in contact.

23

ARC CONTACT IN GEAR MESH

The equation of the pinion base circle (Figure 12) is

$$x^2 + y^2 + 2\, r_{b1}\, y = 0 \qquad\qquad [30]$$

and

$$\frac{d_y}{d_x} = \frac{-x}{r_{b1}+y} \qquad\qquad [31]$$
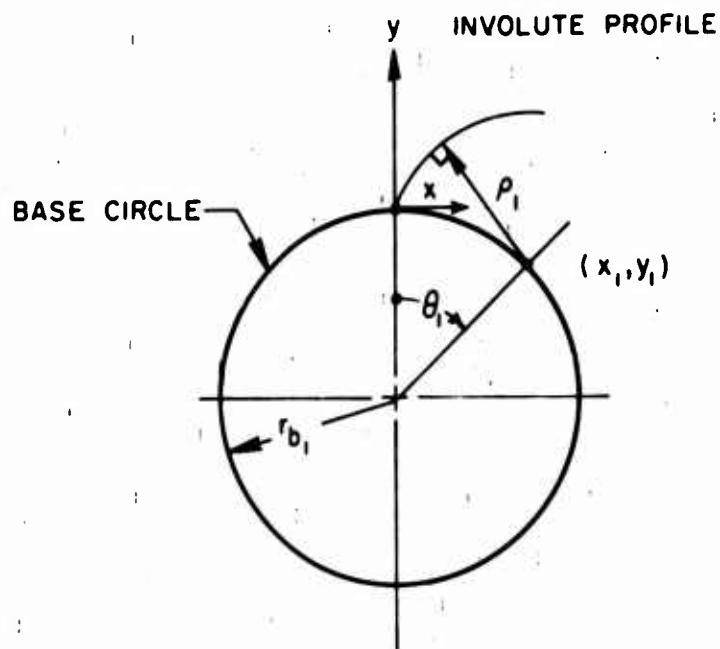
Figure 12. Involute Geometry.

By definition, the radius of curvature to the point of contact on the involute profile is the product of the base circle radius and the angle of roll.

$$\rho_1 = r_{b1}\, \theta_1 \qquad\qquad [32]$$

and

$$\left. \begin{array}{l} x_1 = r_{b1}\, \sin\, \theta_1 \\[2mm] y_1 = r_{b1}\, (\cos\, \theta_1 - 1) \end{array} \right\} \qquad\qquad [33]$$

24

The coordinates of the involute are then

$$
\left.
\begin{aligned}
x &= x_1 - \rho_1 \cos \theta_1 = r_{b1} (\sin \theta_1 - \theta_1 \cos \theta_1) \\
y &= y_1 + \rho_1 \cos \theta_1 = r_{b1} (\cos \theta_1 - 1 + \theta_1 \sin \theta_1)
\end{aligned}
\right\}
\qquad [34]
$$

The tooth "Contour Differential" or arc of contact differential is defined as

$$
ds = \sqrt{d_x^2 + d_y^2} = \sqrt{1 + \left(\frac{d_y}{d_x}\right)^2}\ d_x
\qquad [35]
$$

where $\quad \dfrac{d_y}{d_x} = \tan \theta_1$

Differentiation of Equation 34 and substitution into Equation 35 gives

$$
d_s = r_{b1}\ \theta_1 \tan \theta_1\ d\theta_1
\qquad [36]
$$

INTEGRAL FORMULATION OF LIFE MODEL

The basic form of the Lundberg-Palmgren load-life model was given in Equation 1 as

$$
\log \frac{1}{S} \sim \frac{\tau_o^{\,c}\ N^e\ V}{z_o^{\,h}}
\qquad [1]
$$

The stressed volume, V, can be expressed for the involute spur gear tooth in terms of the differential arc of contact as

$$
V = \int_S F\ z_o\ d_s
\qquad [37]
$$

The decisive stress amplitude, τ_o, is given by Equation 18 as:

$$
\tau_o = T\ \sigma_z \text{max} = \frac{2\ T\ P_N}{\pi\ F\ b}
\qquad [38]
$$

where

$$
T = \frac{T_{23\ \text{max}}}{\sigma_z\ \text{max}} = 0.30036 - 0.01205_\mu + 0.5421_\mu 2
\qquad [18]
$$

25

The depth, z_0, to maximum value of the decisive stress amplitude is

$$z_0 = \xi b \qquad [39]$$

$$\xi = \frac{z_0}{b} = 0.7819 - 0.05822\mu - 3.9873\mu^2 \qquad [19]$$

The millions of stress repetitions, N, can be expressed in terms of the stress repetition per revolution of the pinion, u, and the millions of pinion revolutions, L, as

$$N = uL \qquad [40]$$

For a single tooth, a given point on the surface is stressed once per revolution of the pinion.

$$\left.\begin{array}{l} u = 1 \\ N = L \end{array}\right\} \qquad [41]$$

Substituting Equations 37 through 41 into Equation 1 results in

$$\log \frac{1}{S} \sim \left(\frac{2}{\pi}\right)^c F^{1-c} L e \int_s \frac{(T\ P_N)^c}{\xi^{h-1}\ b^{c+h-1}}\ ds \qquad [42]$$

The contact semiwidth, b, of the line contact between the mating gear teeth can be expressed (Ref. 6) in terms of the normal load, P_N, as

$$\left.\begin{array}{c} b = \left[\dfrac{P_N\ (\frac{1}{E_1'} + \frac{1}{E_2'})}{\pi\ F(\frac{1}{\rho_1} + \frac{1}{\rho_2})}\right]^{1/2} \\ \\ \text{where} \qquad E_i' = \dfrac{E_i}{(1-\nu_i^2)} \end{array}\right\} \qquad [43]$$

26

Substituting into Equation 42 gives

$$\log \frac{1}{S} \sim (\frac{2}{\pi})^c \left[\frac{\pi}{\left[\frac{1}{E_1'}+\frac{1}{E_2'}\right]}\right]^{\frac{c+h-1}{2}} F^{\frac{h-c+1}{2}} L^e \int_s \frac{T^c P_N^{\frac{c-h+1}{2}} \left[\frac{1}{\rho_1}+\frac{1}{\rho_2}\right]^{\frac{c+h-1}{2}}}{(\xi)^{h-1}} ds \quad [44]$$

Expressing the fatigue-life model in terms of the roll angle, θ_1 of Figure 12 and the differential arc length of Equation 36 gives

$$\log \frac{1}{S} \sim (\frac{2}{\pi})^c \left[\frac{\pi}{\frac{1}{E_1'}+\frac{1}{E_2'}}\right]^{\frac{c+h-1}{2}} F^{\frac{h-c+1}{2}} L^e \int_{\theta_1} \frac{T^c P_N^{\frac{c-h+1}{2}}}{\xi^{h-1}} \left(\frac{1}{\rho_1}+\frac{1}{\rho_2}\right)^{\frac{c+h-1}{2}} r_{b_1} \theta_1 \tan\theta_1 d\theta_1$$

$$[45]$$

Expressing the radii of curvature in terms of the gear geometry results in the required integral formulation of the fatigue-life model.

$$\left(\frac{1}{\rho_1}+\frac{1}{\rho_2}\right) = \frac{(r_1+r_2)\sin\phi}{r_{b_1}\theta_1[(r_1+r_2)\sin\phi - r_{b_1}\theta_1]} \quad [46]$$

where

$$\left.\begin{array}{c} \rho_1 + \rho_2 = (r_1+r_2)\sin\phi = \text{Constant} \\ \\ r_{b_1} = r_1\cos\phi \end{array}\right\} \quad [47]$$

27

Substituting into Equation 45

$$
\log \frac{1}{S} \sim \left(\frac{2}{\pi}\right)^c \left[\frac{\pi}{\frac{1}{E_1'}+\frac{1}{E_2'}}\right]^{\frac{c+h-1}{2}} F^{\frac{h-c+1}{2}} L^e \int_{\theta_1} \frac{T^c P_N}{\xi^{h-1}}^{\frac{c-h+1}{2}} \left.\begin{matrix} \\ \\ \cdots \\ \\ \end{matrix}\right.
$$

$$
\left.\left[\frac{(r_1+r_2)\sin\phi}{(r_1+r_2)\sin\phi - r_{b_1}\theta_1}\right]^{\frac{c+h-1}{2}} \left[r_{b_1}\theta_1\right]^{\frac{3-c-h}{2}} \tan\theta_1 \, d\theta_1 \right\} \qquad [48]
$$

The function under the integral sign in Equation 48 is only piecewise continuous by virtue of changes in the number of teeth in contact during a complete arc of contact. Thus, the integral can be formulated separately for each of the distinct loading zones identified in Figures 10 and 11 for various contact ratios.

Let i = the total number of teeth in contact.

Then

$$
P_N = \frac{W_t}{i \, \cos\phi} \qquad [49]
$$

$$
\log \frac{1}{S} \sim A_1 F^{\frac{h-c+1}{2}} L^e \left[(r_1+r_2)\sin\phi\right]^{\frac{c+h-1}{2}} W_t^{\frac{c-h+1}{2}} r_1^{\frac{3-c-h}{2}} \cos\phi^{1-c} \, \Psi \qquad [50]
$$

where

$$
A_1 = \left(\frac{2}{\pi}\right)^c \left[\frac{\pi}{\frac{1}{E_1'}+\frac{1}{E_2'}}\right]^{\frac{c+h-1}{2}} = \left(\frac{2}{\pi}\right)^c (C_p)^{c+h-1} \qquad [51]
$$

$$
\Psi = \sum_{1}^{2N+1} I(\theta)_{k1} \qquad [52]
$$

28

where 2n+1 is the total number of load zones (Figures 10 and 11), k is the roll angle at the beginning, and l is the roll angle at the end of the contact zone.

Where

$$I(\theta)_{kl} \equiv \int_{\theta_k}^{\theta_l} \frac{T^c \, [(r_1+r_2) \sin\phi - r_{b_1} \theta]^{\frac{1-c-h}{2}}}{\xi^{h-1} \, {}_1^{\frac{c-h+1}{2}}} \, [\theta]^{\frac{3-c-h}{2}} \tan\theta \, d\theta \qquad [53]$$

Evaluation of the Ψ function will be discussed in a subsequent section.

DYNAMIC CAPACITY AND LIFE

The dynamic capacity (C_m) of a gear mesh will be defined as the transmitted tangential load, W_t, which can be carried for one million pinion revolutions with a 90% probability of survival; this definition is similar to the definition of the dynamic capacity of ball and roller bearings (References 2 through 5).

The life expressed in millions of pinion revolutions is then expressed as

$$L_{10} = \left(\frac{C_M}{W_t}\right)^P \quad \text{millions of pinion rev.} \qquad [52]$$

The life of the gear mesh can also be expressed in terms of hours by

$$H_{10} = \frac{\left(\frac{C_M}{W_t}\right)^P \times 10^6}{60 \times n_\rho} \quad \text{hours} \qquad [54]$$

The subscript 10 refers to 10% probability of failure (90% probability of survival).

For simplification it will be assumed that the transmitted tangential load, W_t, is divided evenly between the total number of teeth in contact. This omits consideration of unequal load sharing because of tooth bending. The assumption is reasonable for standard contact ratios between 1.0 and 2.0 but is more questionable for higher contact ratios. Let i = the number of teeth in contact. Then from Reference 1,

$$W_t = \frac{HP \times 33,000}{V_t} = \frac{HP \times 126,000}{N_p \, d} \qquad [55]$$

29

where HP = Transmitted horsepower

V_t = Pitch line velocity, fpm

N_p = pinion rpm

d = pinion pitch diameter, in.

The gear mesh, M_G, is defined by

$$M_G = \frac{N_2}{N_1} = \frac{r_2}{r_1} \geq 1 \qquad [56]$$

and

$$r_1 + r_2 = r_1(1 + M_G) \qquad [57]$$

Equation 50 is the probability formulation for a single tooth and may be expressed with Equations 56 and 57 as

$$\log \frac{1}{S} \sim A_1 F^{\frac{h-c+1}{2}} L^e (1+M_G)^{\frac{c+h-1}{2}} (r_1)^{\frac{c-h+1}{2}} W_t^{\frac{c+h-1}{2}} \sin\phi \, \cos\phi^{1-c} \, \psi \qquad [58]$$

Introducing a material constant, B*, and equating and rearranging terms results in

$$W_t L_T^{\frac{2e}{c-h+1}} = B* \left\{ \frac{r_1^{-1} (1+M_G)^{\frac{1-c-h}{2}} (\log \frac{1}{.9}) \sin\phi^{\frac{1-c-h}{2}} \cos\phi^{c-1}}{A_1 F^{\frac{h-c+1}{2}} \psi} \right\}^{\frac{2}{c-h+1}} \qquad [59]$$

Define the dynamic capacity of a single tooth, C_T, as the load that can be sustained for one million pinion revolutions ($L_T = 1.0$ at $S = 0.9$).

Then when $L_T = 1.0$ in Equation 59, W_t is by definition the dynamic capacity of a single tooth.

$$C_T = B* \left\{ \frac{r_1^{-1} (1+M_G)^{\frac{1-c-h}{2}} (\log \frac{1}{.9}) \sin\phi^{\frac{1-c-h}{2}} \cos\phi^{c-1}}{A_1 F^{\frac{h-c+1}{2}} \psi} \right\}^{\frac{2}{c-h+1}} \qquad [60]$$

Also, by forming the ratio of life for the dynamic capacity tooth load, C_T, when $L_T = 1.0$ and the life, L_T, under load W_t results in the load-life law,

$$L_T = \left(\frac{C_T}{W_t}\right)^{\frac{c-h+1}{2e}} = \left(\frac{C_T}{W_t}\right)^P \qquad [61]$$

where

$$p = \frac{c-h+1}{2e} \qquad [62]$$

The life of the pinion is the statistical combination of the individual pinion tooth lives:

$$\frac{1}{L_1^e} = \sum_1^{N_1} \frac{1}{L_T^e} = \frac{N_1}{L_T^e} \qquad [63]$$

In a similar manner, the life of the gear is

$$\frac{1}{L_2^e} = \sum_1^{N_2} \frac{1}{L_T^e} = \frac{N_2}{L_T^e} \qquad [64]$$

The life of the gear mesh is the statistical combination of the life of the pinion and the life of the gear.

$$\frac{1}{L_M^e} = \frac{1}{L_1^e} + \frac{1}{L_2^e} \qquad [65]$$

Then

$$L_M = \left(\frac{N_1}{L_T^e} + \frac{N_1 M_G}{L_T^e}\right)^{-\frac{1}{e}} \qquad [66]$$

From Equation 52, 60 and 61,

$$\left(\frac{C_M}{W_t}\right)^P = \left[\frac{N_1}{\left(\frac{C_T}{W_t}\right)^{pe}} + \frac{N_1 M_G}{\left(\frac{C_T}{W_t}\right)^{pe}}\right]^{-\frac{1}{e}} \qquad [67]$$

31

and

$$C_M = \frac{C_T}{\left[N_1(1+M_G)\right]^{\frac{1}{pe}}} = \frac{C_T}{\left[N_1(1+M_G)\right]^{\frac{2}{c-h+1}}} \tag{68}$$

The dynamic capacity of an involute spur gear mesh, C_M, is

$$C_M = \frac{B^*(\log\frac{1}{.9})^{\frac{2}{c-h+1}} \sin\phi^{\frac{1-c-h}{c-h+1}} \cos\phi^{\frac{c-1}{c-h+1}}}{r_1^{\frac{2}{c-h+1}} (1+M_G)^{\frac{c+h+1}{c-h+1}} A_1^{\frac{2}{c-h+1}} F^{\frac{h-c+1}{c-h+1}} \psi^{\frac{2}{c-h+1}} N_1^{\frac{2}{c-h+1}}} \tag{69}$$

EVALUATION OF ψ FUNCTION

The ψ function was defined by Equations 52 and 53 as

$$\psi = \sum_{1}^{2n+1} I(\theta)_{k\ell} \tag{52}$$

$$I(\theta)_{k\ell} = \int_{\theta_k}^{\theta_\ell} \frac{T^c \left[(r_1+r_2)\sin\phi - r_{b1}\,\theta\right]^{\frac{1-c-h}{2}} \theta^{\frac{3-c-h}{2}} \tan\theta\, d\theta}{\xi_i^{h-1}\,^{\frac{c-h+1}{2}}} \tag{53}$$

Direct integration of $I(\theta)_{k\ell}$ in the form shown has not been accomplished. Simplifications regarding values of the variables usually encountered in an involute spur gear mesh will be made in order to allow a numerical approximation of the integral.

Assume the tooth normal load, P_N, and the coefficient of traction, μ, to be constant over each separate arc of contact as illustrated in Figure 10 for standard contact ratio gears and Figure 11 for high contact ratio gears. The extent of the load zones is expressed in terms of roll angles in Table VII. Assume the arcs of contact to be small enough to allow the value of the angle, θ, within the range to be used without variation throughout the interval. Then the $I(\theta)_{k\ell}$ function of Equation 53 is approximated by

$$I(\theta)_{k\ell} \approx \frac{T^c\left[(r_1+r_2)\sin\phi - r_1\cos\phi\,\theta_k\right]^{\frac{1-c-h}{2}} [\theta_k]^{\frac{3-c-h}{2}} \tan\theta_k[\theta_\ell-\theta_k]}{\xi^{h-1}\,_{(i)}^{\frac{c-h+1}{2}}} \tag{70}$$

32

For arcs of contact in the approach zone, use θ_k or the initial value of the roll angle of the zone of contact. Use the roll angle at the pitch ($\theta = \tan\phi$) for the central load zone. Use the exit roll angle (θ_ℓ) for zones in the arc of recess. Values of 1 for the number of loaded teeth in each zone are given in Table VII for standard and high contact ratio gear meshes.

Define the factor $f_{k\ell}$ as the ratio of the T and ξ functions to the values of T_o and ξ_o with zero traction.

$$ f_{k\ell} = \left(\frac{T}{T_o}\right)_{k\ell}^{c} \cdot \left(\frac{\xi_o}{\xi}\right)^{h-1} \qquad [71] $$

Substituting from Equations 18 and 19 of Table VI.

$$ f_{k\ell} = \frac{\left[\dfrac{0.30036-0.01205_\mu+0.5421_{\mu^2}}{0.30036}\right]^c}{\left[\dfrac{0.7819-0.05822_\mu-3.98/3_{\mu^2}}{0.7819}\right]^{h-1}} \qquad [72] $$

then

$$ f_{k\ell} = \frac{(1.0000-0.0401_\mu+1.8048_{\mu^2})^c}{(1.0000-0.0745_\mu-5.0995_{\mu^2})^{h-1}} \qquad [73] $$

and recognizing that

$$ (r_1+r_2)\sin\phi = C\sin\phi \qquad [74] $$

the Ψ function can then be written as

$$ \Psi = \frac{T_o^{\,c}}{\xi_o^{\,h-1}} \Psi^1 \qquad [75] $$

$$ \Psi^1 = \sum_{1}^{2n+1} 1_{k\ell} \qquad [76] $$

For Standard Contact Ratio Gears $1 < m_p < 2$

33

$$\psi^1 = I_{12} + I_{23} + I_{34} \qquad [77]$$

$$I_{12} = f_{12} \frac{[C\sin\phi - r_1\cos\phi \; \theta_1]^{\frac{1-c-h}{2}} \; \theta_1^{\frac{3-c-h}{2}} \; \tan\theta_1 \; [\theta_2-\theta_1]}{(2)^{\frac{c-h+1}{2}}} \qquad [78]$$

$$I_{23} = f_{23} \frac{[C\sin\phi - r_1\cos\phi\tan\phi]^{\frac{1-c-h}{2}} \; \tan\phi^{\frac{1-c-h}{2}} \; \tan(\tan\phi)[\theta_3-\theta_2]}{(1)^{\frac{c-h+1}{2}}} \qquad [79]$$

$$I_{34} = f_{34} \frac{[C\sin\phi - r_1\cos\phi \; \theta_4]^{\frac{1-c-h}{2}} \; \tan\phi^{\frac{3-c-h}{2}} \; \tan\theta_4[\theta_4-\theta_3]}{(2)^{\frac{c-h+1}{2}}} \qquad [80]$$

For High Contact Ratio Gears $2 < m_p < 3$

$$\psi^1 = I_{12} + I_{23} + I_{34} + I_{45} + I_{56} \qquad [81]$$

$$I_{12} = f_{12} \frac{[C\sin\phi - r_1\cos\phi \; \theta_1]^{\frac{1-c-h}{2}} \; \theta_1^{\frac{3-c-h}{2}} \; \tan\theta_1 \; [\theta_2-\theta_1]}{[3]^{\frac{c-h+1}{2}}} \qquad [82]$$

$$I_{23} = f_{23} \frac{[C\sin\phi - r_1\cos\phi \; \theta_2]^{\frac{1-c-h}{2}} \; \theta_2^{\frac{3-c-h}{2}} \; \tan\theta_2 \; [\theta_3-\theta_2]}{[2]^{\frac{c-h+1}{2}}} \qquad [83]$$

34

$$I_{34} = f_{34} \frac{[C\sin\phi - r_1 \cos\phi\tan\phi]^{\frac{1-c-h}{2}} (\tan\phi)^{\frac{3-c-h}{2}} \tan(\tan\phi)[\theta_4 - \theta_3]}{[3]^{\frac{c-h+1}{2}}} \qquad [84]$$

$$I_{45} = f_{45} \frac{[C\sin\phi - r_1 \cos\phi \; \theta_5]^{\frac{1-c-h}{2}} (\theta_5)^{\frac{3-c-h}{2}} \tan\theta_5 \; [\theta_5 - \theta_4]}{[2]^{\frac{c-h+1}{2}}} \qquad [85]$$

$$I_{56} = f_{56} \frac{[C\sin\phi - r_1 \cos\phi \; \theta_6]^{\frac{1-c-h}{2}} (\theta_6)^{\frac{3-c-h}{2}} \tan\theta_6 \; [\theta_6 - \theta_5]}{[3]^{\frac{c-h+1}{2}}} \qquad [86]$$

EVALUATION OF CONSTANTS

The constants c, h, and e used in Equation 1 and throughout the development of the fatigue life theory need to be correlated with experimental gear test results. In the absence of such massive test data, it is suggested that the values found valid for ball and roller bearing[2,3] fatigue life be used.

$$\left. \begin{array}{l} c = 10 \; 1/3 \\ h = \; 2 \; 1/3 \\ e = \qquad 9/8 \end{array} \right\} \qquad [87]$$

This makes the load-life exponent, p, of Equation 62 the same as that for pure line contact in roller bearings.[3]

$$p = \frac{c-h+1}{2e} = 4 \qquad [62]$$

The material constant, B^* of Equation 69 also needs to be correlated with spur gear test life data. The rolling contact test rig results obtained under the present program can be used to get an estimate for B^*. A full description of the method of correlation is contained in the analysis of the experimental data (Equation 98).

35

Then

$$B * [\log \frac{1}{.9}]^{2/9} \left[\frac{\ell_o^{4/3}}{T_o^{31/3} A_1} \right]^{2/9} = 27,360 \text{ lb \& inch units} \tag{88}$$

EFFECT OF HARDNESS ON LIFE

Hardness is known to have a significant effect upon fatigue life. The AGMA Standard[1] for the durability of spur gears uses a hardness factor. Rolling element bearing life is also reduced when hardness is reduced. A reduction factor based upon pinion hardness should be included in the life formula. It is suggested that the rolling bearing life factor from Reference 11 be used.

$$f_H = \left(\frac{HV}{750} \right)^2 \tag{89}$$

where HV is the Vickers Hardness Ratio.

EFFECTS OF MISALIGNMENT

Roller bearing life rating standards[4,5] use specified columns in a table of rating factors depending upon the amount of roller end or tip modification (crowning) and the degree of guidance of the roller to prevent skewing. These columns are based upon λ reduction factors of Reference 3. In this sense the λ reduction factor is very similar to the C_M load distribution factor of the AGMA Standard[1] For the present time, until fatigue life test data is available for correlation, it is suggested that a conservative value of λ be used. Reference 3 suggests the use of $\lambda = 0.45$ for ordinary unmodified (uncrowned) line contact.

The spur gear dynamic capacity of Equation 69 with the addition of the hardness factor (Equation 89) and the load distribution factor, λ, is summarized in Table VIII.

A later section of this report presents a numerical calculation using the dynamic capacity of Table VIII.

TABLE VIII. SPUR GEAR DYNAMIC CAPACITY

SPUR GEAR DYNAMIC CAPACITY SUMMARY

	Algebraic Form	Numerical Form*
C_M	$B\lambda f_H f_G (1+m_G)^{-\frac{c-h-1}{c-h+1}} F^{\frac{c-h-1}{c-h+1}} (N_1 r_1)^{-\frac{2}{c-h+1}}$	$B\lambda f_H f_G (1+m_G)^{-41/27} F^{7/9} (N_1 r_1)^{-2/9}$
B	$B^* \cdot A_1^{-\frac{2}{c-h+1}} \log\left(\frac{1}{S}\right)^{\frac{2}{c-h+1}} \left\{T_o^{-c} \cdot \zeta_o^{h-1}\right\}^{\frac{2}{c-h+1}}$	$B^* A_1^{-2/9} \log\left(\frac{1}{9}\right)^{2/9} \left\{(0.30036)^{-31/3} \cdot (0.7819)^{4/3}\right\}^{2/9}$
f_H	$\left(\frac{HV}{750}\right)^2$	HV = Vickers Hardness Ratio for R_c 61 or BHN 700, $f_H = 1.0$
f_G	$\left\{\psi \, (\cos\phi)^{1-c} \, (\sin\phi)^{\frac{c+h-1}{2}}\right\}^{\frac{2}{h-c+1}}$	$\left\{\psi \, (\cos\phi)^{-\frac{28}{3}} \, (\sin\phi)^{35/6}\right\}^{-2/9}$

	Standard Contact Ratio $1 < m_p < 2$	High Contact Ratio $2 < m_p < 3$	Standard Contact Ratio $1 < m_p < 2$	High Contact Ratio $2 < m_p < 3$
ψ	$I_{12} + I_{23} + I_{34}$	$I_{12} + I_{23} + I_{34} + I_{45} + I_{56}$	$I_{12} + I_{23} + I_{34}$	$I_{12} + I_{23} + I_{34} + I_{45} + I_{56}$

	Algebraic Form	Numerical Form*
$I_{k\ell}$	$f_{k\ell} \dfrac{[C \sin\phi - r_1 \cos\phi \, \theta_j]^{\frac{1-c-h}{2}} \theta_j^{\frac{3-c-h}{2}} \tan\theta_j [\theta_\ell - \theta_k]}{(i_{k\ell})^{\frac{c-h+1}{2}}}$	$f_{k\ell} \dfrac{[C \sin\phi - r_1 \cos\phi \, \theta_j]^{-35/6} \theta_j^{-29/6} \tan\theta_j [\theta_\ell - \theta_k]}{(i_{k\ell})^{9/2}}$
$f_{k\ell}$	$[1.0000 - 0.0401u_{k\ell} + 1.8048\mu_{k\ell}^2]^C$ $[1.0000 - 0.0745u_{k\ell} - 5.0955\mu_{k\ell}^2]^{\frac{1-h}{2}}$	$[1.0000 - 0.0401u_{k\ell} + 1.8048\mu_{k\ell}^2]^{31/3}$ $[1.0000 - 0.0745u_{k\ell} - 5.0955\mu_{k\ell}^2]^{-4/3}$
$\mu_{k\ell}$	Coefficient of traction in contact k-ℓ.	High Contact Ratio $2 < m_p < 3$

θ_j** $i_{k\ell}$	Standard Contact Ratio $1 < m_p < 2$			Contact kℓ	θ_j	$i_{k\ell}$
	Contact kℓ	θ_j	$i_{k\ell}$	1-2	θ_1	3
	1-2	θ_1	2	2-3	θ_2	2
	2-3	$\tan\phi$	1	3-4	$\tan\phi$	3
	3-4	θ_4	2	4-5	θ_5	2
				5-6	θ_6	3

* $C = 30\ 1/3$, $h = 2 - 1/3$, $e = 9/8$, $B = 27,360$ lb and inch units. $\lambda \approx 0.45$

** Ref. Table VII for calculation of roll angles.

37

EXPERIMENTAL EVALUATION OF TRACTION EFFECTS UPON ROLLING FATIGUE LIFE

A limited experimental program was undertaken to determine if traction in the surface contact would have a significant detrimental effect upon rolling fatigue life. No attempt was made to test sufficient samples to obtain a statistically significant comparison. An overall look at the problem was indicated to determine if effects greatly differing from theory might occur.

DESCRIPTION OF TEST

An existing FIRL rolling contact (RC) testing machine, shown in Figure 13, was used for the experimental evaluation. This is a modified RC rig based on the principles of the well known RC rig.[12] Modifications consist primarily of a much huskier machine capable of much higher specimen loadings and the addition of timing belt drives to the large contact wheels (Figure 14). The bottom shaft of Figure 14, which is belt connected to the wheels, has a vane pump mounted on the rear of the rig. Traction in the contact was obtained by torque loading the lower shaft with the hydraulic pump working against a restrictor valve. The capability of the test rig and description of instrumentation are given in Table IX. The geometry of the rolling and traction test is shown in Figure 15. A 3/4-in.-diameter cylindrical test specimen is loaded between 7-1/2-in.-diameter test wheels. The geometry, including effect of the testing machine, materials, and lubricant used, is summarized in Table X. The test load, speed, Hertz contact stress, and elasto-hydrodynamic (EHD) oil film conditions are summarized in Table XI.

A footprint check of the load cell readout on the testing machine was made. Table XII summarizes the results of the footprints and presents a favorable comparison with calculated values of the contact areas between the test specimen and the contacting wheels. This common footprint technique consists of a light flash (0.0001 in.) copper plating of the cylindrical test specimen. Static loading of the test specimens by the two loading wheels results in a burnished and observable contact ellipse area. Measurement of this area by means of a traveling microscope with vernier allows close correlation between the load cell readout located below the scissors of the loading arms of Figure 14 and the actual elastic contact area of the testing conditions. The good correlation obtained assured that the load cell readout on the instrument panel was valid.

TEST RESULTS

The result of 17 test specimens with pure rolling and with rolling associated with traction in the contact are summarized in Table XIII. This table is a chronological history of the testing, and it may be noted that whenever failures were encountered in the test wheels, the wheels

38
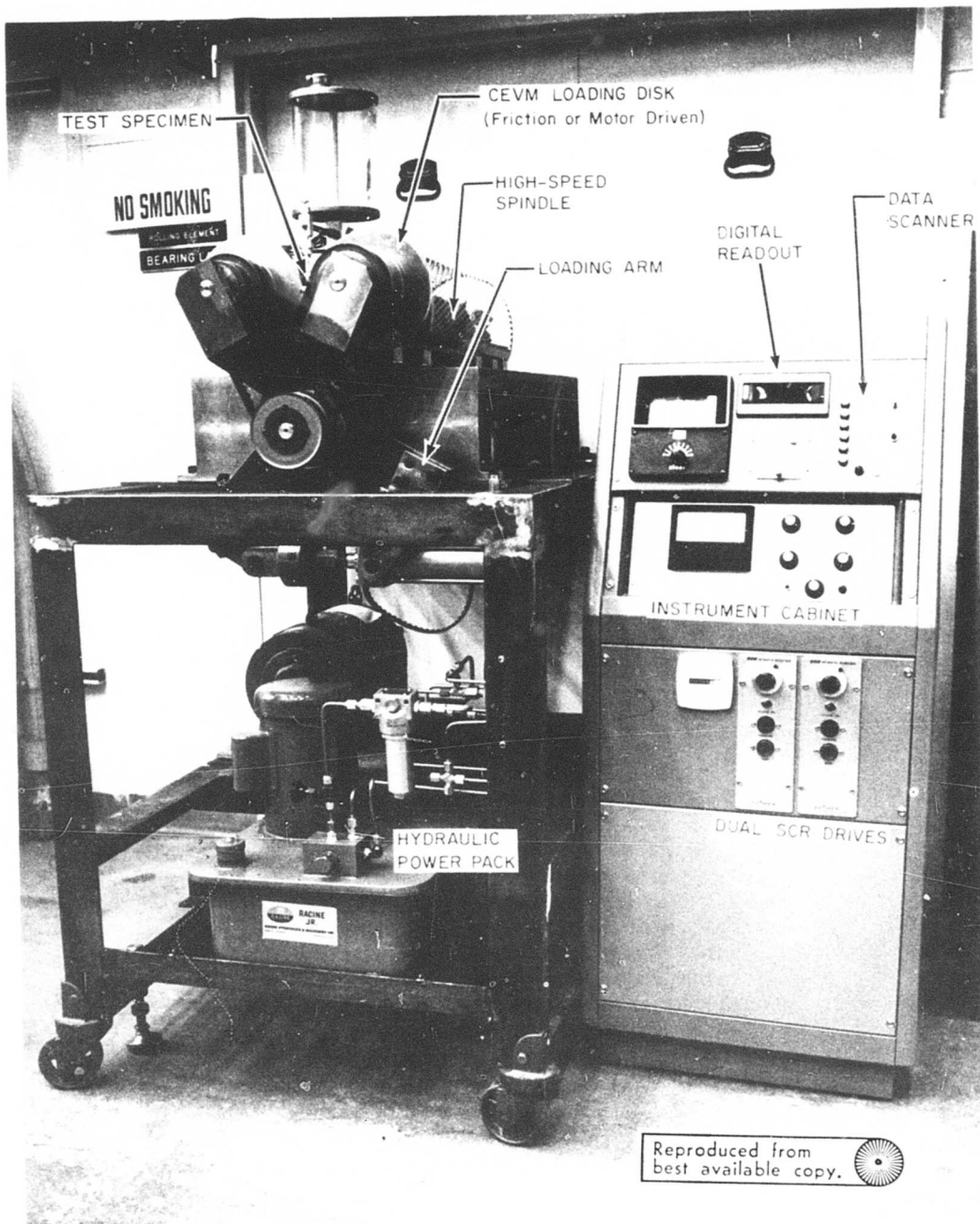
Figure 13. FIRL Rolling Contact (RC) Testing Machine.
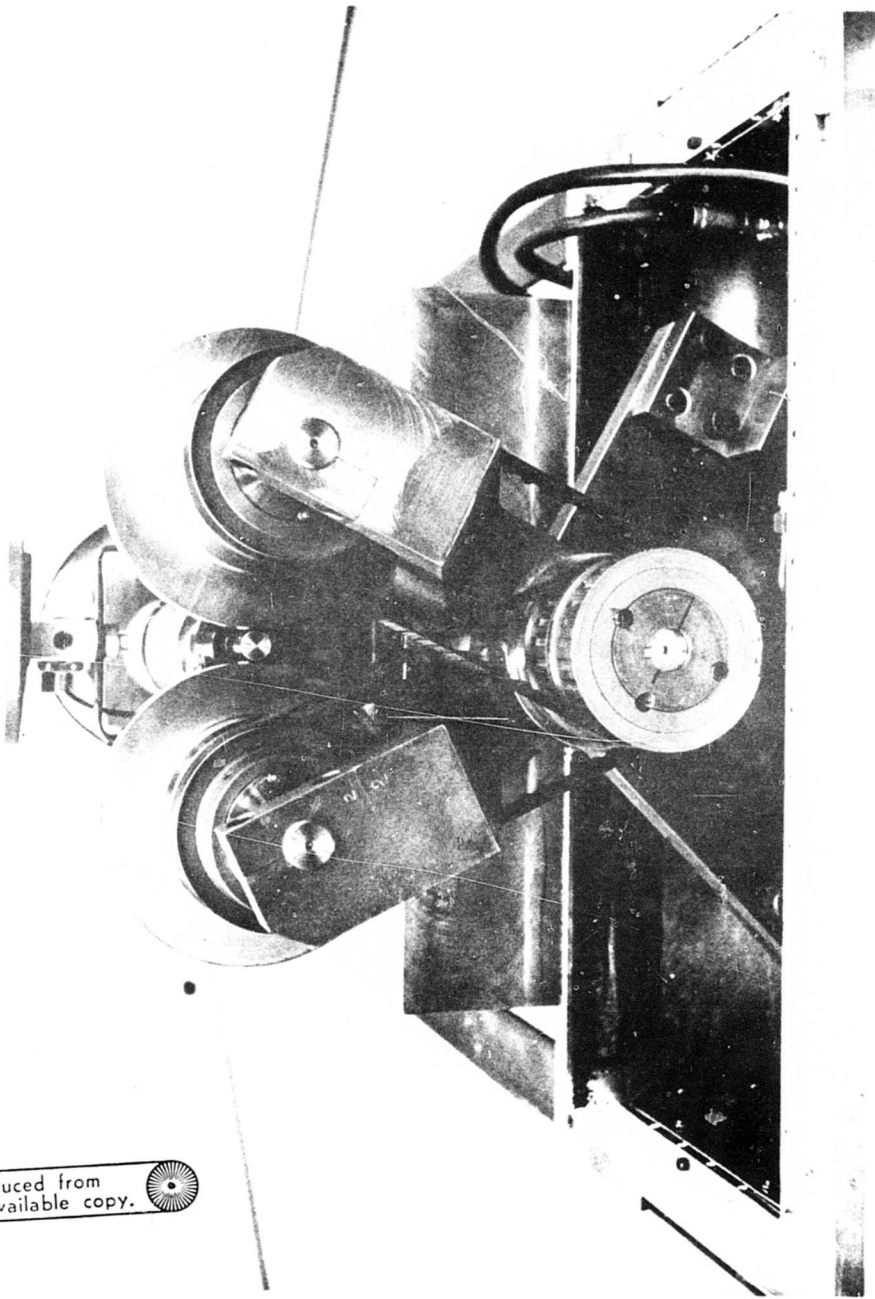
Figure 14. FIRL Modified RC Testing Machine.

40

TABLE IX. FIRL TRACTION TESTING MACHINE CAPABILITY

High-Speed Spindle	100-10,000 RPM
Speed Regulation	±1% No Load to Full Load
	3HP SCR Drive
Low-Speed Spindle	100-2500 RPM
Speed Regulation	±1% No Load to Full Load
	3HP SCR Drive
Test Load	0 to 3000 Lb
Load Cell Accuracy	1/4 of 1%
High-Speed Spindle, Torque	54 Inch-Lb ±1%
Low-Speed Spindle, Torque	108 Inch-Lb ±1%

Instrumented with Elapsed Time Meter and
Piezoelectric Accelerometer for
Automatic Shutoff Upon Test Specimen Failure
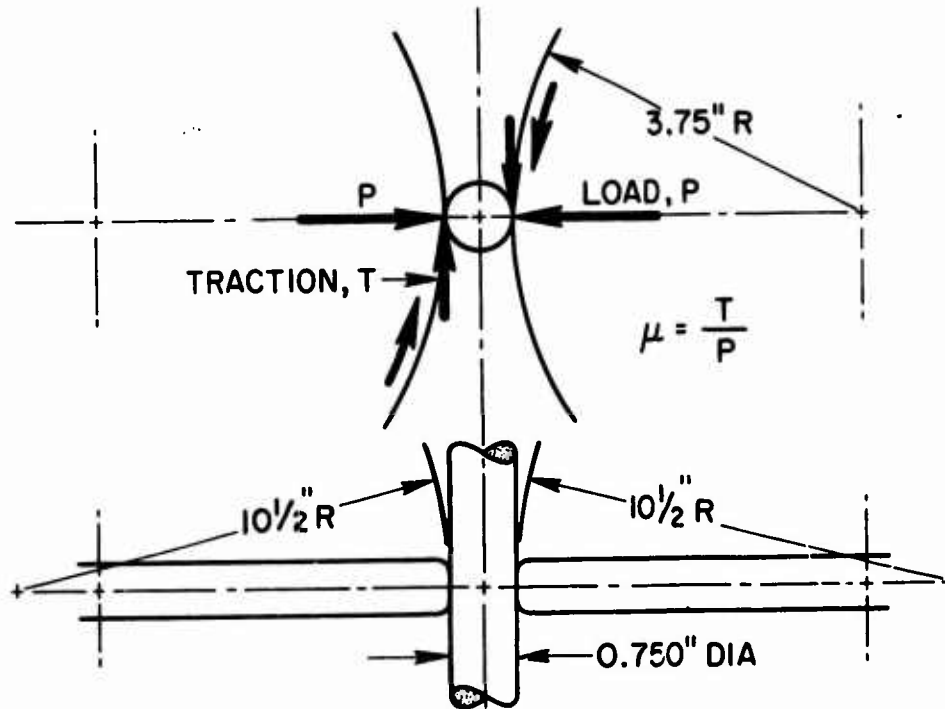
Figure 15.   Rolling and Traction Test.

41

TABLE X. TEST GEOMETRY, MATERIAL, AND LUBRICANT

	Test Specimen	Wheels
Size	3/4" Dia. X 3.0" Lg.	7-1/2" Dia. X 0.5" Wide
Crown Radius	∞	10.5 In.
Material	M-50 CEVM (AMS 6490)	M-50 CEVM (AMS 6490)
Surface Finish RMS	12	8
Hardness	RC 61 min.	RC 61 min.
Lubricant	MIL-L-7808 Oil @80°F	

TABLE XI. TEST LOAD, STRESS, AND EHD FILM CONDITIONS

Load	2000 lb
Speed	1800 RPM
Coeff. of Traction	0.06
Max Hertz Contact Stress	393,495 psi
EHD Oil Film	5.1×10^{-6} In.
Specific Film $= \dfrac{h}{\sqrt{\sigma_1^2 + \sigma_2^2}} \approx$	0.36

TABLE XII. COMPARISON OF CONTACT ELLIPSE FOOTPRINTS WITH THEORY		
	Length of Contact Ellipse 2a (In.)	Width of Contact Ellipse 2b (In.)
Footprint 1	0.291	0.034
Footprint 2	0.292	0.032
Footprint 3	0.302	0.032
Footprint 4	0.302	0.030
Avg.	0.297	0.032
Calculated Values	0.296	0.0328

were redressed or reground to their original 8-rms surface finish prior to continuing testing with new samples. The cylindrical test samples were marked "A" and "B" on the ends. In general, the "A" end was used for rolling tests with no traction and the "B" end of the test specimen was used for the rolling and traction tests. This provides a random effect of materials upon the results. All of the test specimens were obtained from the same heat of steel. Two pairs of test wheels were used. All four test wheels were made from the same heat of steel.

A summary of the eight rolling test specimens and their history is shown in Table XIV. It should be noted that five of the eight test specimens were continued to a fatigue type failure. Table XV is the Weibull statistical analysis of the rolling specimens according to Reference 13. These statistical results are plotted on standard Weibull paper on Figure 16.

TABLE XIII. EXPERIMENTAL RESULTS

Date	Specimen Number	Fatigue Failure	RPM	Torque in.-lb	Running Time hr	Remarks
Original Test Wheels RCT - 100597-101-162						
2-23-71 2-26-71	1A	Yes	1800-1811	4.1-5.08	65.7	Specimen failed.
3-1-71 3-2-71	2A	Yes	1802-1812	0.67-1.27	37.7	Specimen failed.
3-3-71 3-5-71	7A	Yes	1802-1811	0.25-0.63	111.7	Specimen failed
3-9-71 3-19-71	3A	No	1800-1811	0.86-2.2	259.0	Stopped test - Brgs in wheel support filed - Rig vibration caused skid damage.
Original Test Wheels RCT - 100597-102 - 162						
3-25-71 4-6-71	5A	Yes	1800-1818	.06-1.40	208.5	Specimen failed.
4-6-71 5-5-71	6A	No	1801-1819	1.15-3.08	677.0	Discontinued test.
5-5-71 5-17-71	2B	Yes	1734-1834	88.3-92.0	197.6	Wheels failed - Specimen damaged by wheels.
5-21-71	Wheels Reground.		RCT-100597-101-1 RCT-100597-101-2	7.5095" Dia. matched to 0.0002" on Dia. 10.500" Crown radius.		
5-21-71 5-25-71	6B	Yes	1730-1757	88.8-91.2	102.25	Wheels and specimen pitted.
5-26-71	Wheels Reground.		RCT-100597-102-1 RCT-100597-102-2	7.4755" Dia. matched to .0002" 10.500 in. crown radius.		
5-27-71	1B	No	1815-1837	2.91-3.55	187.5	Discontinued test.
6-3-71	4B	No Test	1735	91.75	.0.1	Test rig failure Wheel seized - failed wheel and specimen.

Preceding page blank

Date	Test No. / Condition	Specimen No.	RPM	%	Hours	Remarks
5-25-71	6B — Yes		1736-1757	86.0-91.2	102.25	(cut off)
5-26-71	Wheels Reground.	RCT-100597-102-1 / RCT-100597-102-2				7.4755" Dia. matched to .0002" 10.500 in. crown radius.
5-27-71	1B — No		1815-1837	2.91-5.55	187.5	Discontinued test.
6-3-71	4B — No Test		1735	91.75	0.1	Test rig failure. Wheel seized - failed wheel and specimen.
6-8-71	Wheels Reground.	RCT-100597-101-1 / RCT-100597-101-2				7.5030" Dia. matched. 10.500" Crown radius.
5-8-71	7B — No Test		~1800	Traction Test	>0.1	Traction torque applied by error at low loading. Stick-slip damaged wheels and specimens.
6-9-71	Wheels Reground.	RCT-100597-102-1 / RCT-100597-102-2				7.429" Dia. - Matched. 10.500" Crown radius.
6-9-71 / 6-14-71	8B — Yes		1758-1790	87.0-91.50	97.0 Motor Charge 245.1	Stopped test @ 97.0 hr. Electric motor arcing - High resistance joints in commutator. Switched to 3600 RPM drive 1/2 stepdown. Wheel failure.
6-23-71			1601-1612	89.4-90.8		
6-23-71	Wheels Reground.	RCT-100597-101-1 / RCT-100597-101-2				7.4968" Matched. 10.500" Crown radius.
6-23-71	9B — No		1596-1600	86.25-92.08	171.7	Surface distress on specimen.
6-30-71 / 7-1-71	10B — No		1540-1617	88.03-91.8	309.5	Surface effects on specimen.
7-14-71	11B — Yes		1538-1550	87.0-91.48	234.1	Wheel failed.
8-6-71	Wheels Reground.	RC-100597-102-1 / RC-100597-102-2				7.3793" Dia. matched. 10.500" Rad. crown.
8-6-71	12B — Yes		1591-1625	85.6-91.6	341.2	Wheel and specimen failed.
8-7-71	Wheels Reground.	RCT-100597-101-1 / RCT-100597-101-2				7.489" matched. 10.500" crown radius.
8-24-71 / 8-30-71	13B — Yes		1754-1845	78.0-88.60	35.5	Wheel failed. 1800 RPM motor reinstalled. 1/1 drive pulley ratio.
9-1-71	Wheels Reground.	RCT-100597-101-1 / RCT-100597-101-2				7.4305" Dia. matched. 10.500" Radius crown.
9-1-71 / 9-9-71	14B — No		1726-1760	85.03-90.04	191.6	Discontinued test.
9-10-71 / 10-20-71	15A — Yes		1804-1830	.28-2.80	793.7	Rolling test (no traction). Specimen examined periodically and returned to test at: 75.3 hr — 362.9 hr, 119.8 hr — 431.5 hr, 149.2 hr — 502.2 hr, 224.4 hr — 591.7 hr, 274.1 hr — 706.3 hr, — 774.9 hr. 793.7 hr wheel failure in 101-2.

Date	Specimen	Reground	Part No.	Range	Charge	Remarks
6-9-71 6-14-71	8B	Yes	1758-1790	87.0-91.50	97.0 Motor Charge 245.1	Stopped test @ 97.0 hr. Electric motor arcing - High resistance joints in commutator. Switched to 3600 RPM drive 1/2 stepdown. Wheel failure.
6-23-71			1601-1612	99.4-90.8		
6-23-71	Wheels Reground.		RCT-100597-101-1 RCT-100597-101-2			7.4968" Matched. 10.500" Crown radius.
6-23-71	9B	No	1596-1600	86.25-92.08	171.7	Surface distress on specimen.
6-30-71 7-1-71	10B	No	1540-1617	88.03-91.8	309.5	Surface effects on specimen.
7-14-71	11B	Yes	1538-1550	87.0-91.48	234.1	Wheel failed.
8-6-71	Wheels Reground.		RC-100597-102-1 RC-100597-102-2			7.3793" Dia. matched. 10.500" Rad. crown.
8-6-71	12B	Yes	1591-1625	85.6-91.6	341.2	Wheel and specimen failed.
8-7-71	Wheels Reground.		RCT-100597-101-1 RCT-100597-101-2			7.489" matched. 10.500" crown radius.
8-24-71 8-30-71	13B	Yes	1754-1845	78.0-88.60	35.5	Wheel failed. 1800 RPM motor reinstalled. 1/1 drive pulley ratio.
9-1-71	Wheels Reground.		RCT-100597-101-1 RCT-100597-101-2			7.4305" Dia. matched. 10.500" Radius crown.
9-1-71 9-9-71	14B	No	1726-1760	85.03-90.04	191.6	Discontinued test.
9-10-71 10-20-71	15A	Yes	1804-1830	.28-2.80	793.7	Rolling test (no traction). Specimen examined periodically and returned to test at: 75.3 hr 362.9 hr; 119.8 hr 431.5 hr; 149.2 hr 502.2 hr; 224.4 hr 591.7 hr; 274.1 hr 706.3 hr; 774.9 hr. 793.7 hr wheel failure in 101-2.
10-20-71	End of testing.					

TABLE XIV. SUMMARY OF ROLLING TEST RESULTS

Specimen No.	Fatigue Failure	Hours @1800 RPM	Remarks
1A	Yes	65.7	Specimen Failed
2A	Yes	37.7	Specimen Failed
7A	Yes	111.7	Specimen Failed
3A	No	259.0	Rig Failure-Discontinued
5A	Yes	208.5	Specimen Failed
6A	No	677.0	Discontinued Test
1B	No	187.5	Rig Failure-Discontinued
15A	Yes	793.7	Wheel Failure

Rolling test specimen 15A was the last specimen tested. This specimen was removed from test at periodic intervals (see Table XIII), and the surface condition was recorded by means of a scanning electron microscope (SEM). Thus, the progression of surface deterioration with time prior to a spalling fatigue type failure was observed. This special failure observation is reported in detail in a later section of the report.

The traction test specimens are summarized in Table XVI. Nine specimens were tested with traction and six were continued through failure. The failures with the traction samples were predominantly wheel type spalling fatigue failures. Rolling contact life theory would tend to predict specimen failures because of the additional number of stress repetitions per revolution of the test specimen as compared to stress repetitions of the testing wheels. Theory would indicate that the test wheels should have approximately 25 times the life of the individual test specimens assuming an equal probability of failure between the specimen and wheel. The reason for the predominance of wheel failures is unexplained at this time. All of the tractive loads were applied by loading the lower spindle of Figure 14. Thus, no tests were run with a reversal of the traction with respect to the rolling direction. It has been commented in some gear literature[14] that there is a preference for pitting failure when the direction of sliding is opposite to the

TABLE XV.	WEIBULL STATISTICAL ANALYSIS OF ROLLING CONTACT BEARING LIFE BASED ON MEDIAN RANK PLOTTING POSITIONS

ROLLING SPECIMENS MIL-L-7808 OIL

NUMBER OF BEARINGS TESTED =   8 FAILURE INDEX =   5

ORDER NO.	MEDIAN RANK	HOURS LIFE
.100000+01	.829960-01	.377000+02
.200000+01	.202140+00	.657000+02
.300000+01	.321284+00	.111100+03
.420000+01	.464257+00	.208500+03
.660000+01	.750202+00	.793700+03

BEARING LIFE VALUES WITH 90PERCENT CONFIDENCE BANDS

	HOURS LIFE	LOWER BAND	UPPER BAND
L(10)LIFE=	.348458+02	.476814+01	.185286+03
L(50)LIFE=	.271692+03	.118462+03	.576598+03

WEIBULL SLOPE =   .917282+00
ORDER NO. CK =   .900000+01
AVER.LIFE. HRS =   .425267+03
CORRELATION CK =   .973549+00

INPUT DATA	INDEX	TEST LIFE HRS.	(0=FAILED .1=NOT FAILED)
	0	.377000+02	
	0	.657000+02	
	0	.111100+03	
	1	.187500+03	
	0	.208500+03	
	1	.259000+03	
	1	.677000+03	
	0	.793700+03	

Preceding page blank
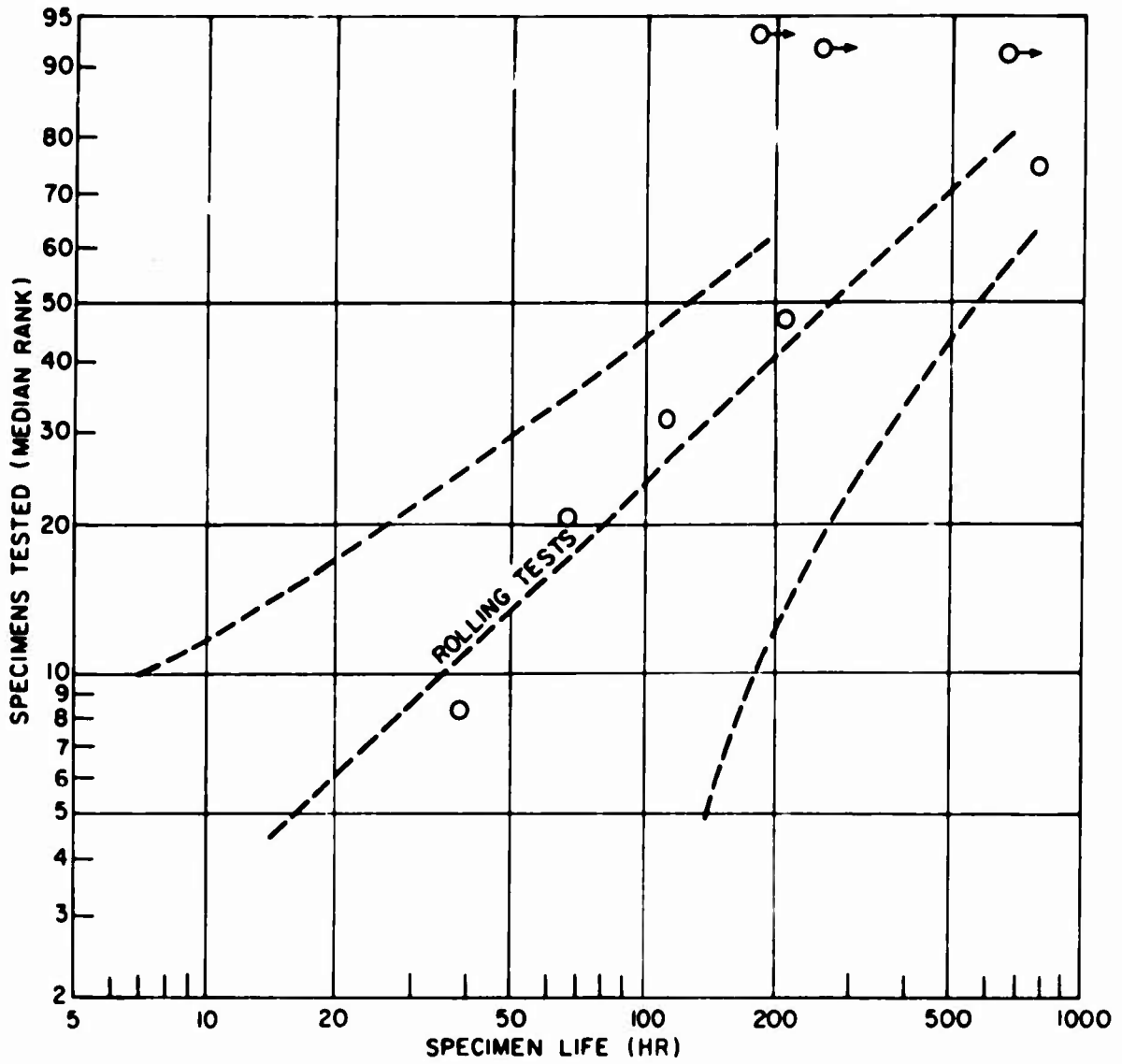
Figure 16.   Weibull Plot of Rolling Tests.

50

direction of rolling on the tooth contact. The conditions in the test
rig essentially result in the direction of impending sliding on the wheels
being opposite to the direction of rolling and may be a partial explanation
for the predominance of failures in the wheel surfaces. During initial
testing to determine the amount of traction that could be applied, it
was noted that when the coefficient of traction at the lubricated
contact exceeded approximately 0.065, a stick slip condition resulted in
large fluctuations in the torque and immediate destruction (a matter of
seconds) of the specimen and wheel surfaces. Therefore, all tests were
conducted with traction associated with rolling that would allow no gross
sliding in the contacts. The Weibull statistical analysis of the traction
specimens is summarized in Table XVII and presented graphically on
Weibull paper in Figure 17.

| TABLE XVI.   SUMMARY OF TRACTION TEST RESULTS |||||
Specimen No.	Fatigue Failure	Hours[*] @1800 RPM	Remarks
2B	Yes	197.6	Wheel Failure
6B	Yes	102.25	Wheel And Specimen Failure
8B	Yes	228.6[*]	Wheel Failure
9B	No	152.6[*]	Some Surface Distress
10B	No	275.1[*]	Some Surface Distress
11B	Yes	208.1[*]	Wheel Failure
12B	Yes	303.3[*]	Wheel And Specimen Failure
13B	Yes	35.5	Wheel Failure
14B	No	191.6	Discontinued Test

[*]Hours Life Adjusted By (1600/1800) Factor.

The comparison of the rolling and traction test results is shown
graphically on Weibull paper in Figure 18. It is immediately apparent
that no clear-cut statistically significant results can be expected.
Figure 18 with the 90% confidence bands essentially shows that the two
test conditions plot one on top of the other so that the slight increase
of life at the 10% probability of failure level with traction is
completely reversed or less life at the 50% probability of failure level
with the traction samples. The fact that the 90% confidence bands are
essentially symmetric and contained with respect to each other indicates
that no statistical significance could possibly be formed with the

51

TABLE XVII.	WEIBULL STATISTICAL ANALYSIS OF ROLLING CONTACT BEARING LIFE BASED ON MEDIAN RANK PLOTTING POSITIONS

TRACTION SPECIMENS   MIL-L-7808 OIL

NUMBER OF BEARINGS TESTED =   9   FAILURE INDEX =   6

ORDER NO.	MEDIAN RANK	HOURS LIFE
.100000+01	.741253-01	.355000+02
.200000+01	.180594+00	.102250+03
.333333+01	.322552+00	.197600+03
.466667+01	.464510+00	.208100+03
.600000+01	.606469+00	.228600+03
.800000+01	.819406+00	.303300+03

BEARING LIFE VALUES WITH 90PERCENT CONFIDENCE BANDS

	HOURS LIFE	LOWER BAND	UPPER BAND
L(10)LIFE=	.578135+02	.133233+02	.157449+03
L(50)LIFE=	.204761+03	.125023+03	.321040+03

WEIBULL SLOPE =   .148966+01
ORDER NO. CN =   .100000+02
AVER.LIFE. HRS =   .236609+03
CORRELATION CN =   .936134+00

INPUT DATA	INDEX	TEST LIFE HRS.	(0=FAILED .1=NOT FAILED)
	0	.355000+02	
	0	.102250+03	
	1	.152600+03	
	1	.191600+03	
	0	.197600+03	
	0	.208100+03	
	0	.228600+03	
	1	.275100+03	
	0	.303300+03	
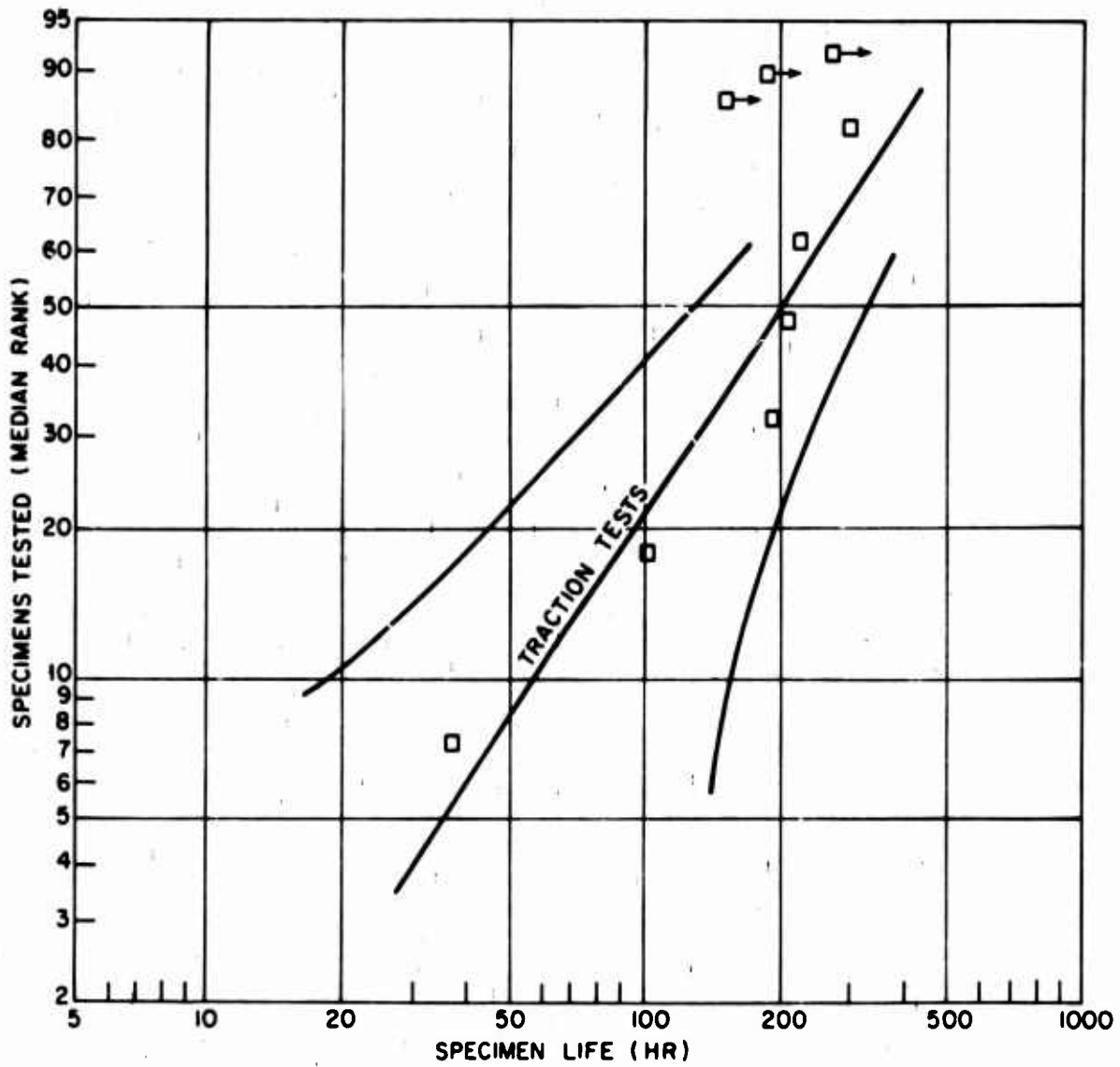
Figure 17. Weibull Plot of Traction Tests.
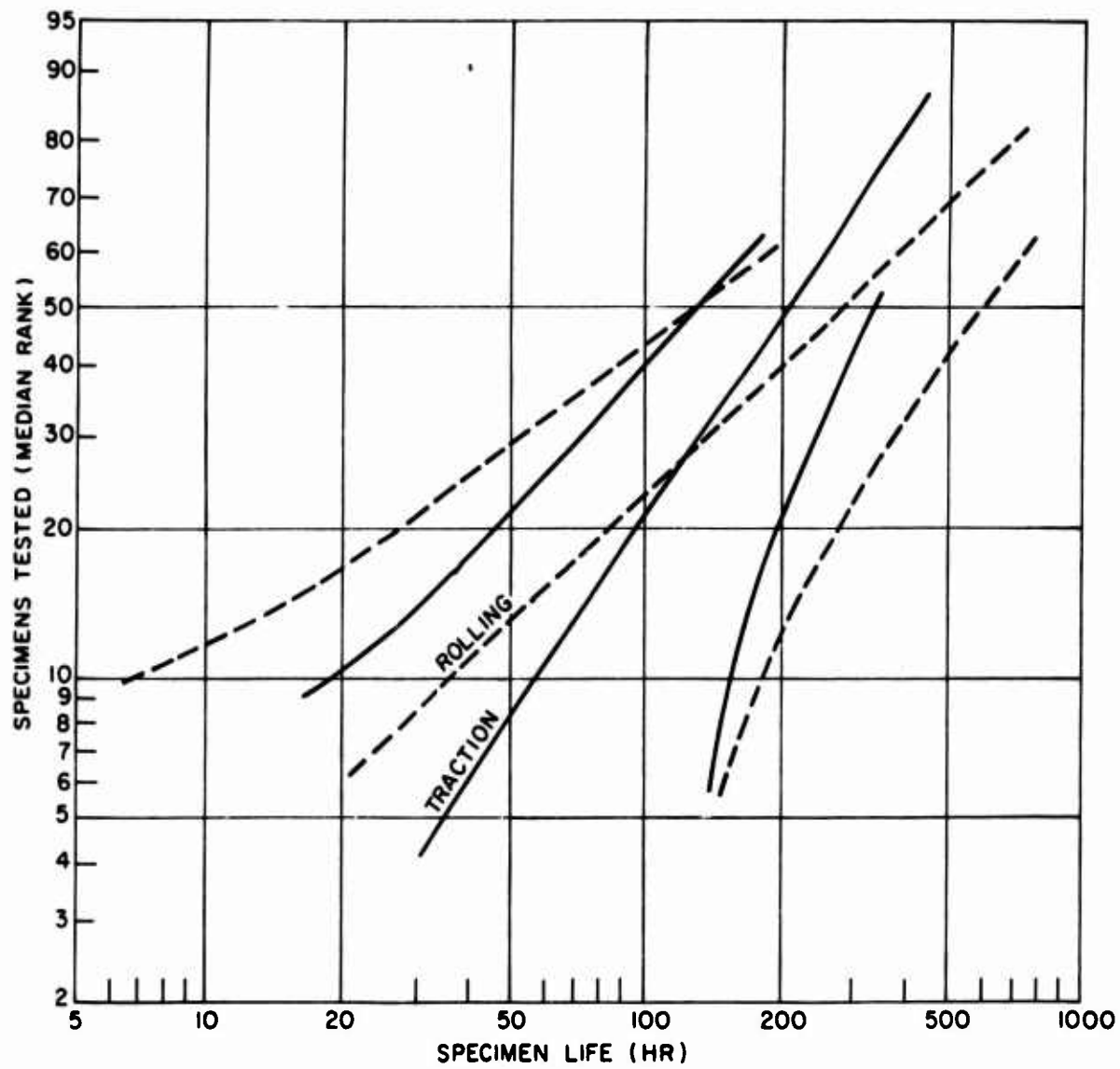
Figure 18. Comparison of Test Results.

available limited number of tests which would shed light on the effect of traction upon fatigue life. However, it is evident from Figure 18 and the results of the analysis of Tables XV and XVII that for the conditions explored, no significant reduction in rolling fatigue life was experienced. Therefore, a simplification of the gear life formula by assuming a zero coefficient of traction is not unreasonable at this time.

ANALYTICAL DETERMINATION OF MATERIAL CONSTANT FOR GEAR LIFE

The formulation of the gear life model as summarized in Table VII contains a material constant, B*. The test results to date can be used to get an indication of the magnitude of this material constant. The approach is to expand the load-life law of Equation 1 in a manner similar to that done to obtain the spur gear dynamic capacity. This expansion of the load-life law is then made to fit the specific geometry of the RC test rig (Figures 13 and 14). The detailed treatment is given in the equations below, resulting in the value of 27,360 pound and inch units (Eq. 98) which is contained in the spur gear dynamic capacity summary of Table VIII. This same approach can be used to correlate with fatigue life data from Buckingham[15] or other sources such as the Caterpiller roller gear test machine.

$$\log \frac{1}{S} \sim \frac{\tau_o^c \, N^e V}{z_o^h} \tag{1}$$

$$\tau_o = T_o \, \sigma_z \max = \frac{2 T_o \, P_N}{\pi \ell_{eff} b} \tag{38}$$

$$z_o = \xi b \tag{39}$$

$$b = \left[\frac{P_N \left(\frac{1}{E_1'} + \frac{1}{E_2'} \right)}{\pi \, \ell_{eff} \, \Sigma \rho} \right]^{1/2} \tag{43}$$

$$V = \ell_{eff} \, z_o \, \pi \, D_n \tag{37}$$

$$N = uL \tag{40}$$

55

Then by substitution,

$$\log \frac{1}{S} \sim \frac{A_1 T_o^c P^{\frac{c-h+1}{2}}}{\xi_o^{h-1}} \ell_{eff}^{\frac{-c+h+1}{2}} u^e L^e \pi^e D_n \Sigma_\rho^{\frac{c+h-1}{2}} \qquad [90]$$

Introducing a material constant B* and rearranging results in

$$P_N L^{\frac{2e}{c-h+1}} = B* \ (\log \frac{1}{S})^{\frac{2}{c-h+1}} \left[\frac{\xi_o^{h-1}}{T_o^c A_1} \right]^{\frac{2}{c-h+1}} \ell_{eff}^{\frac{c-h-1}{c-h+1}} \left[\pi D_n u^e \right]^{\frac{2}{c+h-1}} \Sigma_\rho^{\frac{c+h-1}{c-h+1}} \qquad [91]$$

For $L = 1.0 \times 10^6$ million cycles and introducing the currently accepted values,

$$c = 10-1/3$$
$$h = 4-1/3$$
$$e = 9/8$$

$$Q = B* \ [\log \frac{1}{S}]^{2/8} \left[\frac{\xi_o^{4/3}}{T_o^{31/3} A_1} \right]^{2/9} \ell_{eff}^{7/9} \ [\pi D_n]^{-2/9} u^{-1/4} \Sigma_\rho^{\frac{-35}{27}} \qquad [92]$$

where $Q = P_N$ is then the *dynamic capacity* or load that can be sustained for one million revolutions of the test specimen.

Evaluation of the material constant B* can now be accomplished using the RC rig test results.

$$B* \ [\log \frac{1}{S}]^{2/9} \left[\frac{\xi_o^{4/3}}{T_o^{3\ 1/3} A_1} \right]^{2/9} = Q \ \ell_{eff}^{-7/9} \ [\pi D_n]^{2/9} \ u^{1/4} \ \Sigma_\rho^{35/27} \qquad [93]$$

pound and inch units.

The formula for computing the life of a rolling contact specimen in line contact can be expressed in terms of the capacity Q and applied load P as

$$H_{10} = \frac{(\frac{Q}{P})^4 \times 10^6}{60 \times RPM} \qquad \text{Hours} \qquad [94]$$

56

where

$$Q = \left[\frac{H_{10} \times 60 \times RPM}{10^6}\right]^{1/4} \times P \qquad (1b) \qquad [95]$$

The H_{10} life of the rolling test specimens (Table XV) was 35 hours with 90% probability of survival. M50 CEVM steel is generally accepted to have approximately 5 times the life of ordinary air melt steels. The test life for typical gear steel (nonvacuum processed) can be taken as

$$H_{10} \cong 5 \text{ hr} \qquad [96]$$

Then

$$Q = \left[\frac{5 \times 60 \times 1800}{10^6}\right]^{1/4} (2000) = 1714 \text{ lb} \qquad [97]$$

The various constants for the RC test rig are (Table XII):

ℓ_{eff} = effective length of contact = 0.296 in.

D_n = diameter of race path = 0.750 in.

u = stress repetitions per revolution = 2

$$\Sigma_p = \frac{1}{R_A} + \frac{1}{R_B} = \frac{1}{0.375} + \frac{1}{3.75} = 2.9333$$

$$B^* \ [\log \tfrac{1}{S}]^{2/9} \left[\frac{\xi_o^{4/3}}{T_o^{31/3} A_1}\right]^{2/9} = \frac{(1714)[(\pi)(0.750)]^{2/9}(2)^{1/4}(2.9333)^{35/27}}{(0.296)^{7/9}} \qquad [98]$$

$$= 27,360 \text{ lb and in. units}$$

57

FAILURE INVESTIGATION AND CLASSIFICATION

SCANNING ELECTRON MICROSCOPY ANALYSIS

A new apparatus was designed and constructed in order to facilitate
characterization of rolling contact test elements by scanning electron
microscope (SEM) techniques. A view of this equipment appears in
Figure 19. The end of the specimen to be examined is inserted into a
sleeve cap, and the other end is supported by an adjustable free spindle
on which it can rotate freely. A small 6-volt D.C. motor is coupled
through a slow-speed gear drive arrangement to the sleeve cap. The
friction fit within the sleeve assures rotation of the cylindrical speci-
men when the motor is operating. The entire assembly shown in the
figure fits into the standard stage of the JSM-2 SEM. Electrical con-
tacts have been positioned within the SEM in such a way that the motor
can be operated by a small battery and switch arrangement outside the
microscope. The full width of the specimen's wear track can be observed
in the SEM through use of the X-Y microscope controls, and the entire
track can be examined by appropriate use of these controls in conjunction
with the motorized specimen rotation. The test wear tracks are clearly
visible in the specimen shown in the holder in Figure 19. There is also
a spall evident on the top of the track at the sleeve end of the cylinder.
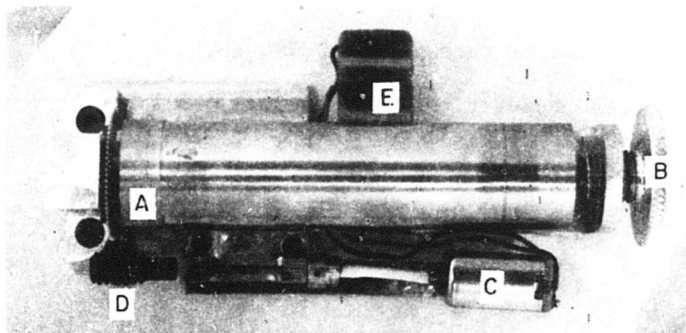
APPROX. 0.9X

A SLEEVE CUP
B LIVE SPINDLE
C SMALL 6V D.C. MOTOR
D SPEED REDUCING GEAR TRAIN
E ELECTRICAL CONTACTS FOR POWER
SUPPLY EXTERNAL TO THE SEM

Figure 19. SEM Sample Holder With a Spalled Specimen in Place.

By indexing both the sleeve and the specimen, changes in the wear surface at specific locations as a function of the running time in an interrupted test regime were catalogued and are discussed below.

With the aid of the specially designed specimen holder in the SEM, 15 specimens were thoroughly analyzed. The surfaces and failure types were characterized, and micrographs were taken of typical examples of various features. A tabulation of the observations is found in Table XVIII, and a more complete discussion of the results is given below. Each test is first considered individually, and then comprehensive conclusions are presented. In order to evaluate the surface alterations induced by running, representative SEM micrographs of the as-finished surfaces are presented in Figure 20. The grinding process produced a surface characterized by finishing lines and smeared metal. A similar finishing technique was employed on the test wheels, and the contacting surfaces should have been comparable. The large size of the wheels precluded direct observation in the SEM.

Specimen 1A: The large spall on this specimen is shown in the SEM micrograph of Figure 21. There are characteristics of both subsurface and surface initiation on this spall. The straight crack on the entrance side is indicative of surface inclusion initiation, while the general fracture surface appearance within the spall is similar to spalls in which no surface indications are found. Large spalls form in small segments, as is clearly shown by the sections in Figure 21 about to exfoliate and by the fracture surface details both in and opposite to the rolling direction as shown by surface cracking at both entrance and exit sides of spalls. Thus it is entirely possible for the spall to have originated near its center, where there are distinct morphology changes, and to have grown back to the apparent inclusion line. (In specimen 15A, surface fatigue was observed to propagate to scratches to yield a straight line boundary.)

The smoothed fracture surfaces within the spall (Figure 22) are evidence that the mating fracture surfaces rubbed against each other for many cycles before the cracks grew sufficiently to remove a piece of metal. On this basis it seems that the presence of as-fractured surfaces should be taken as evidence of the location for last stages of the failure process. Only one location near the bottom of the spall exhibited a fresh fracture, indicating that this spall as a whole may have been surface initiated. However, this location may also have been a secondary failure region of the entire spall, with evidence of near-surface, fresh fracture surfaces having been obliterated by subsequent spall growth. Accordingly, it is difficult to classify the spall as clearly either subsurface or surface in origin. Nevertheless, by gross appearance alone it would be classified as a "classical type" spall.

TABLE XVIII. SUMMARY OF METALLOGRAPHIC OBSERVATIONS

Specimen	Traction	Running Time (hr)	Wheel Condition	Failure Mode	General Surface Condition
1A	No	65.7	New	Spall	1 large spall; general glazing - many dents; very little surface distress.
2A	No	187.5	From Previous Run	Spall	Similar to 1A.
7A	No	111.1	From Previous Run	Spall	Similar to 1A.
5A	No	208.5	From Tests 1,2, 7 and 3A	Surface	No spalls; extensive surface distress.
6A	No	677.0	From 5A	None	Limited scattered surface distress and glazing; test terminated.
2B	Yes	197.6	From 6A	Wheel	Narrow band of surface distress; surface smearing; glazing.
6B	Yes	102.25	Reground	Wheel	Large patches of smeared metal from wheel; surface distress and glazing.
8B	Yes	228.6	Reground	Surface & Wheel	Surface distress; heavy glazing; 1 band of larger pits.
9B	Yes	152.6	Reground	Surface & Wheels	Large patches of surface distress; glazing; smearing; some regions had deeper pits; less severe than 8B.
10B	Yes	275.1	Reground	Surface	Center band of heavy surface distress; much less overall damage than 9B.
11B	Yes	208.1	From 10B	Surface & Wheels	Heavily smeared pieces of metal from wheel; surface distress and smearing between built-up metal; worst appearance of any test in absence of large spall.
12B	Yes	303.3	Reground	Surface & Wheels	General surface distress around very prominent large pitches and streaks of built-up metal.
13B	Yes	35.5	Reground	Wheel	Extensive denting from wheel failure; 2 narrow lines of raised, smeared metal; surface distress; less damage than 12B.
14B	Yes	191.6	Reground	Test Stopped	Patches of distress; least damage of all traction specimens.
15A	No	793.7	From 14B	Wheel	(Interrupted 11 times during

a) 300X
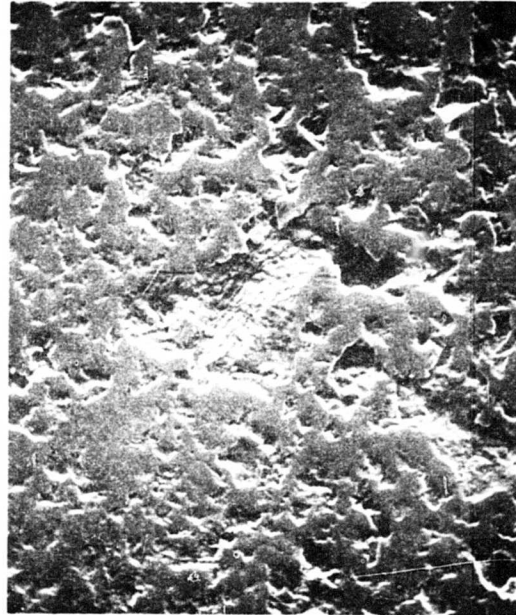
b) 1000X

Figure 20.   Representative Sample of As-Ground Surface of the Rolling
Contact Specimen Prior to Testing.
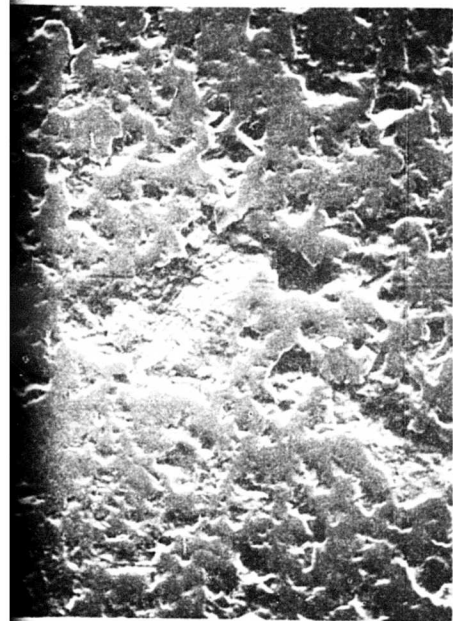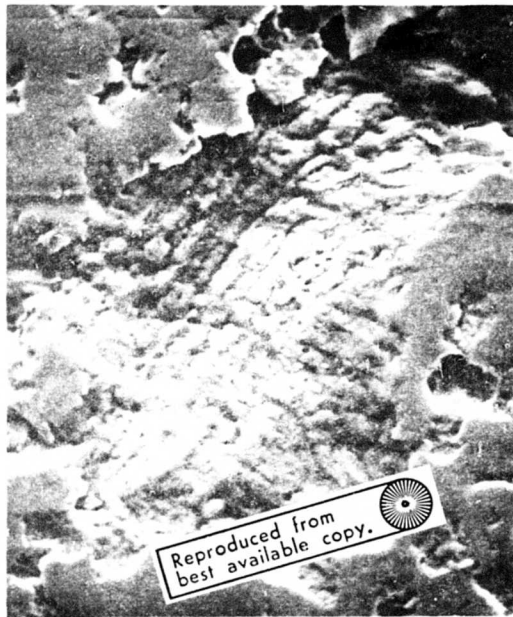
b) 1000X

c) 3000X

DIRECTION OF ROLL

urface of the Rolling
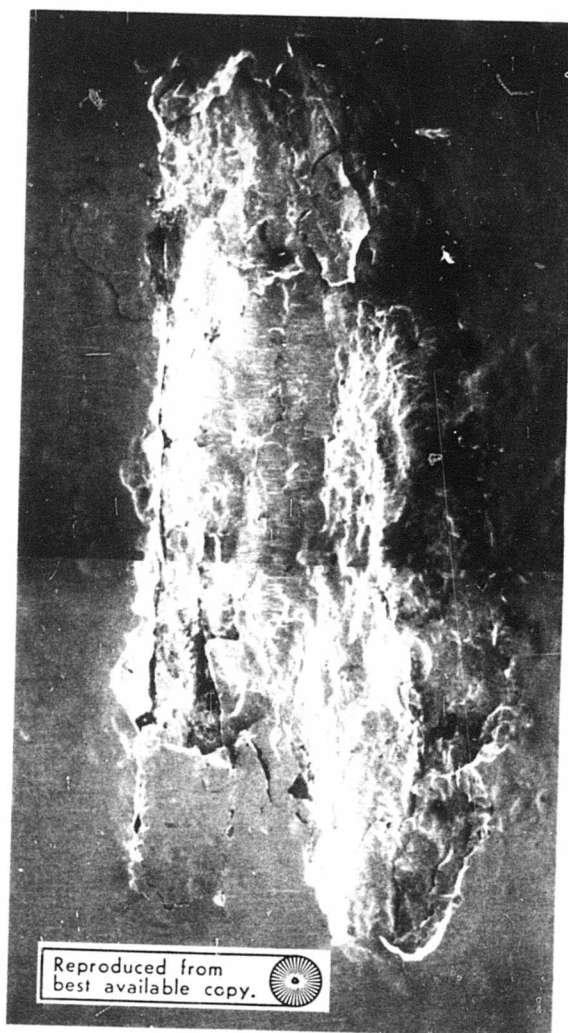
26 X

→

DIRECTION OF ROLL

Figure 21. Large Spall on Specimen 1A.

Preceding page blank

65

DIRECTION OF ROLL
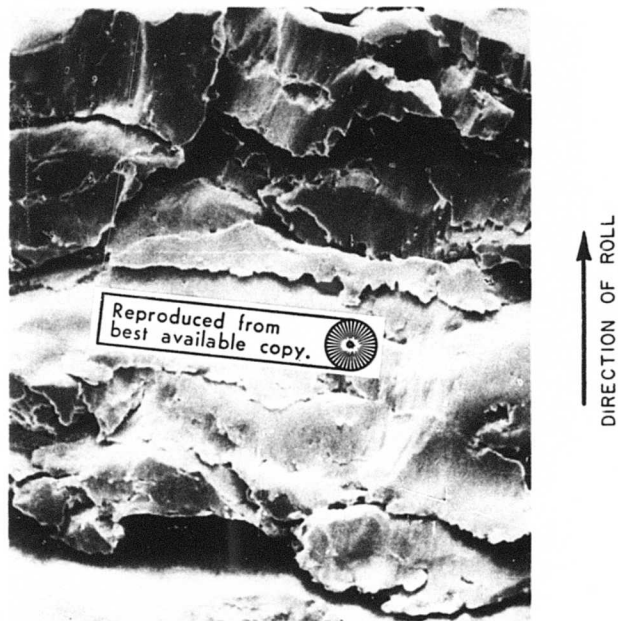
180X

Figure 22.   An Example of the Fragmentation and Plastic Deformation
of Specimen 1A.

The fragments of the spall led to many dents on the specimen as shown in
Figure 23.   Also apparent in the figure are the original finishing
characteristics which had not been severely altered in the relatively
brief running time.

Specimen 2A: This specimen spalled after the very brief running time of
37.7 hours.   The overall geometry of the spall, Figure 24, is different
from that in Figure 21 and essentially can be classified as "classical
subsurface" in origin.   However, the fine details within the spall were
similar to those discussed above for 1A and are consistent with either
a surface or a subsurface origin.   Figures 25 and 26 are examples of a
fracture surface which has not been completely rubbed or pressed smooth
in the failure process.   This region was found at one of the deeper areas
of the large spall and was the only such example found in this spall.
Thus it may represent a single isolated spall segment formed late in the
overall spalling sequence of events.

The surface was heavily dented and the original finishing marks are
clearly evident.   Extensive cracking at the exit end of the spall is
evident in Figure 24.

66

DIRECTION OF ROLL

b) 600X
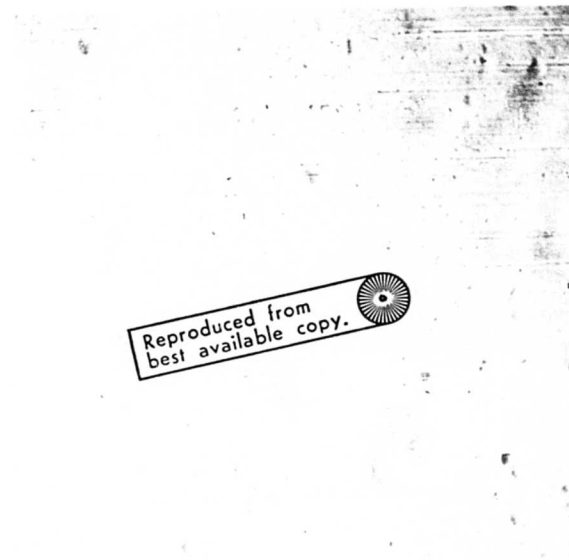
a) 180X

Figure 23. General Surface Appearance of Specimen 1A.

67
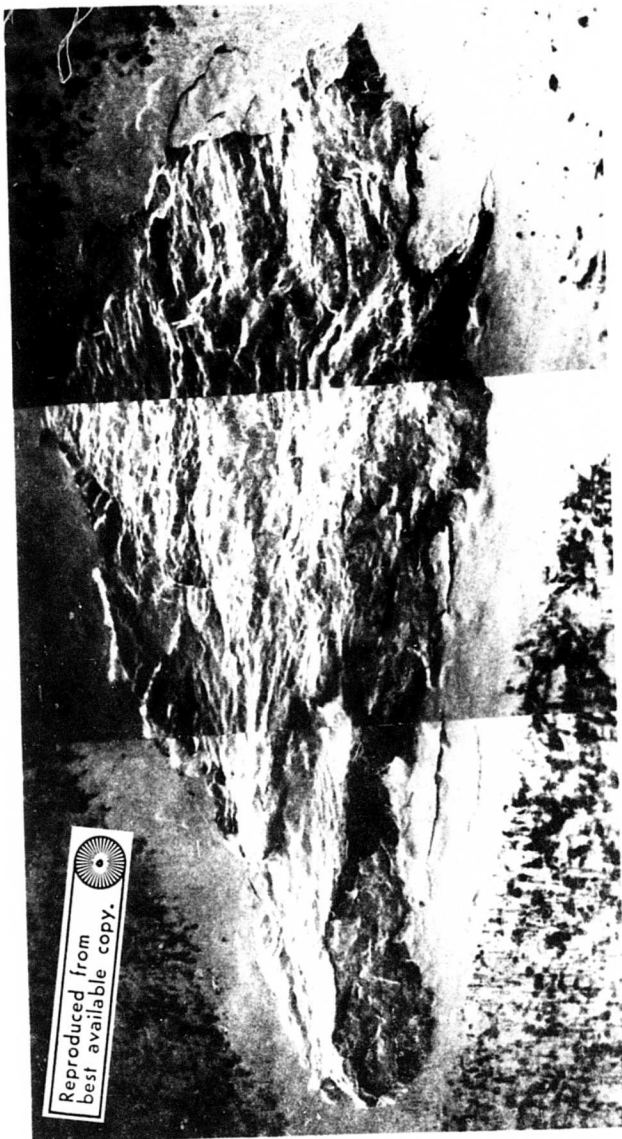
DIRECTION OF ROLL

26X

Figure 24. Specimen 2A Composite SEM Micrograph.

DIRECTION OF ROLL

180 X

Figure 25.   Fracture Surface Within the Spall of Figure 24.
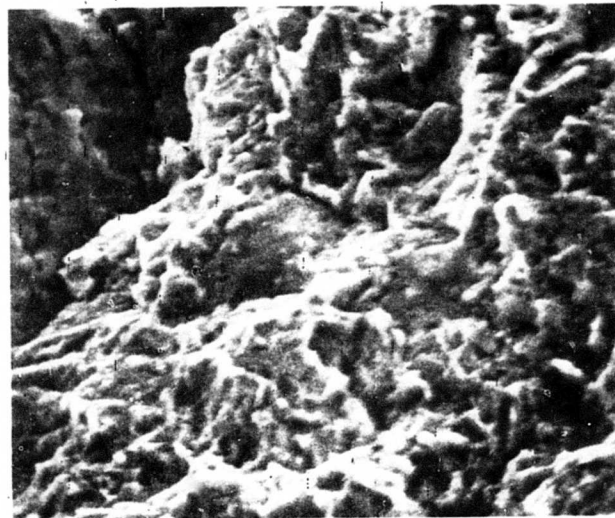
DIRECTION OF ROLL

6000 X

Figure 26.   Higher Magnification of Central Region of Figure 25.

69

Specimen 7A: This specimen was similar in appearance to 2A, exhibiting one large spall and much surface denting. Incipient spall growth was noted well before the entrance end of the spall as shown in Figure 27 and appears to have occurred in conjunction with the spall since no other evidence of such damage was found in the contact path. This cracking also seems to be surface nucleated from stress concentrations and lubricant deficiencies created by the presence of the spall.

Specimen 5A: There were no well-defined spalls, such as on the previous specimens, on this test element. However, there was a broad band of surface distress, also referred to as surface peeling, covering about half the contact surface and scattered patches of the surface distress over the remainder of the surface. Figure 28 illustrates the surface within the band of heavy surface distress. The higher magnification views show that the surface is composed of shallow spalling intermixed with heavy, plastically deformed, glazed original surface metal. At higher magnifications, what appear to be fatigue striations are in evidence. It is also possible to note that the surface regions bordering the peeled-off areas have been deformed to such an extent that they overhang the shallow depressions.

Specimen 6A: This specimen was similar in appearance to 5A, with the surface distress being less pronounced with regard to the fraction of the surface affected. Within the distressed regions the glazing was more pronounced, as is shown in Figure 29, than for Specimen 5A. This is probably due to the longer running time for 6A.

Specimen 2B: Unlike the previous specimens discussed, 2B was run under traction. Surface distress (Figure 30) was primarily confined to one narrow band in the contact area, and the glazed metal was heavily flowed over the shallow peeled spots, particularly at the edge of the band in Figure 30. Since wheels failed during this test run, it is difficult to assess the extent to which the heavy smearing of surface metal on the specimen is due to either the wheel failure or the presence of traction.

Specimen 6B: The surface of this specimen is marked with large patches of smeared metal which had peeled off the test wheels and then built up on the test specimen. The smearing was detectable by eye, but SEM was required to study its details. Careful scanning across the contact area on the specimen showed that surface distress had occurred on the specimen

70
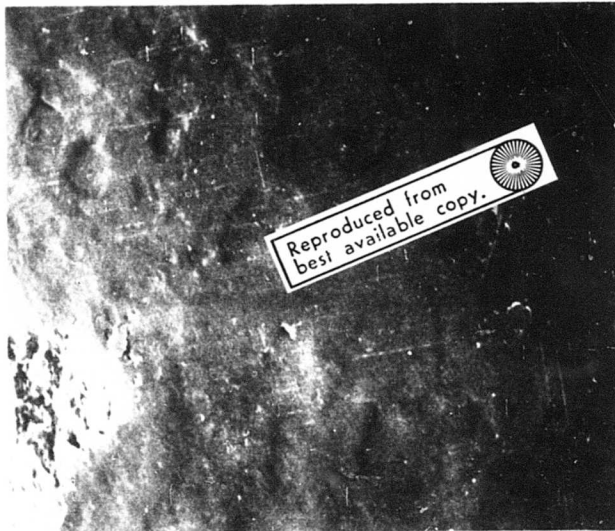
DIRECTION OF ROLL

b) 300X

a) 60X
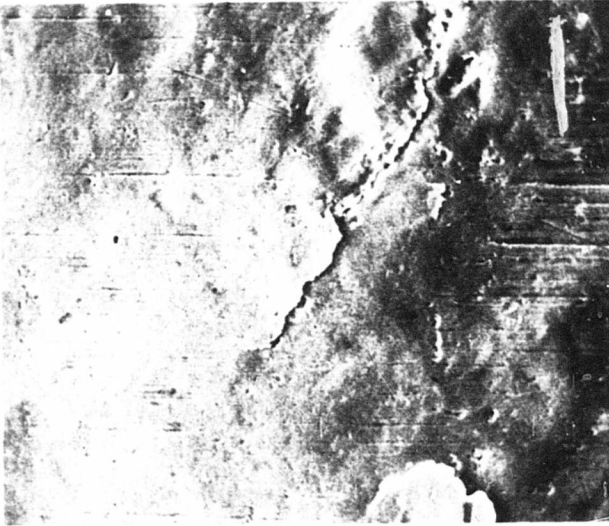
Figure 27. Entrance End of Large Spall on Specimen 7A.

71
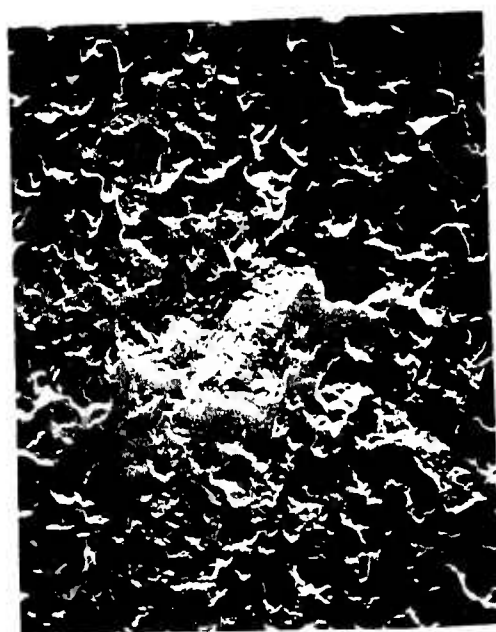
a) 100X   b) 300X

Figure 28.   Combined Surface Distress and Pr~ ~nced Plastic Deforma-
             tion and Glazing Covering Much   ~he Surface of Specimen 5A.
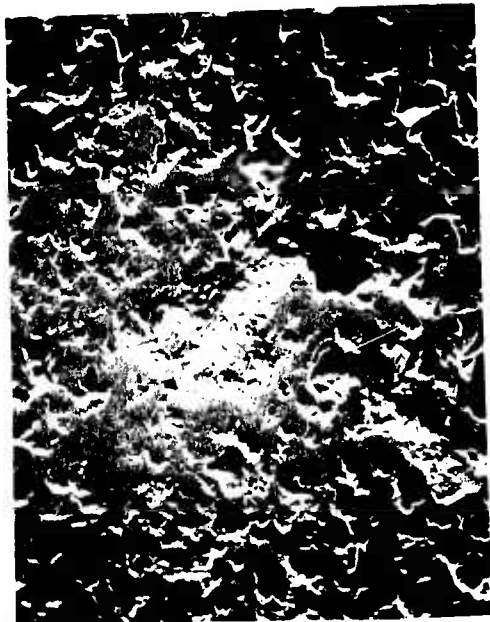
b) 300X

c) 1000X

DIRECTION OF ROLL

nounced Plastic Deforma-
the Surface of Specimen 5A.

DIRECTION OF ROLL

b) 800X

Reproduced from
best available copy.

a) 300X

Figure 29. Pronounced Plastic Deformation and Glazing Surround Peeled Regions
(Surface Distress) on Specimen 6A.

a) IOOX   b) 3OOX

Figure 30.   Band of Surface Distress and Heavily Flowed Glazed Metal on
Specimen 2B.

b) 300X

c) 1000X

DIRECTION OF ROLL

avily Flowed Glazed Metal on

prior to its picking up the smeared metal. However, the extent of the shallow spalling was much less than the elevated patches, indicating that the majority of the smeared metal must have originated on the wheels. In Figure 31 the background surface distress or peeling is evident and is on a much finer scale than the large patches adhering to the surface. It is very interesting to note the degree to which the particles of hardened M50 steel (>60R$_c$) from the wheel were plastically deformed and welded to the specimen under the high compressive forces in the contact area.

Specimen 8B: The entire surface of this specimen showed peeling and glazing. There were several bands of particularly heavy glazing surrounding larger pits as in the lower magnification micrograph in Figure 32. In the region away from the larger pits, the surface is relatively uniformly pitted and glazed over. There is also evidence in the higher magnification micrograph that some of the peeled areas have been filled in by smeared metal, which may have come from the wheels. Although the wheels required regrinding, there was no evidence of built-up metal on the specimen as in 6, 11 and 12B, run under similar conditions. There were also a few isolated pits visible by eye, but these were several magnitudes smaller and shallower than the spalls found in specimens 1, 2 and 7A.

Specimen 9B: This specimen was very similar to 8B with the qualification that the total extent of peeling, pitting and glazing was somewhat less pronounced, consistent with the shorter running time. There also were no individual pits visible to the eye.

Specimen 10B: This specimen had many of the features of 8B and 9B, but the total extent of surface alterations was significantly less. One band of heavier distress or peeling ran around the center of the contact area, with patches found elsewhere.

Specimen 11B: There were unique "chatter-like" ridges visible to the eye on this specimen. Examples are presented in Figure 33. In terms of overall gross damage in the absence of "classical" spalling, this specimen was the worst one examined. It was not possible to ascertain if all the metal in the ridges derived from the wheels since the regions between them were extensively smeared, unlike the condition described for specimen 6B. However, scanning across the wear path into the unrun region did not reveal any difference in elevation between the background regions separating the ridges and the unrun surface. This would indicate that the built-up metal came primarily from the wheels.

Specimen 12B: This specimen was also characterized by extensive smearing of built-up metal. However, the distribution of this metal was quite different from that present for specimens 6 and 11B. As shown in Figure 34, very long, narrow, continuous streaks of metal distinguished this specimen from the ones previously discussed. For this specimen, the presence of the original peeled or distressed surface indicates that the built-up metal originated primarily in the wheels.

b) 100X

a) 60X
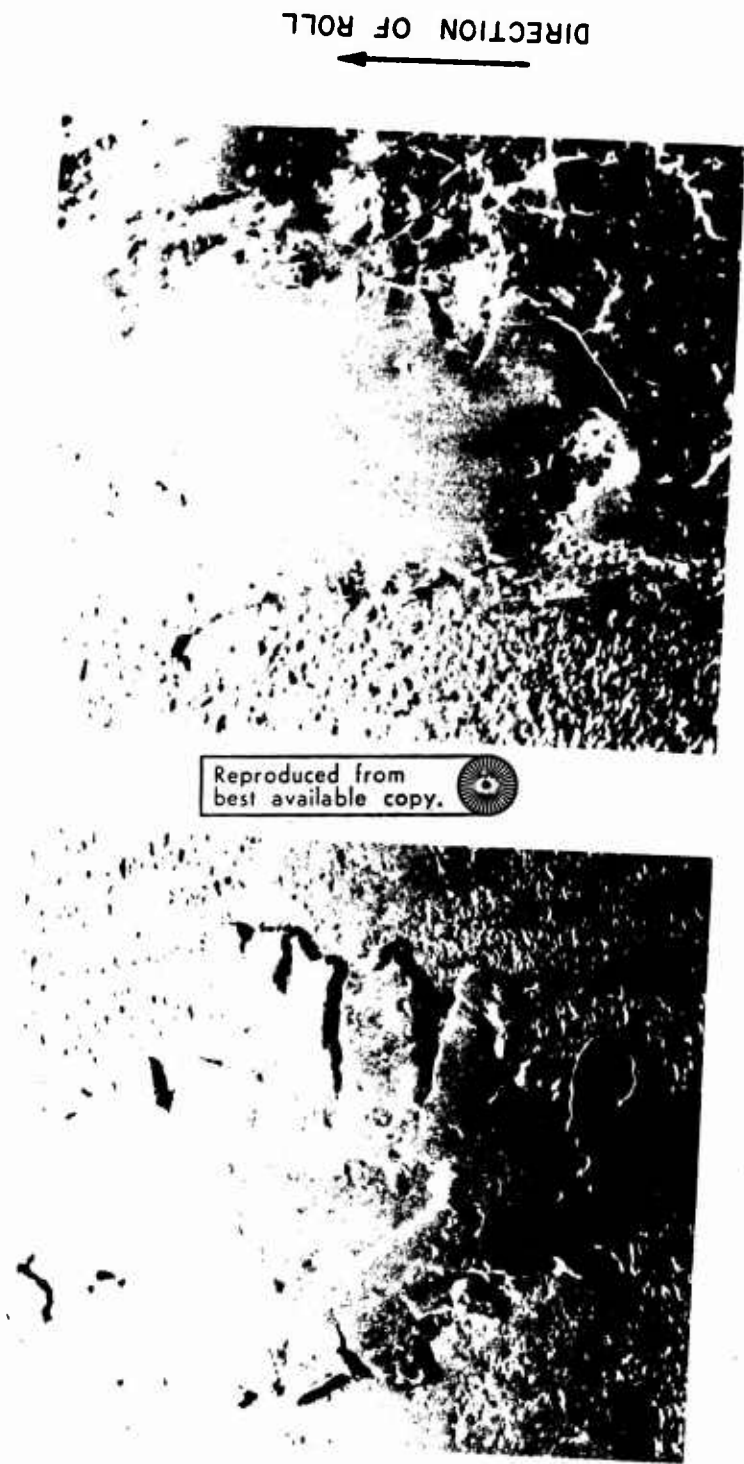
Figure 31. Two Examples of the Built-up Smeared Metal Noted on the Surface of
Specimen 6B.

DIRECTION OF ROLL

b) 300X

a) 100X

Figure 32. Pronounced Peeling Surface Distress and Accompanying Glazing Which Covered the Entire Contact Area of Specimen 8B.

81
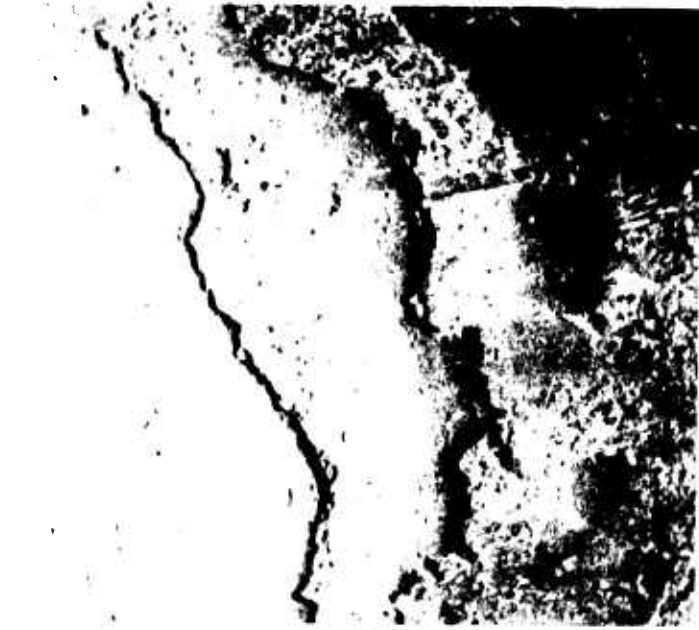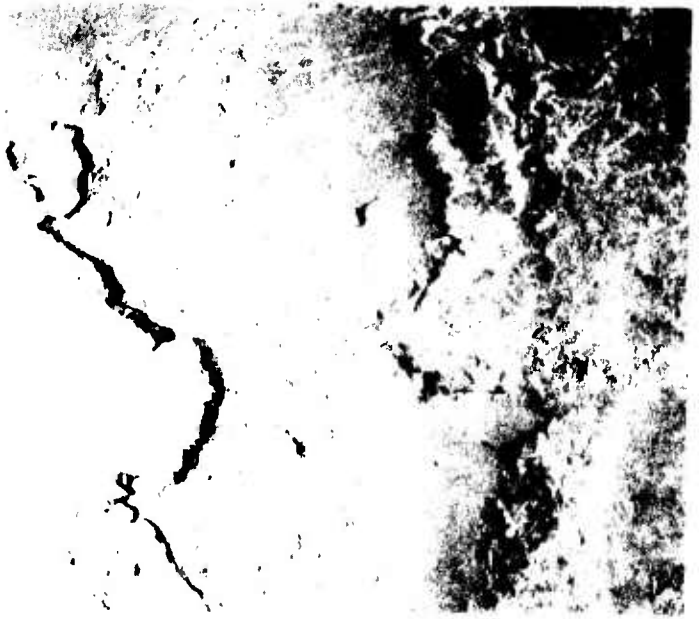
b) 47X

a) 47X

Figure 33. Examples of Built-up Ridges of Metal Found on Specimen 11B.

DIRECTION OF ROLL
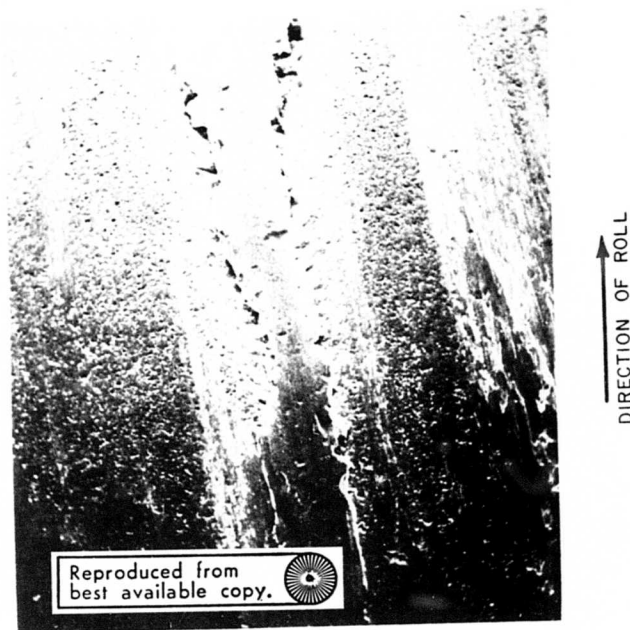
37 X

Figure 34.   An Example of the Streaks of Built-up, Smeared Metal Found
on the Surface of Specimen 12B.

Specimen 13B: There were two narrow lines of smeared metal encircling
the contact path.   The extent of this effect was much less than for
specimen 12B, and the majority of the surface showed denting (from wheel
failure), surface distress, and glazing much like specimen 8B.

Specimen 14B: With the exception of patches of moderate surface distress,
there was little alteration to the surface induced by the running.   There
was nothing to indicate why the wheels, after regrinding, ran well with
this specimen and failed early when running under essentially identical
conditions with 13B.

Specimen 15A: This specimen was run without traction and was examined
periodically during the test program.   A full discussion of the SEM
analysis of the testing regime is given below.

At the conclusion of the testing, the specimen surface was highly glazed,
was uniformly covered with patches of surface distress, and contained
an incipient spall.   Some of the glazing appears to have been associated
with a large spall on a wheel which terminated the test.   Since this was

83

the last test in this program, the wheel was not reground and thus was
available for detailed analysis. Figure 35 is a light micrograph
spall which had the same characteristics as those found on specimens 1,
2 and 7A. Since the wheel was too large for the SEM, a plastic replica
of the spall was made and examined. While this replica could not follow
all the multiple crack branching found within a spall, it did provide a
basis for concluding that this spall did have flattened fracture sur-
faces and characteristics essentially the same as those noted on the
test specimens. Also evident in the figure are the surface finishing
lines and the absence of any clear surface distress. This was in direct
contrast to the surface of 15A at the conclusion of running and undoubtedly
can be attributed to the relative sizes of the specimen and wheel.

DIRECTION OF ROLL

Reproduced from
best available copy.
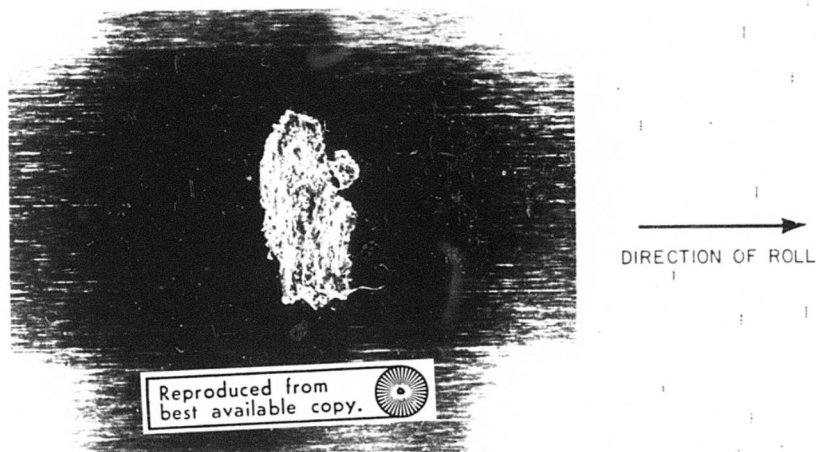
6X

Figure 35. Light Micrograph of Large Spall on Wheel at Termination of
Test 15A.

GENERAL OBSERVATIONS

A. Rolling Contact (No traction)

The first three test specimens (1, 2 and 7A) failed by what appeared to
be "classical" spalling modes. These specimens exhibited very little,
if any, surface distress (peeling). On the other hand, specimens 5
and 6A also ran without traction, ran for longer periods of time, did
not spall, but were characterized by surface distress. Specimen 6A ran 677
hours compared to 208.5 for 5A, yet showed much less surface peeling. This

transition from spalls to surface distress to little surface damage, if real and not subject to statistical happenstance, may have been the result of running-in of the test wheels. Such a running-in process would have led to a progressive relative difference in surface morphology between the wheels and each successive test specimen. Since it is difficult to propose another mechanism consistent with the observations, careful characterizations and control of relative surface finishes in future tests should be helpful in determining the true importance of surface finishing techniques and end results in practical life applications and also in insuring valid comparative testing conditions.

The nature of the fracture surfaces within large spalls and within the shallow peeling is significantly different. In the spalls, the surfaces were heavily deformed and smeared, indicating a metal-to-metal contact during the spall propagation process. Furthermore, the presence of many secondary cracks and small metal segments indicates a stepwise propagation process. Thus, each spall fragment may have been forced against the base metal during each successive loading cycle until it exfoliated. In contrast to this, the surfaces within peeled areas appeared to be relatively undeformed, but stepwise fracture details again appeared evident. Such stepwise fracture and undeformed fracture surfaces at first would seem to be inconsistent. However, by taking into account the specific geometry of the contact area, the stress distribution and particularly the presence of the lubricant between the cracking surfaces, it should be possible to develop a model for the peeling process. Further work would be required to generate research data to accomplish such a task.

The smooth fracture surfaces within the larger spalls may also be due to a number of factors such as the loading situation when deeper cracks are propagating and the absence of lubricant between fracture surfaces for subsurface crack initiation and propagation. Again pursuing this approach, further work should contribute much toward the understanding of and the designing against rolling contact fatigue.

B. Rolling Contact With Traction

In general, the traction tests resulted in surface distress on the test elements and the wheels, with the specimens often picking up the metal exfoliated from the wheels. No large spalls were formed on any traction specimens, even though most traction specimens experienced about the same running times as those specimens run without traction. It appears that surface peeling and any accommodation it produces may alleviate grosser scale spalling. If this is true, such knowledge would be of extreme importance in surface finishing considerations. However, these observations are based on limited testing and would require further work for substantiation.

INTERRUPTED TEST PROGRAM — SPECIMEN 15A

In order to obtain data, tests were run until a failure occurred either on the specimen or on a wheel. Post-test inspection of the specimens usually revealed relatively advanced forms of surface alterations, and therefore little could be learned concerning the sequence of events during run-in of the rolling elements and leading up to the failure processes. Since phenomena which occur early in rolling contact may play a major role in determining the life of a test element, it was decided to run specimen 15A under an interrupted test regime and sequentially examine surface alterations. In particular, any early modifications could be closely followed as a function of running time through the use of the special holder in the SEM.

The test was run under the standard no-traction condition, and the specimen was examined periodically as noted in Table XVIII. A series of SEM micrographs were taken for comparison purposes and are presented and discussed below. The initial surface of this specimen was the same as represented in Figure 20, and this micrograph should be referred to when considering the alterations evident in the micrographs taken after the various running times.

After the initial 75.3 hours of running, the major feature noted was the appearance of scattered small patches of shallow peeling or distress. As shown in Figure 36, these regions appear to result directly from asperities and smeared metal produced by grinding. The appearance of the fracture surfaces indicates a stepwise crack propagation, and segments in the process of cracking are plainly evident. In general, the surface was slightly glazed or flattened compared to its initial state.

After 119.8 hours there were a few more regions of peeling, with some being slightly more extensive. The surface as a whole showed little change; the deeper finishing marks were still plainly evident. Likewise, after 149.2 and 224.4 hours, very little further difference was noted. Thus, after the initial surface distress, which was apparently caused by asperity interaction between the specimen and the wheels, only a little further peeling or glazing was noted. It was evident that these small patches of distress do not necessarily cause stress concentrations of such an extent to make themselves self propagating at any appreciable rate. However, since fatigue is a continuous process, it is not to be expected that this condition should be completely stable. Nevertheless, it appears that the surface defects which are larger in area and appear to have a worse geometry than any features on the initial surface are much less damaging in terms of further damage than those initially on the surface. This must be related to an accommodation of the running surface that results when initial metal asperities are removed. From this, one can speculate that a very uniform and finely pitted surface in which high spots can deform into the valleys may be a better initial condition than a finely finished surface with a few asperities. Furthermore, it is interesting to note that in spite of its high hardness ($>R_c 60$),

86

a) 300X   b) 1000X   c)

Figure 36.   Typical Example of Peeled or Distressed Surface Damage on Specimen 15A After 75.3 Hours.
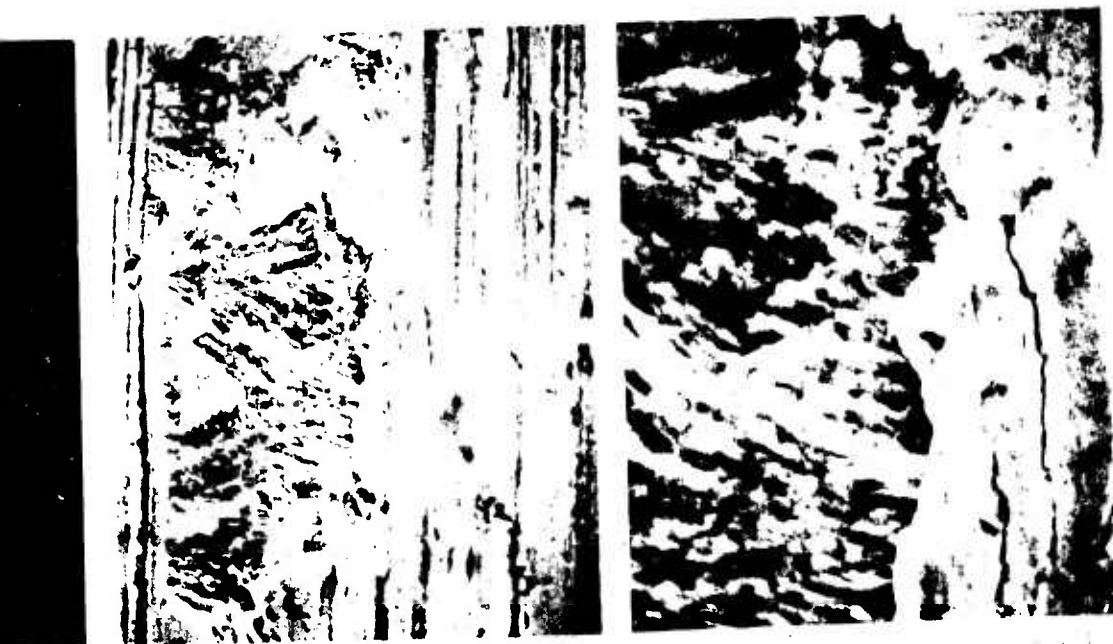
b) 1000X

c) 3000X

DIRECTION OF ROLL

r Distressed Surface Damage on
rs.

the M50 steel can plastically deform to such a large extent on a fine scale without cracking.

After 274.1 hours, a few larger patches of distress were noted; an example is given in Figure 37. The heavily glazed metal interspersed within the patches no longer shows the original surface markings. Some shallow, smeared lines introduced during handling of the specimen between test runs are evident in the glazed regions separating the peeled spots.

After 362.9 hours, the surface defect grouping shown in Figure 38 was noted. This defect appeared to have originated or stopped at a handling scratch. The progress of this defect was subsequently recorded at each examination cycle, and the resulting SEM micrographs appear in Figures 39, 40 and 41 at different magnifications. The lower magnification micrographs (Figure 39) indicate that the growth of the defect was very limited as a function of accumulated running time. At high magnification, Figure 40, the limited growth of the distressed region appears to be influenced by handling scratches. The last two micrographs of this series were taken after a spall had initiated on one of the test wheels. By comparing these micrographs with one representative of earlier stages in the test run, it can be seen that a marked degree of smoothing over and plastic spreading of the higher, nonpeeled surface had occurred. This was primarily from plastic flow rather than a wearing down of the elevated regions, since the lower, peeled spots appear smaller with time. The scratches which were prominent in the early stages were almost totally obliterated when the testing was suspended. Careful comparison of the 1000X micrographs (Figure 41), taken after several earlier stages in the surface deformation process, clearly reveals the extensive localized deformation, examples of which are indicated by the arrows.

After 431.5 hours, a large dent, probably caused by some debris which entered the contact area during running, was found while scanning the specimen in the SEM. The micrographs in Figure 42 reveal that shallow spalling occurred at one end (the exit end when considering the direction of rolling) of the dent. The fracture surfaces show signs of flattening, and the crack branching characteristic of larger spalls is evident. This region was sequentially examined after each subsequent testing period, and the micrographs appear in Figures 43, 44 and 45 at different levels of magnification. From the low magnification sequence in Figure 43, it is obvious that surface peeling was nucleated at the rim of the dent. The shallow spalling noted in the figure did not propagate deeper, as shown in Figures 44 and 45, but did lead to surface peeling and subsequent plastic flow of the higher surface regions much the same as discussed previously for the surface peeling defect in Figures 38 to 43. It appears that a form of compliancy may be responsible for the fact that the cracks at the bottom of the shallow spall did not propagate under the Hertzian stresses or from lubricant-induced hydraulic pressure propagation.

DIRECTION OF ROLL

b) 1000X

a) 300X

Figure 37. Representative Larger Patch of Peeling and Glazing Noted After 274.1 Hours of Running Specimen 15A.

90

a) 300X   b) 1000X

Figure 38.   Patch of Surface Peeling Noted After 362.9 Hours.

91

b) 1000X

c) 3000X

DIRECTION OF ROLL

oted After 362.9 Hours.
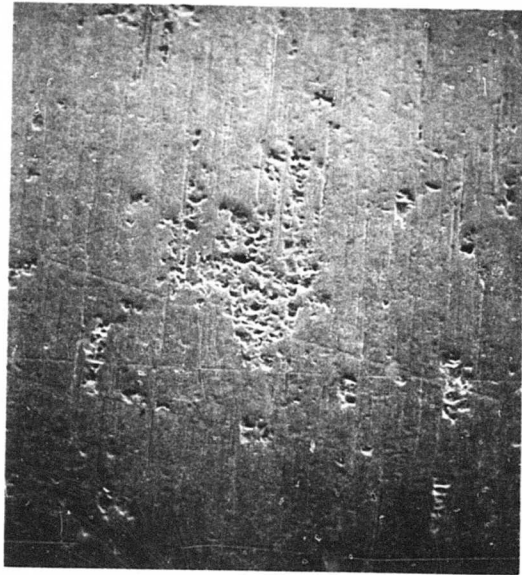
a) 431.5 HR.
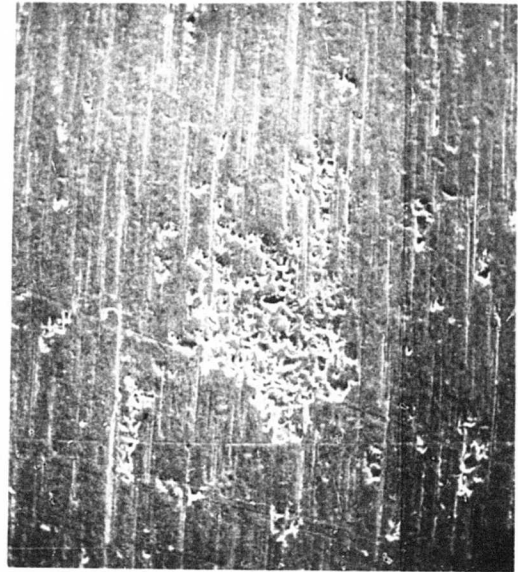
b) 502.2 HR.

d) 706.3 HR.

e) 774.9 HR.

Reproduced from
best available copy.

Figure 39. Sequential Views at 100X of a Specific Surface Peeling
Defect After Various Running Times.

b) 502.2 HR.
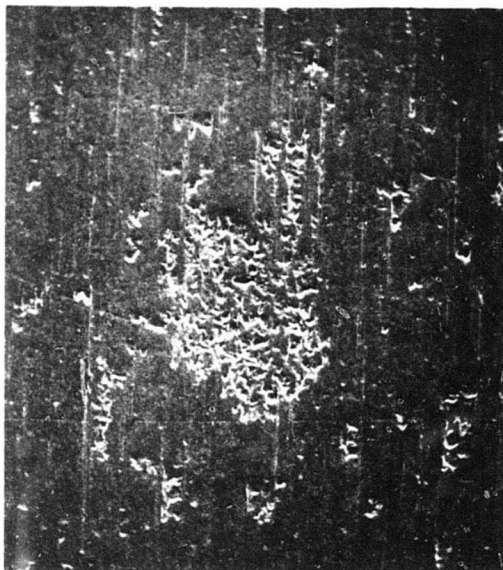
c) 591.7 HR.

DIRECTION OF ROLL

e) 774.9 HR.
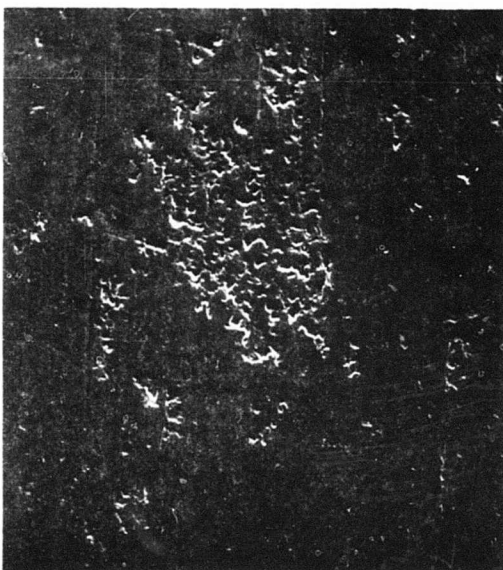
f) 793.7 HR.

DIRECTION OF ROLL

ecific Surface Peeling
es.
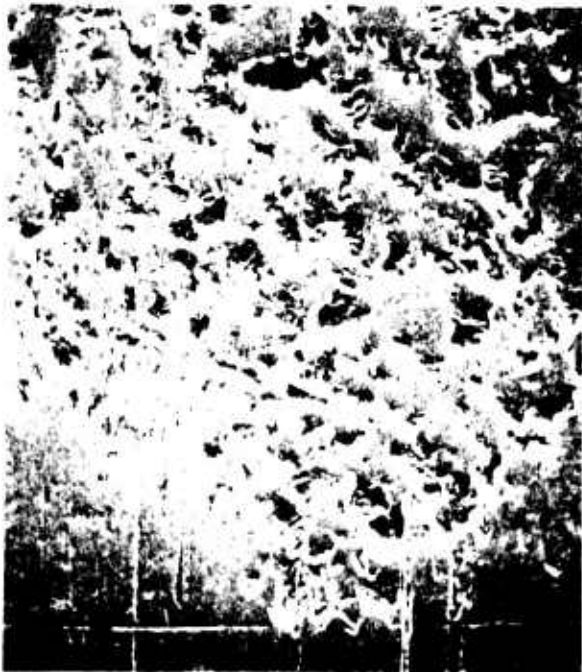
a) 362.9 HR.　　　　　　　　b) 431.5 HR.
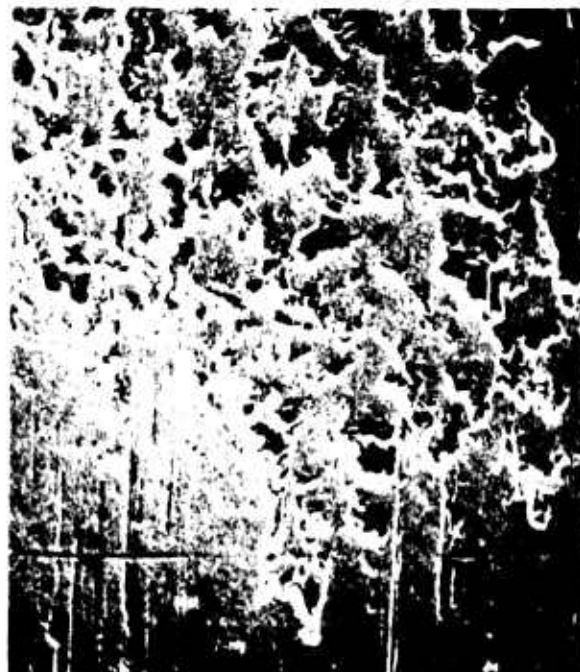
d) 591.7 HR.　　　　　　　　e) 706.3 HR.　　　　　　　　f)

Figure 40.　Sequential Views at 300X of a Specific Surface Peeling
Defect After Various Running Times.

b) 431.5 HR.

c) 502.2 HR.
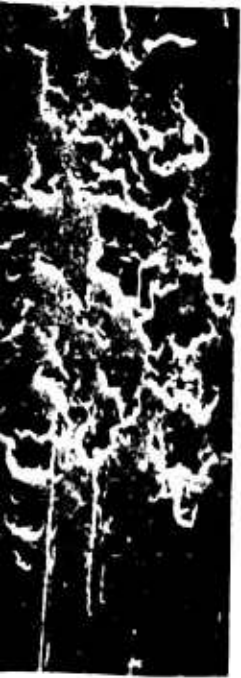
DIRECTION OF ROLL

HR.
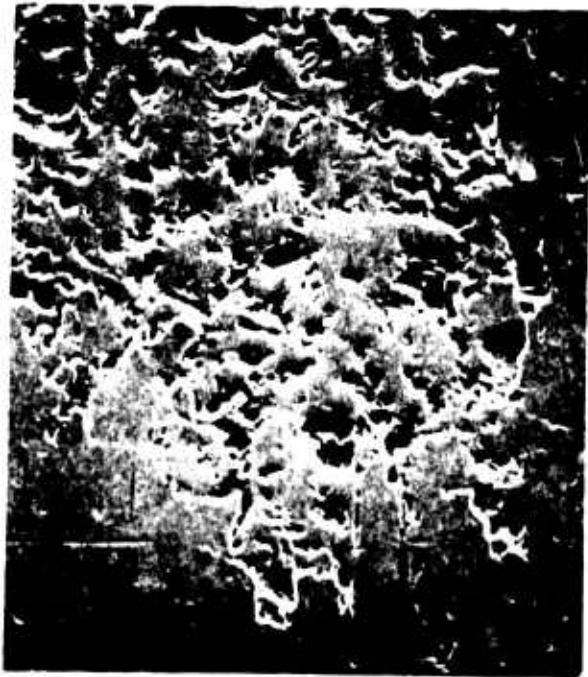
f) 774.9 HR

g) 793.7 HR.

DIRECTION OF ROLL

ng

a) 362 9 HR   b) 431.5 HR   c) 502 2 H

Figure 41. Sequential Views at 1000X of One Small Area Within the Surface Defect of Figures 39 and 40.

b) 431.5 HR.

c) 502.2 HR.

DIRECTION OF ROLL

One Small Area Within the
and 40.

a) 75X　　　　　　　b) 300X　　　　　　c) IC

Figure 42.　Dent Defect and Associated Shallow Spalling Noted After 431.5
Hours.

99

c) 1000X

d) 3000X

DIRECTION OF ROLL

a) 431.5 HR.   b) 502.2 HR.   c) 5

Figure 43.   Sequential Views at 300X of Shallow Spalling Occurring
at the Upper Boundary of the Dent in Figure 42.

c) 591.7 HR.

d) 706.3 HR

DIRECTION OF ROLL

a) 75X, 431.5 HR.

b) 100X, 502.2 HR.
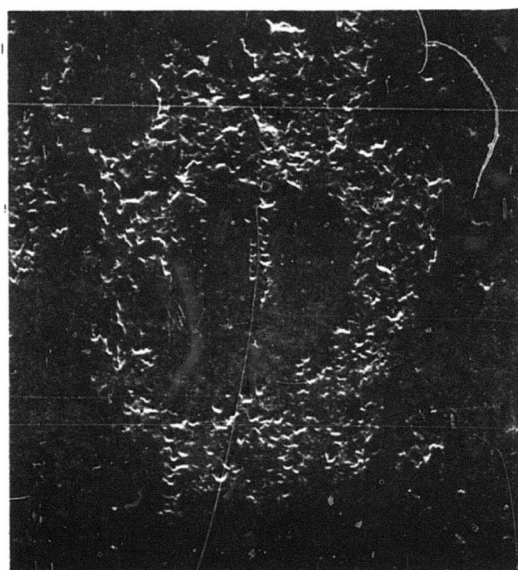
d) 100X, 706.3 HR.
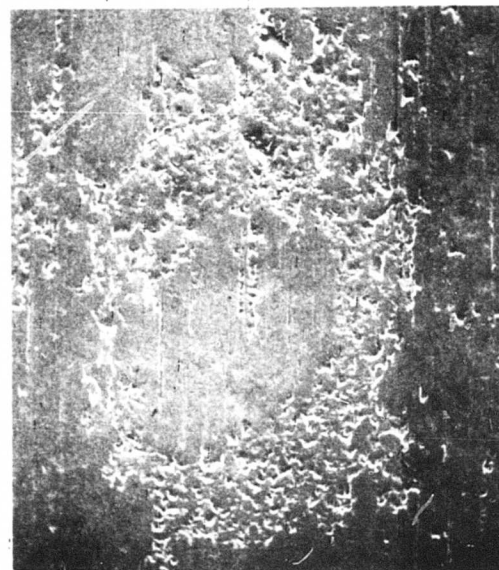
e) 100X, 774.9 HR.

Figure 44. Low Magnification Sequential Views of Dent Defect of
Figure 42 Showing Associated Spalling and Peeling.

Preceding page blank

b) 100X, 502.2 HR.
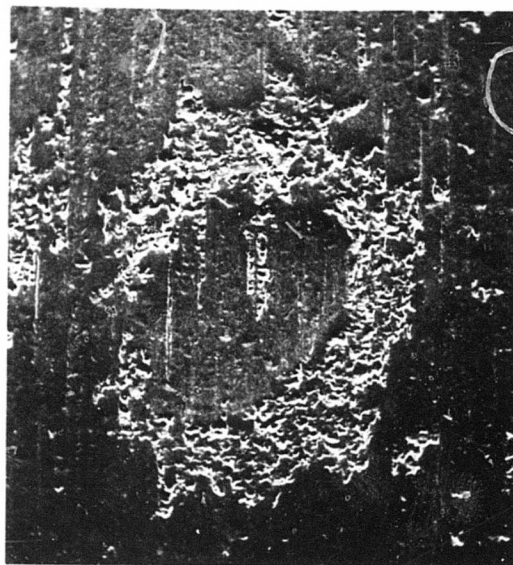
c) 100X, 591.7 HR.

DIRECTION OF ROLL
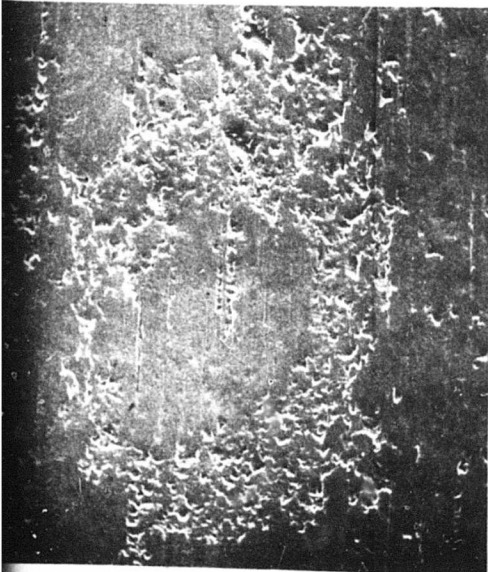
e) 100X, 774.9 HR.
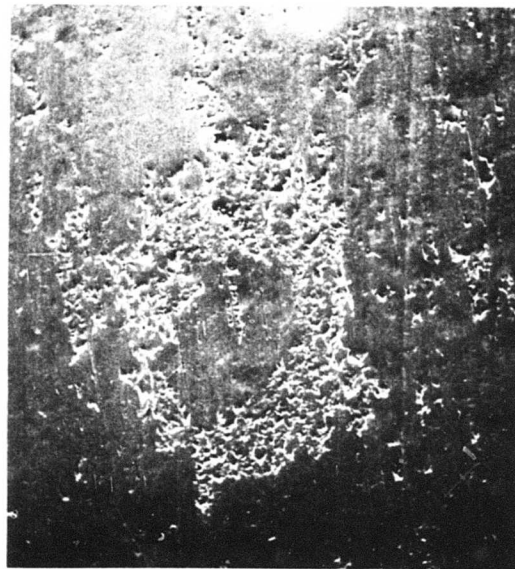
f) 60X, 793.7 HR.

DIRECTION OF ROLL

of Dent Defect of
ing and Peeling.

a) 1000X, 431 5 HR   b) 1000X, 502 2 HR   c) 800X

Figure 45. High Magnification Sequential Views of the Shallow
            Spalling Region of Figure 43.

105

b) 1000X, 502 2 HR

c) 800X, 706 3 HR

DIRECTION OF ROLL

...ial Views of the Shallow

43.

As mentioned above, a small spall was noted in one of the wheels after 706.3 hours. The test was continued, however, to determine the influence of this large defect upon the test specimen. Small pieces exfoliating from the spall clearly introduced dents on the specimen. The pronounced smoothing of the specimen surface that occurred in the last stages of the test run may also have been influenced by the spall, but further investigation would be required to verify this. Likewise, a small surface cracking region on the specimen, noted after 774.9 hours and shown in the upper micrographs in Figure 46, may also have been influenced by the spall on the wheel. After the final run, 793.7 hours, a much larger incipient spall (bottom micrographs of Figure 46) had formed in conjunction with the original defect, which appears in the upper left of the bottom left-hand micrographs. The surface within this larger spall appears flattened, much the same as in the large spalls of specimens 1, 2 and 7A. It would be very interesting to determine if subsurface cracking connects the first cracking region (of the upper micrographs) with this spall, since this could contribute to the understanding of spall initiation and growth.

The micrographs in Figure 47 present a comparison as a function of running time of regions of the contact surface which had not experienced peeling or spalling. The original surface had been discussed previously. At the conclusion of testing, 793.7 hours, some surface finishing lines were still evident. However, it is obvious that significant plastic deformation of the surface had occurred, particularly during the earlier stages of running. The changes which developed during running from 362.9 to 793.7 hours were more subtle, with the surface appearing to have undergone very localized flow to yield the details in Figure 47.

On the basis of the large amount of information gathered in this single interrupted test, it is felt that this initial investigation has demonstrated the potential of a combined analytical, experimental and SEM analysis approach to rolling contact phenomena studies. A broad range of variables such as surface finishing quality, material, heat treatment, relative hardness of rolling elements, lubrication, presence of sliding or traction, and others could be systematically evaluated for critical rolling contact and gearing applications. This investigation has shown that a variety of mechanisms are operative even in a relatively straightforward testing program and has clearly indicated the value of obtaining information other than life data. This is particularly important from the point of view of evaluating the influence of particular characteristics of a testing technique upon the results obtained.

Preceding page blank
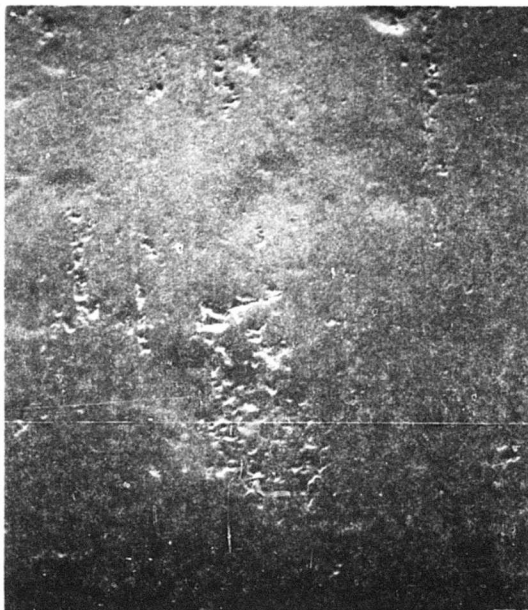
a) 100X   b) 300X   c) 60

Figure 46.   Incipient Spall on Specimen Which Developed After Wheel
Had Started Spalling.

Preceding page blank

109
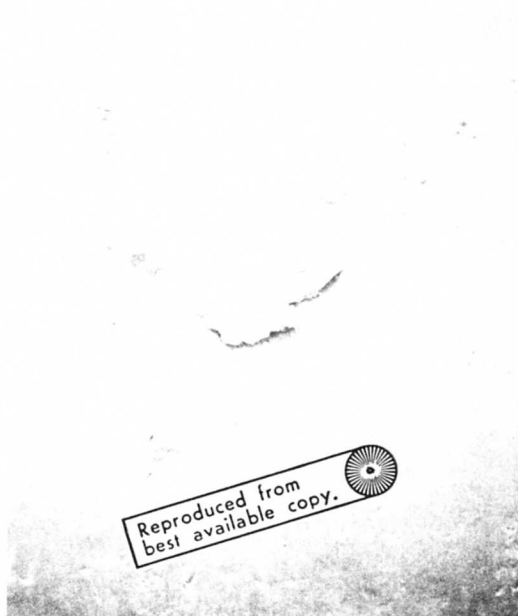
c) 60X
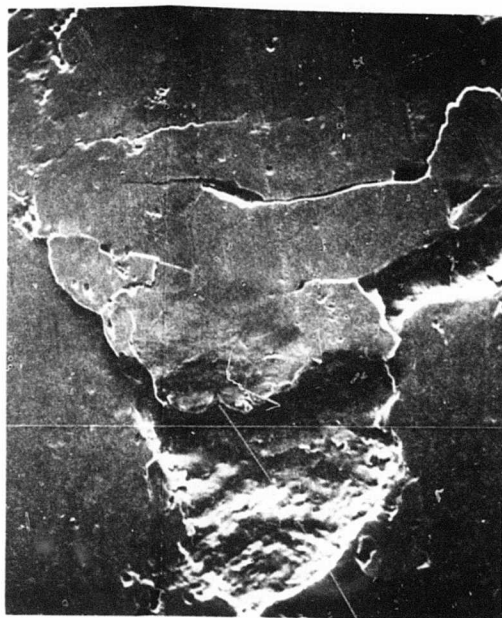
d) 180X

DIRECTION OF ROLL

a) 300X, As-ground   b) 300X, 362.9 HR   c)

d) 1000X, As-ground   e) 1000X, 362.9 HR.   f)

Figure 47. Comparison of General Surface Appearance.

b) 300X, 362.9 HR.

c) 300X, 793.7 HR.

DIRECTION OF ROLL

e) 1000X, 362.9 HR.

f) 1000X, 793.7 HR.

DIRECTION OF ROLL

Surface Appearance.

DYNAMIC CAPACITY CALCULATIONS FOR A SPUR GEAR MESH

SAMPLE PROBLEM

The dynamic capacity, C_m, summarized in Table VIII, was calculated for
a standard contact ratio spur gear set and a high contact ratio spur
gear set. The high contact ratio gear set contains the same number of
teeth in both gears, has the same diametral pitch, and is designed as an
equivalent gear set[16]. This sample problem then provides an opportunity
to show how to calculate the dynamic capacity of the mesh and also to
determine the relationship between a standard contact ratio and a high
contact ratio gear. Table XIX contains the numerical calculations in
tabular form. The first section of the table relates the input for the
4.5 diametral pitch gears on a 10-inch center distance. The standard
contact ratio gear set has a pressure angle of 25 degrees and a contact
ratio of 1.5243. The high contact ratio gear set has a pressure angle
of 21 degrees and a contact ratio of 2.3447. Next, the arc of approach
and the arc of recess are computed and added to give the total angle of
action of each individual tooth. Then the arcs of low load zones (β_L)
and the arc of the high load zone (β_H) are computed. These load distri-
butions are shown in Figures 10 and 11. Next, the roll angles are cal-
culated per Table VII for both gear sets. The load zones for the various
roll contact angles are identified in Figures 10 and 11. Next, the ψ or
integral function for the various loaded arcs of the tooth are computed
for the standard contact ratio gear according to Equations 77 through 80,
and for the high contact ratio gear according to Equations 81 through 86.
An assumption was made in these calculations that the coefficient of trac-
tion equalled zero over the arcs of contact. The experimental test results
on the rolling contact rig indicated that the effect of the coefficient
of traction was not significant; therefore, the simplification. It is
interesting to note in the I_{ij} integrals of Table XIX that for the
standard contact ratio gear, the center portion or single tooth loading
portion of the tooth has the highest number, I_{23}, and therefore has the
lowest life. One would tend to expect a higher incident of failures in
this zone. Also, the addendum of the pinion or the I_{34} zone is also
significantly higher than the initial I_{23} zone on the dedendum. The
high contact ratio gear shows the second and fourth zones with the highest
values. Again, these correspond to the two zones of high tooth loading
and one would expect a higher incident of failures in these zones. Finally,
the dynamic capacity, C_m, is computed per the summary, Table VIII.

The dynamic capacity of the standard contact ratio spur gear set equals
64,785 pounds. This by definition is the tangential load (W_t) which can be
carried by the gear set for one million revolutions of the pinion. The
dynamic capacity of the high contact ratio gear set is 76,740 pounds.
This is higher than for the standard contact ratio gear set. However, it
should be noted that the high contact ratio gear has a narrower face of
4.38 inch as compared to the 4.7553 inch of the standard set. If one

Preceding page blank

TABLE XIX. SAMPLE CALCULATION OF DYNAMIC CAPACITY

Sym	Description	Formula	STD. $1 <$ STD < 2	HCR. $2 <$ HIGH < 3
N_1-N_2	Number of teeth		41-49	41-49
r_{o1}	Pinion outside radius	Given	4.7778	4.8972
r_{o2}	Gear outside radius		5.6667	5.7480
F	Face width (min)		4.7553	4.3800
ϕ	Pressure angle	$\cos 25° = .90631$	25.0°	21.0°
C	Center distance	$\sin 25° = .42262$	10.00	10.00
P_d	Diametral pitch	$\cos 21° = .93358$	4.5	4.5
r_1	Pinion pitch rad.	$\sin 21° = .35837$	4.5556	4.5556
r_2	Gear pitch rad.		5.4444	5.4444
r_{b1}	Pinion base rad.		4.12875	4.25299
r_{b2}	Gear base rad.		4.93436	5.08284
ρ_P	Pinion curv. at tip	$\rho_P = \sqrt{r_{o1}^2 - (r_1 \cos\phi)^2}$	2.4043	2.4278
ρ_G	Gear curv. at tip	$\rho_G = \sqrt{r_{o2}^2 - (r_2 \cos\phi)^2}$	2.7864	2.6841
Z	Length of line of action	$Z = \rho_P + \rho_G - C \sin\phi$	0.9645	1.5282
θ_P		$\theta_P = 2\pi/N_1$	0.153248	0.153248
m_P	Contact ratio	$m_P = Z/\theta_P r_{b1}$	1.5243	2.3447
ϕ_1	Aux. pinion angle	$\cos\phi_1 = (r_1 \cos\phi/r_{o1})$	.86415	.86845
ϕ_2	Aux. gear angle	$\cos\phi_2 = (r_2 \cos\phi/r_{o2})$	.87076	.88428
$\sin\phi_1$			.50327	.49571
$\sin\phi_2$			.49166	.46690
ϕ_1	Arc of approach	$\phi_1 = (r_{o2} \sin\phi_2 - r_2 \sin\phi)/r_{b1}$	-.11758	-.17235
ϕ_1'	Arc of recess	$\phi_1' = (r_{o1} \sin\phi_1 - r_1 \sin\phi)/r_{b1}$	.11604	.18701
Y	Total angle of action	$Y = \phi_1 + \phi_1'$	.23362	.35936
β_L	Arc of low load zones	$x =$, $\beta_L =$; $\beta_L = X Y/m_P$	0.5243 / 0.08037	0.3447 / 0.05283
β_H	Arc of high load zones	$1-x =$, $\beta_H =$; $\beta_H = (1-x) Y/m_P$	0.4757 / 0.07288	0.6553 / 0.10043
θ_1	Roll < for start of contact	$\theta_1 = \tan\phi - \phi_1$	0.34872	0.21151
θ_2		$\theta_2 = \theta_1 + \beta_L$	0.42909	0.26434
a			0.50197	0.36477

Symbol	Description	Equation	Value 1	Value 2
ϕ_1	Arc of approach	$\phi_1 = (r_{o2}\sin\phi_2 - r_2\sin\phi)/r_{b1}$	.11758	.17235
ϕ_1'	Arc of recess	$\phi_1' = (r_{o1}\sin\phi_1 - r_1\sin\phi)/r_{b1}$	.11604	.18701
γ	Total angle of action	$\gamma = \phi_1 + \phi_1'$	.23362	.35936
β_L	Arc of low load zones	$\beta_L = x\,\gamma/m_p$ $x =$ $\beta_L =$	0.5243 / 0.08037	0.3447 / 0.05283
β_H	Arc of high load zones	$\beta_H = (1-x)\,\gamma/m_p$ $1-x =$ $\beta_H =$	0.4757 / 0.07288	0.6553 / 0.10043
θ_1	Roll < for start of contact	$\theta_1 = \tan\phi - \phi_1$	0.34872	0.21151
θ_2		$\theta_2 = \theta_1 + \beta_L$	0.42909	0.26434
θ_3	(Reference Table VII)	$\theta_3 = \theta_1 + \beta_L + \beta_H$	0.50197	0.36477
θ_4		$\theta_4 = \theta_1 + 2\beta_L + \beta_H$	0.58234	0.41760
θ_5		$\theta_5 = \theta_1 + 2\beta_L + 2\beta_H$		0.51803
θ_6		$\theta_6 = \theta_1 + 3\beta_L + 2\beta_H$		0.57086
I_{12}	I_{ij} appear in denominator (Table VIII)		0.000525	0.000464
I_{23}	High values mean less life		0.011344	0.003914
I_{34}	Central portion and addendum of pinion have less life		0.000965	0.000315
I_{45}				0.009263
I_{56}				0.001561
ψ	Std. $\psi = I_{12} + I_{23} + I_{34}$	HCR $\psi = I_{12} + I_{23} + I_{34} + I_{45} + I_{56}$	0.012834	0.015518
f_G	$[\psi \cos\phi^{-28/3}\sin\phi^{35/6}]^{-2/9}$		6.5564	8.2789
f_H	Harness factor for RC 61 = 1.0		1.0	1.0
m_G	Gear ratio = N_2/N_1		1.195	1.195
	$(1 + m_G)^{-41/27} = (1.195)^{-41/27} =$		0.7630	0.7630
$F^{7/9}$			3.3627	3.1545
	$(N_1 r_1)^{-2/9} = [(41) \times (4.5556)]^{-2/9}$		0.3128	0.3128
B	Material constant Eq. (88)		27,360	27,360
λ	(non-crown) Load Distribution Factor		0.45	0.45
C_M	Dynamic Capacity $C_M = B_\lambda f_H f_G (1+m_G)^{-41/27} F^{7/9} (N_1 r_1)^{-2/9}$ See Table VIII		64,785	76,740

B

were to calculate the high contact ratio gear with the same face width
as the standard one, the dynamic capacity would be still higher and
equal to 81,807 pounds. Thus, in this sample problem, the high contact
ratio gear set with the same face width as a corresponding standard
contact ratio gear set would have a dynamic capacity 26% higher than for
the standard set. Since life is equal to the fourth power of the ratio
of the dynamic capacity to the tangential load, the 26% increase in
capacity would mean a 254% increase in predicted fatigue life. Thus,
the high contact ratio gear set, as expected, has a higher predicted fatigue
life under the same loading conditions.

COMPARISON WITH AGMA SURFACE DURABILITY

The AGMA surface durability (pitting) standard[1] was then used to
calculate the ratings for the standard contact ratio sample problem.
These calculations are shown in Table XX. The calculated contact stress
number for the standard contact ratio gear set under a transmitted
tangential load (W_t) of 29,332.1 pounds is 192,551 psi. This is 86% of
the allowable contact stress number for an RC-60 fully hardened gear of
225,000 psi. The life factor (C_L) is then calculated by multiplying the
ratio of the calculated contact stress to the allowable contact stress
by the hardness ratio factor, the temperature factor, and the factor
of safety as identified in the standard. The life factor is 0.86 or
greater than 10^7 cycles according to the appropriate life factor figure
of the AGMA standard. A comparison between the life of the gear set
computed with the life model or dynamic capacity and the life factor of
the AGMA standards is shown in Table XXI. Various values of the life
factor, C_L, were assumed and corresponding tangential loads (W_t) were
calculated. These tangential transmitted loads were then used with the
dynamic capacity (C_m) to compute the millions of cycles. The results
of Table XXI are shown graphically in Figure 48, which is a reproduction
of the life factor graph from the AGMA surface durability standard[1].

The life prediction using the dynamic capacity is similar around 10^7 cycles
to the AGMA life factor curve. The slope of the dynamic capacity calcula-
tion (fourth power relationship) is greater than the slope assumed in the
AGMA standard. Also, the dynamic capacity approach to life calculation
allows computation of predicted fatigue life for any loading because
there is no asymptotic value as shown on Figure 48 for an AGMA life factor
of 1.0. This makes the dynamic capacity approach useful for reliability
calculations. As actual spur gear durability or pitting fatigue life
information becomes available, it may be desirable to modify the slope
of the life calculation. This was done in the case of roller bearings.
The AFBMA (Anti-Friction Bearing Manufacturers Association) standard[4]
and the ASA standard[5] for evaluating the load ratings of ball and
roller bearings suggest the use of a ten-thirds power (10/3) for the
load-life relationship of a roller bearing. The basic theory in Refer-
ence 3 develops a fourth-power relationship for a roller bearing with
line contact between the rollers and races. It was found necessary,

117

TABLE XX. AGMA SURFACE DURABILITY (PITTING) CALCULATION FOR SAMPLE PROBLEM

Symbol	Description	Std
S_c	Calculated contact stress No. $= C_P \sqrt{\dfrac{W_t C_o}{Cr} \cdot \dfrac{C_s}{dF} \cdot \dfrac{C_m C_f}{I}}$	
C_P	Elastic coefficient $= \sqrt{\dfrac{1}{\pi\left(\dfrac{1-\mu_p^2}{E_P} + \dfrac{1-\mu_G^2}{E_G}\right)}}$ $\quad \mu = 0.25$ $\quad E = 30 \times 10^6$	2256.8
W_t	Transmitted tangential load (lb)	29,332.1
C_o	Overload factor, uniform	1.00
C_r	Dynamic factor, ground spur gears – aircraft quality	1.0
C_s	Size factor	1.0
d	Pinion operating pitch diam.	9.1112
F	Face width	4.7553
C_m	Load distribution factor	1.1
C_f	Surface condition factor	1.0
Z_c	Distance measured along the line of action from the pitch point to lowest point of single tooth contact $Z_c = (\phi_1 - \beta_L)\, rb_1$	0.1537
I	Geometry factor $= 2 ccs\phi \left(\dfrac{m_G}{m_G+1}\right)\left(\dfrac{\sin\phi}{2} + \dfrac{Z_c}{D}\right)\left(\dfrac{\sin\phi}{2} - \dfrac{Z_c}{d}\right)$	0.1023
S_c	$(2256.8)\left[\dfrac{(29,332.1)\,(1.0)}{(1.0)} \cdot \dfrac{(1.0)}{(9.1112)\,(4.7553)} \cdot \dfrac{(1.1)(1.0)}{0.1023}\right]^{1/2}$	192,551 psi
S_{ac}	Allowable contact stress number 60 RC	225,000 psi
C_L	Life factor $\quad C_L = \dfrac{S_c}{S_{ac}} \cdot \dfrac{C_T C_R}{C_H}$ when $\quad C_T = 1.0$ $\quad C_R = 1.0$ $\quad C_H = 1.0$	0.86 $>10^7$ cycles
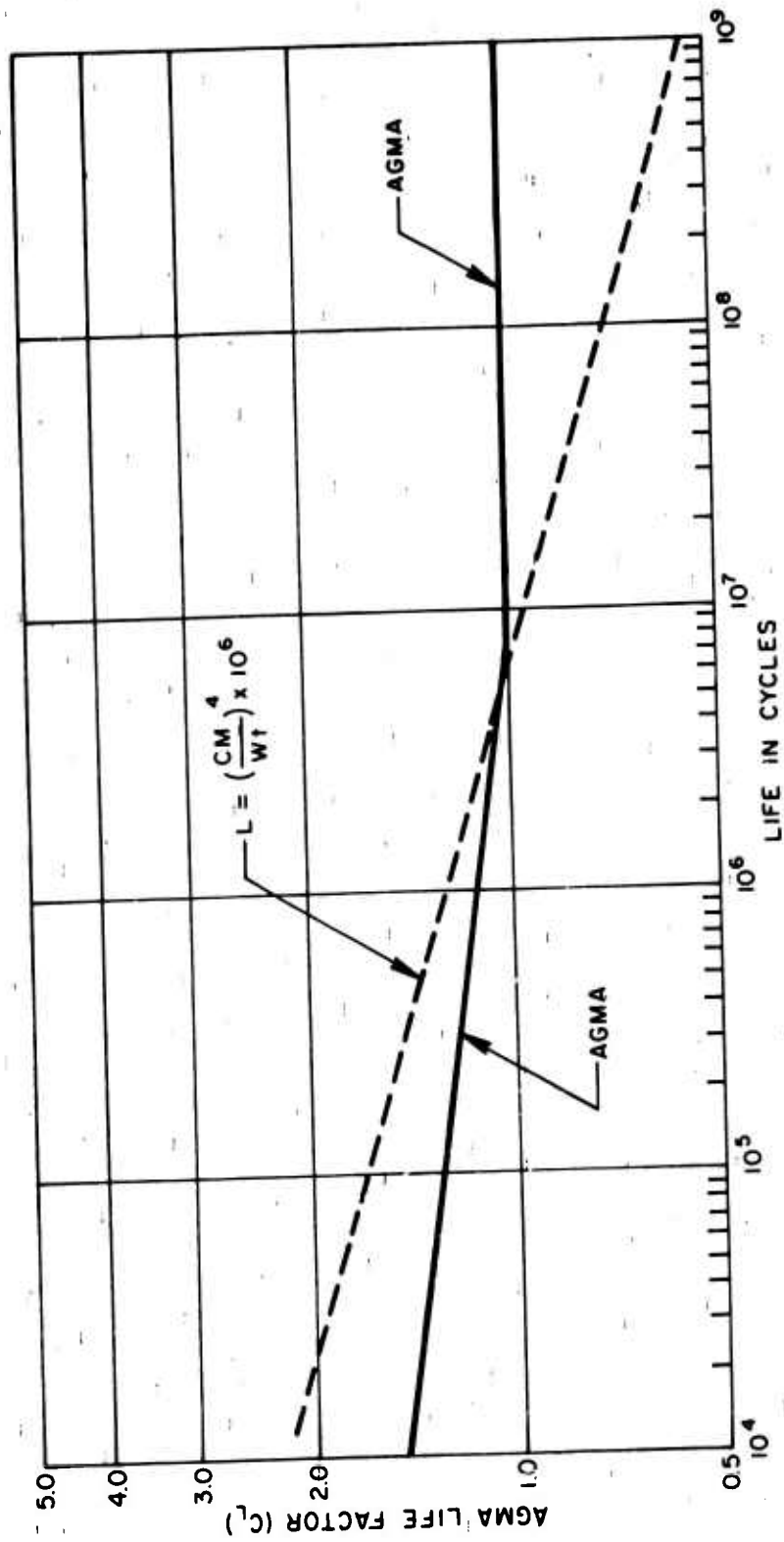
Figure 48. Comparison of Dynamic Capacity and AGMA Life Factor.

TABLE XXI. COMPARISON OF DYNAMIC CAPACITY AND AGMA LIFE FACTOR				
W_t (lb)	S_c (psi)	$C_L = \dfrac{S_c}{225,000}$	$\left(\dfrac{C_M}{W_t}\right)$	$\left(\dfrac{C_M}{W_t}\right)^4 \times 10^6$ Cycles
29,332.1	192,551	0.86	2.209	2.38×10^7
40,051	225,000	1.0	1.618	6.85×10^6
57,674	270,000	1.2	1.123	1.59×10^6
78,500	315,000	1.4	0.825	0.46×10^6

$$C_M = 64,785 \text{ lb (Table XIX) for } 10^6 \text{ cycles.}$$

$$S_c = 1124.28 \sqrt{W_t} \text{ psi (Table 9)}$$

in practice, to modify the fourth power to a ten-thirds power to account
for bearings with mixed types of contacts such as crowned rollers and
spherical roller bearings. Such bearings can have point contact
between the roller and one race and line contact between the roller
and the other race. Thus, modification of the power relationship in
the load-life formula is not a new problem. Indeed, discussion over
the years at the AFBMA has centered on whether a cubic relationship
should be used for both ball and roller bearings without loss of accu-
racy resulting in broader generality. The comparison of the current
suggested life model for the numerical example is not inconsistent with
the present AGMA rating methods.

CONCLUSIONS

The following conclusions are made from this study:

- The dynamic capacity of a spur gear mesh was formulated and presented in a manner very similar to that used for ball and roller bearings (References 4 and 5).

- The effect of surface tractions upon theoretical subsurface oriented fatigue life was found to be negligible at coefficients of traction below 0.10 as normally encountered in spur gear applications.

- Surface traction was experimentally found to have no significant statistical effect upon the fatigue life of cylindrical test specimens.

- The results of the limited fatigue testing provided a reasonable initial estimate for a material factor to be used in the dynamic capacity calculations.

- The technique of examining surface metallurgy with a scanning electron microscope (SEM) was shown to be a powerful new method for describing progression of failure.

- The predicted fatigue life of a typical spur gear mesh was calculated and shown not be inconsistent with current AGMA durability ratings.

- A geometry factor, f_G, was hand calculated for the numerical example. A need exists to tabulate this factor to facilitate use of the life formula for design studies.

LITERATURE CITED

1. AGMA STANDARD FOR SURFACE DURABILITY (PITTING) OF SPUR GEAR TEETH, AGMA 210.02, Jan. 1965, Published by American Gear Manufacturers Association, Washington, D.C.

2. Lundberg, G., and Palmgren, A., DYNAMIC CAPACITY OF ROLLING BEARINGS, Acta Polytechnic, Mechanical Engineering Series Vol. 1, Nr 3, Royal Swedish Academy of Eng. Sciences, Stockholm, 1947. Also a condensed version ASME Jnl. of App. Mech., June 1949, pp. 165-172.

3. Lundberg, G., and Palmgren, A., DYNAMIC CAPACITY OF ROLLER BEARINGS, Acta Polytechnic, Mech. Eng. Series Vol. 2, Nr. 4, Stockholm, 1952.

4. AFBMA STANDARDS, METHOD OF EVALUATING LOAD RATINGS FOR BALL BEARINGS, Section 9, Rev. 4, Oct. 1960, The Anti-Friction Bearing Manufacturers Association, Inc., 60 East 42nd Street, New York City.

5. AMERICAN STANDARD METHOD OF EVALUATING LOAD RATINGS FOR BALL AND ROLLER BEARINGS, ASA Standard B3.11-1959.

6. Peritsky, H., STRESSES AND DEFLECTIONS OF CYLINDRICAL BODIES IN CONTACT WITH APPLICATION TO CONTACT OF GEARS AND OF LOCOMOTIVE WHEELS, ASME Trans., Jnl. of Applied Mech., June 1950, pp. 191-201.

7. Seely, F. B. and Smith, J. O., ADVANCED MECHANICS OF MATERIALS, John Wiley & Sons, N.Y., Second Edition, 4th Printing, 1959, Sect. 110, STRESSES FOR TWO BODIES IN LINE CONTACT; LOADS NORMAL AND TANGENT TO CONTACT AREA, pp. 368-376.

8. Liu, C. K., STRESS AND DEFORMATIONS DUE TO TANGENTIAL AND NORMAL LOADS ON AN ELASTIC SOLID WITH APPLICATIONS TO CONTACT STRESS, PhD Thesis, University of Illinois, June 1950.

9. Smith, J. O., and Liu, C. K., STRESSES DUE TO TANGENTIAL AND NORMAL LOADS ON AN ELASTIC SOLID WITH APPLICATION TO SOME CONTACT STRESS PROBLEMS, ASME Trans., Jnl. of App. Mech., June 1953, pp. 157-166.

10. Dudley, D. W., PRACTICAL GEAR DESIGN, McGraw Hill, New York, 1954.

11. Eschman, Hasbargen, and Weigand, BALL AND ROLLER BEARINGS, THEIR THEORY, DESIGN, AND APPLICATION, Kugelfisher Georg Schäfer & Co., R. Oldenburg, München, 1958.

12. Bamberger, E. N., THE EFFECT OF AUSFORMING ON THE ROLLING CONTACT FATIGUE LIFE OF A TYPICAL BEARING STEEL, Trans. of ASME, Jnl. of Eng. for Power, June 1966, pp. 1-10.

13. Johnson, L. G., THE STATISTICAL TREATMENT OF FATIGUE EXPERIMENTS, Elsevier, New York, 1964.

14. Broersma, G., MARINE GEARS, The Technical Publishing Company H. Stam N.V., The Netherlands, 1961.

15. Buckingham, E., ANALYTICAL MECHANICS OF GEARS, McGraw Hill Book Co., New York, 1949.

16. Lemanski, A. J., and Alberti, J. P., INVESTIGATION OF INCREASED LOAD CAPACITY OF SPUR AND HELICAL GEARS WITH INCREASED CONTACT RATIO, The Boeing Company, Vertol Division, Philadelphia, Final Report D210-10190-1, prepared for Naval Air Systems Command, Dept. of the Navy (Contract No. N0019-69-C-0418), October 1970.

17. Dudley, Dale W., GEAR HANDBOOK, McGraw-Hill, New York, N.Y., 1962, pp. 14-15.